Università degli Studi di Firenze
Scuola di Ingegneria
DIEF - Department of Industrial Engineering of Florence

PhD School: *Energetica e Tecnologie Industriali ed Ambientali Innovative*
Scientific Area: ING-IND/08 - *Macchine a Fluido*

Aerodynamic Investigation of Steam Turbine Exhaust System Through CFD Modelling: Design Performance Optimization and Off-Design Assessment

PhD Candidate: Ing. Tommaso Diurno

Tutor: Prof. Ing. Bruno Facchini

CoTutor: Prof. Ing. Antonio Andreini

PhD School Coordinator: Prof. Ing. Giampaolo Manfrida

XXXIV PhD School Cycle - 2018-2021

A mio Nonno Amedeo,
Sei sempre nei mie pensieri,

Alla mia dolce Sara,
Sei la mia forza,

Acknowledgements

Eccomi di nuovo a scrivere una tesi, la terza del mio percorso universitario. Questa è senza dubbio la più significativa perchè frutto di 3 anni di lavoro e culmine di un bellissimo percorso. Un percorso certamente difficile, che mi ha posto davanti a grandi sfide, accompagnate però da altre tante soddisfazioni. Un'esperienza mi che mi sento di consigliare a qualche altro matto come me, che dopo 5 anni di università ancora non si sente stanco di studiare. Confesso che la scelta non è stata immediata, ma, a distanza di 3 anni, posso essere fiero di dire che è stata quella giusta. Desidero quindi ringraziare tutte le persone che hanno facilitato questo viaggio, in forme differenti ma tutte di grande importanza.

Prima di tutto desidero menzionare le due persone che hanno reso possibile tutto questo: il Prof. Bruno Facchini e il Prof. Antonio Andreini, che mi hanno accolto a braccia aperte, credendo fin da subito in me. Vi sarò per sempre grato per questa oppurunità e mi sento orgoglioso di aver fatto parte di questo fantastico gruppo di ricerca, l'HTC group. La vostra esperienza e le vostre capacità mi hanno permesso di crescere molto.

Desiro poi ringraziare la mia guida in questo viaggio: Tommaso Fondelli. Sei stato molto importante nel raggiungimento di questo traguardo, dipensandomi consigli preziosi che mi hanno insegnato molto.

Un grande ringraziamento anche ai miei nuovi colleghi del gruppo di turbine a vapore di Baker Hughes per aver contribuito a questo lavoro, in particolare Lorenzo Arcangeli, Nicola Maceli e Leonardo Nettis.

Come non menzionare poi i miei amici e compagni di avventura del 34esimo ciclo: Pier Carlo, Leonardo e Carlo Alberto, abbiamo affrontato

insieme gioie e dolori di questo percorso. Purtroppo la pandemia ci ha tenuto per molto tempo a casa in smart working e ci ha impedito di vivere a pieno l'esperienza di dottorato. I momenti di diverimento non sono comunque mancati, qualche trasferta (troppo poche, maledetto covid!), molte cene HTC e tante tante risate anche sulle cose più stupide. Un ringraziemento speciale al mio compagno di ufficio (e vicino di casa) Pier al quale devo riconscere l'incomensurabile supporto tecnico (Pier...consulenza?) e morale (basta la lettura mirata di alcuni passi di un celebre racconto per cambiare l'umore di un grigio pomeriggio a Santa Marta). Grazie sopratutto per avermi fatto assaggiare il delizioso té al Mango Thai (scaduto da 1 anno) e per ricordami di spostare la macchina quando c'è pulizia strade.

Un sentito ringraziamento va anche a tutti i membri dell'HTC group, al faro dell'ufficio (o forse di tutta Santa Marta) Matte P per il suo supporto informatico, per la sua battuta sempre pronta e per non avermi "bullizzato" più di tanto. A Lore W che mi ha accolto nel gruppo, al Mazze e Davide per il loro preziosi consigli. A tutti i ragazzi dell'ufficio A: Simo, Sabri, Dani e dell'ufficio B: Albe, Matte e Gama e a tutte le nuove leve, a cui auguro di viversi al meglio questa esperienza.

Passando ai ringraziamenti extra accademici, desidiro ringraziare il mio "fratellino" Checco con il quale sono cresciuto e tutti i "Rega", amici da sempre. Anche se non viviamo più in simbiosi come ai (bei) vecchi tempi voglio dirvi che siete e sarete sempre importanti per me. Il tempo che trascorriamo insieme è sicuramente minore ma sempre piacevole e spensierato.

Non può mancare un grande ringraziamento a tutta la mia pazza famiglia allargata, in primis ai miei genitori che mi hanno sempre supportato in ogni mia scelta e cercato sempre il meglio per me. Ogni mio passo è un immenso grazie che vi devo. Grazie alla mia nonna Elena che mi ha cresciuto e che stravede per me e grazie anche ai miei nonni Amedeo e Paola che purtroppo non possono godersi questo mio momento così speciale. Caro Nonno, sono sicuro che saresti stato come sempre in prima fila per vivere le miei gioie. Non dimenticherò mai quello che hai

fatto per me.

Dulcis in fundo desidero ringraziare Sara, perchè ogni traguardo è più bello quando è vissuto con la persona che ami. Ti ringrazio per l'immenso supporto che mi hai dato in questi anni, ti ringrazio perchè sai capirmi con uno sguardo e sai motivarmi nelle difficoltà. Penso sia impossibile quantificare quanto hai contibuito al raggiungimento di questo obiettivo, potrei mettermi ad elencare tutto quello che hai fatto per me, ma voglio riassumere tutto dicendoti grazie di essere sempre al mio fianco nelle sfide di oggi e in quelle che ci saranno domani. Un grande grazie anche a tutta la tua famiglia, perchè con loro mi sento a sempre a casa.

Abstract

Steam turbines play a key role in the world energy scenario since they are widely used, as thermal engines, in fossil-fueled, nuclear, and concentrated solar power plants. The most recent trends in steam turbine design practice are, therefore, strongly related to the development of the energy market, which is even more oriented towards a fast renewable energy expansion. As a direct consequence, due to intrinsic variability of the green-energy resources, the steam turbines address the need to increase their flexibility to ensure the stable functioning of the power grid. Increasing the flexibility of conventional power plants usually involves retrofitting certain components, for instance, new high-performing low-pressure blades are coupled with a standard exhaust hood. The latter has a great influence on the overall turbine performance since it converts the residual kinetic energy of the flow which leaves the last stage into static pressure increasing the last-stage power output. In most steam turbines, the exhaust hood has a radial shape to reduce the overall length of the component, however, this solution leads to a complex aerodynamic behavior since the flow turns by 90 deg in a very short distance and this generates highly rotational flow structures which are the main source of losses within this component. The retrofitting of the new blades with an "old" exhaust hood might drastically affect the pressure recovery performance due to the strong coupling between these components, reason why it should be associated with a re-design of the exhaust hood to ensure high performance. In this context, this work deals with the development of a design approach for the steam turbine exhaust hood aimed at maximizing

the pressure recovery performance, for a defined last stage geometry, through CFD modeling. Due to the already mentioned strong coupling between the last stage and the exhaust hood, it is necessary to consider the presence both in the fluid domain. However, modeling the unsteady full 3D turbine stage coupled to the exhaust system results in a remarkable number of grid elements with a significant computational effort and it cannot be applied to an optimization strategy that requires a high amount of numerical simulations, it has been used only in the final part of this work to investigate the off-design conditions where the flow unsteadiness must not be neglected. For the optimization strategy different simplified interfaces have been tested, among these, the mixing plane interface has been selected as the best trade-off between accuracy and computational effort. The presented numerical approach has been applied to an exhaust hood manufactured by Baker Hughes. As baseline geometry, a standard exhaust system has been designed however it shows low-pressure recovery performance confirming the risks of retrofitting. By performing detailed aerodynamic post-processing of the baseline geometry results, the main issues of such geometry have been detected and consequently, the re-design procedure has been undertaken. Since the strong fluid-dynamic coupling existing between exhaust hood casing and diffuser (which are the main components of the exhaust hood), a parametric model has been developed including geometrical parameters of both the components, which represent the input data for the optimization procedure. Due to the significant number of parameters taken into account, a simplification of the fluid model is necessary to perform the optimization analysis in a feasible time. For this purpose, a simplified fluid domain has been developed based on the idea to consider the flow in the diffuser as symmetric, allowing to keep the number of grid elements low by considering as fluid domain a single stator and rotor passage coupled to a periodic slice of the diffuser, with the mixing plane as coupling interface. This model neglects the effect related to the asymmetry of the exhaust hood casing and consequently a verification with a 3D model is required as the final step of the procedure is required. A response surface has been achieved as

a function of the key geometrical parameters, therefore an optimization method has allowed identifying the best performing configuration. A 3D model of the optimized periodic geometry has been then generated to assess the effectiveness of the procedure here presented. The comparison between the periodic and the 3D model has highlighted a good agreement in both the averaged pressure recovery factor prediction and flow field resolution within the diffuser, with a speedup of the computational time by about one order of magnitude. The optimized geometry identified presents a pressure recovery factor, calculated in the condenser section, 28% greater than the baseline one. The improvement of the performance is achieved even with a reduction of the exhaust system volume equal to 4%.

Once optimized the design condition performance and therefore defined the geometry of both the last stage and the exhaust hood, the focus is moved on the assessment of the off-design conditions. In the already presented energy scenario, due to intrinsic variability of the green-energy resources, the steam turbines address the need to increase the operation at a low load. Such off-design conditions are extremely critical for the last stage bucket (LSB) of the low-pressure turbine since they might experience non-synchronous aerodynamic excitations triggered by the onset of unsteady fluid behavior characterized by the presence of rotating instabilities similar to the ones widely investigated in the compressors. Due to unsteadiness and strong asymmetry of the flow field in these conditions, the presented simplified numerical setup is not suitable for detailed investigation of this phenomenon but it can offer just a preliminary screening of the most dangerous conditions to be tested with a more accurate numerical setup. The flow field has been indeed studied by performing 3D unsteady CFD simulations (URANS) of the low-pressure turbine the last stage coupled with the exhaust hood, with structural struts included. The full annulus mesh of both the last stage and diffuser is considered with the transient stator-rotor interface to properly account for unsteady interaction effects. The Influence of the operating conditions on the fluid dynamic behavior is assessed by considering six different

operating conditions. Starting from the design condition and gradually decreasing the mass flow rate. The presence of rotating instabilities is demonstrated by monitoring the fluid dynamic variables during the simulation and by using advanced post-processing techniques, such as Proper Orthogonal Decomposition (POD). In the light of the results of this investigation, the operation limits of the turbine have been updated to exclude the most dangerous conditions from the machine operability range. The design solutions aimed at countering the characteristic frequencies of the rotating instabilities are to be excluded since these phenomena act on several frequencies which are unstable in time and strongly related to operating conditions.

Contents

Nomenclature

Acronyms

CFD	Computational Fluid Dynamics
CV	Cross Validation
$DDMA$	Data Driven Modal Analysis
DFT	Discrete Fourier Transform
EA	Evolutionary Algorithm
EDS	Exhaust Design System
EIA	Energy Information Administration
FFT	Fast Fourier Transform
FSI	Fluid Structure Interaction
HCF	High Cycle Fatigue
$iDDES$	improved Delayed Detached Eddy Simulation
IEA	International Energy Agency
$IRENA$	International Renewable Energy Agency
KRG	Kriging Modelling
$LEOF$	Low Engine Order Frequency
LES	Large Eddy Simulation
LFV	Low Fluid Volume
LHS	Latin Hypercube Sampling
LSB	Last Stage Bucket
$MOGA$	Multiple Objective Genetic Algorithm
NPF	Nozzle Passing Frequency

OA	Orthogonal Arrays	
PIV	Particle Image Velocimetry	
POD	Proper Orthogonal Decomposition	
$RANS$	Reynolds Average Navier Stokes	
RIF	Rotating Instability Frequency	
ROM	Reduce Order Model	
SP	Sample Split	
SAS	Scale Adaptive Simulation	
$SBAO$	Surrogate-Based analysis and Optimization	
$STFT$	Short Time Fourier Transform	
SVR	Support Vector Regression	
Greeks		
λ	Lagrangian Multiplier	$[-]$
α	Angles of the hub cone wall	$[deg]$
ε	Error	$[-]$
ρ	Density	$[kg/m^{-3}]$
Φ	Matrix of POD Spatial Distributions	$[-]$
ϕ_r	Spatial Distribution of POD mode	$[-]$
ϕ	Flow Coefficient	$[-]$
Ψ	Matrix of Eigenvectors of the Correlation Matrix	$[-]$
ψ_r	Eigenvectors of the Correlation Matrix	$[-]$
ω	Turbulence Dissipation Rate	$[s^{-1}]$
Ω	Inlet Difusser Swirl Angle	$[deg]$
Δ	Gradient	$[-]$
Σ	Matrix of Eigenvalues of the Data Correlation Matrix	$[-]$
σ_r	Eigenvalues of the Data Correlation Matrix	$[-]$
ξ	Slack Variables in SVR method	$[-]$

Letters

C	Regularization Term of SVR method	$[-]$
C_p	Pressure Recovery Factor	$[-]$
C_{tpl}	Pressure Loss Coefficient	$[-]$
C_{rke}	Residual Kinetic Energy Coefficient	$[-]$
D	Original Data Set	$[-]$
D	Post Processing Surface located in Diffuser	$[-]$
K	Temporal Correlation Matrix	$[-]$
k	Turbulent kinetic energy	$[-]$
N	Number of point in time domain	$[-]$
P	Probability	$[-]$
P_{s}	Area average of static pressure at a post processing plane	$[Pa]$
P_{t}	Mass flow average of total pressure at a post processing plane	$[Pa]$
R	Exhaust Hood Radius	$[m]$
R	Post Processing Surface in Collector Box	$[-]$
w	Coefficient of Polynomial Regression	$[-]$
U	Velocity magnitude	$[m/s]$
U_{ax}	Axial velocity at the diffuser inlet	$[m/s]$
V	Exhaust hood volume	$[m^{-3}]$

Subscripts

0	Total
ax	Axial
j	Time domain
in	Inlet
int	Interface
n	Frequency domain
out	Outlet

Introduction

Steam turbines play a key role in the world energy scenario since they are widely used for electric power generation in several configurations, ranging from conventional power plants, such as fossil-fueled, gas turbine combined cycle and nuclear, to green energy based Concentrated Solar Power (CSP) system. The most recent trends in steam turbine design practice are, therefore, strongly related to the development of the energy market, which is even more oriented towards a fast renewable energy expansion; indeed, according to IEA [1], renewable sources will overtake coal becoming the largest source of electricity generation in 2025. In 2020 the global share of renewables in electricity generation was almost 25% and, despite the economic uncertainties due to pandemic, according to IRENA's [2] estimations, it is likely to increase up to 37% in 2030 and up to 86% in 2050. A similar scenario is predicted by the IEA [3] as illustrated in Figure 1.1 in the breakdown of electricity generation.

In this energy context, due to intrinsic variability of the green-energy resources and due to the absence of commercially available and cost-effective storage systems, the steam turbines, operating in conventional power plants, address the need to increase their flexibility to ensure stable functioning of the power grid. Their lack of flexibility can indeed result in curtailment of the variable resources energy generation or idling of the traditional power plant themselves, as reported in the study of Gonazelez et al. [4].

A recent review on the steam turbine state-of-the-art presented by Gulen [5] clarifies how the most innovative steam power plants with effi-

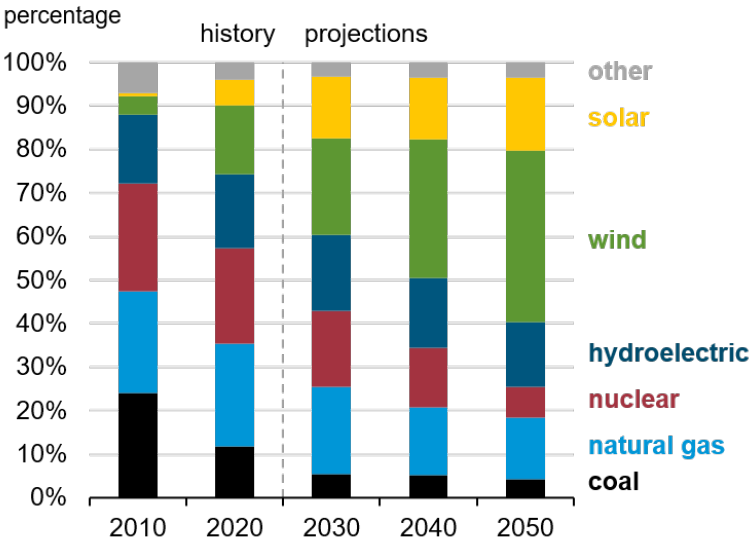

Figure 1: Breakdown of electricity generation by source, 2010-2050 [3]

ciencies in low 40 s have reached a plateau in the peak efficiency technology development. The research effort is therefore focused on the adaptation of these turbomachines to increased flexibility requirements which involves continuous start-up and shut-down of the machine and therefore frequent low load operations, also known as low volume flow (LVF) conditions. Indeed, the steam turbines were originally designed to operate in stable and fixed conditions and, in order to increase their flexibility the re-design of certain components is essential. For instance, during LVF conditions the low pressure turbines blades are subjected to complex unsteady flow phenomena and should be redesigned to resist high unsteady excitations and high thermal load due to windage, especially the last stage blades. In this scenario, a new generation of blades are designed in the last decades [6, 7, 8]. Usually, such blades are integrated into an existing turbine casing, with already designed exhaust hood (retrofitting). This proce-

dure could lead to a drastic reduction of the aerodynamic performance of the exhaust system due to the strong coupling between these components, reasons why also a redesign of the exhaust hood may be required.

Aim of the work

This work, framed in the presented scenario, aims at presenting a numerical procedure for the re-design of a steam turbine exhaust system. The procedure is based on CFD simulations carried out with a numerical setup obtained thanks to a sensitivity analysis aimed at assessing the impact on the results of different numerical strategies. The input of the procedure is the geometry of the last stage of the low pressure turbine, and the output is an optimum exhaust hood with high pressure recovery performance in design operating conditions, and in operating points close to this. Once defined the exhaust system geometry the focus is moved on the off-design conditions, in particular in LVF conditions which are characterized by the ventilation of the LSB. The pressure recovery performances are no longer of interest in such conditions while the structural integrity of the blades becomes of primary importance. For these reasons, in the final part of the procedure, an assessment of the unsteady fluid dynamic behavior is carried out to detect the rotating instabilities potentially responsible for blade vibrations. Such instabilities are detected by performing a full 3D unsteady simulation of the exhaust system (last stage + exhaust hood). The results are finally post-processed with different techniques starting with the Discrete Fourier Transform (DFT) and Short-Time Fourier Transform (STFT) up to the more advanced Proper Orthogonal Decomposition (POD) in order to in-depth characterize these aerodynamic instabilities. Finally, the output of the off-design assessment is the definition of a protection line in the machine operation map in order to exclude, from the operating range of the turbine, the operating points that experience a high level of unsteadiness. This solution can help to avoid dangerous blade vibrations.

Thesis outline

This work deals with several aspects related to the design of a steam turbine exhaust hood, starting from a description of the state-of-art up to a development of an industrial tool for the design of this component. This procedure has been developed as a result of different investigations realized during the research activity in partnership with Baker Hughes, Nuovo Pignone. This work has been rationalized as follow:

- **Chapter 1**: This chapter is focused on the state-of-art of the steam turbine exhaust system. The main findings proposed in the literature are introduced to describe different aspects related to the design of this component. This chapter offers also an insight into the theory behind the numerical models used in the work;

- **Chapter 2**: The numerical strategies for the exhaust hood flow field investigation found in the literature review are here applied to specific exhaust hoods manufactured by Baker Hughes. The aim of this chapter is to assess the influence of these strategies on flow prediction in order to find out an optimal setup as a trade-off between accuracy and computational cost. The selected numerical setup is then used to perform the numerical simulations of the design approach proposed in the following chapter;

- **Chapter 3**: This chapter describes the implementation of the numerical procedure for the exhaust hood design. Such a procedure has been obtained with a two-step development, both are described in order to highlight the significant improvement obtained by using the final procedure to optimize the aerodynamic performance in design operating condition;

- **Chapter 4**: Finally, the focus is moved on the off-design conditions. Different aspects related to the aerodynamic behavior of the exhaust hood during this condition are investigated with a specific interest in the LVF conditions which could be extremely dangerous for blade integrity.

In the last chapter, a summary of the main achievements of this research activity is given together with conclusions and recommendations for future works.

Chapter 1

Background

This chapter is focused on the state-of-art of steam turbine exhaust system, considering several aspects concerning the design of this component: flow field characterization, computational methods, aerodynamic optimization strategies and detailed off-design assessments. Besides this, abstracting from the exhaust hood research context, a general insight of the theory behind the numerical models used in this work is presented, with a specific focus on surrogate-based analysis, optimization algorithms and advanced post-processing techniques. These indeed represent the basis for the implementation of the numerical methods proposed in this work.

Before introducing these aspects, it is worth clarifying the function of the exhaust hood in the steam turbine. It is a component that converts the residual kinetic energy of the flow which leaves the last stage turbine blades into static pressure by guiding and decelerating the flow up to the condenser. This component has a significant impact on the steam turbine efficiency since it decreases the last stage outlet pressure and, consequently it increases the power output, this effect is thermodynamically shown in Figure 1.1.

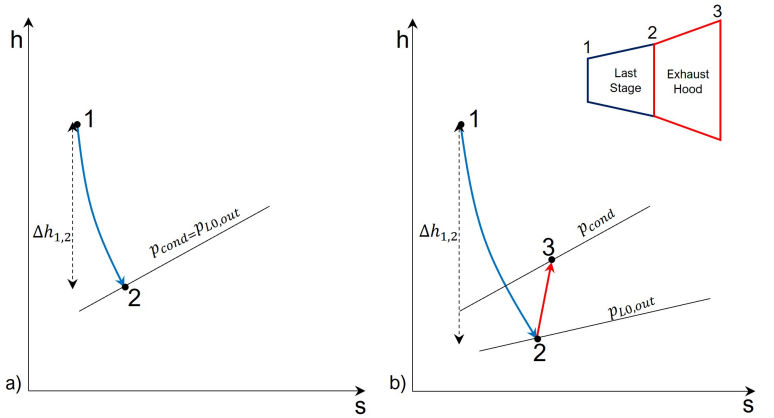

Figure 1.1: Last stage expansion without diffuser a) and with diffuser b)

The exhaust hood performances are usually analyzed by using three different parameters, they are defined as follow (with reference to the nomenclature in Figure 1.1):

- Pressure Recovery Factor (C_p), is the main performance parameter since it quantifies how much of the residual kinetic energy at the diffuser inlet is converted into static pressure. It is calculated as follows:

$$C_p = \frac{P_{s_3} - P_{s_2}}{P_{t_2} - P_{s_2}} \tag{1.1}$$

- Total Pressure Loss Coefficient (C_{tpl}), is used to estimate the pressure losses along the exhaust system flow path. It is calculated as follows:

$$C_{tpl} = \frac{P_{t_2} - P_{t_3}}{P_{t_2} - P_{s_2}} \tag{1.2}$$

- Residual Kinetic Energy Coefficient (C_{rke}), corresponds to the residual energy of the flow that is not converted into pressure

recovery. It is calculated as follows:

$$C_{rke} = \frac{P_{t_3} - P_{s_3}}{P_{t_2} - P_{s_2}} \tag{1.3}$$

It is interesting highlighting how the sum of the coefficients is equal to 1.

Concerning a quantitative impact of the exhaust hood on the steam turbine performances, Keller [9] calculated that an increase in the C_p from -0.4 to +0.3 guarantees 5 MW of additional power in a 1000 MW steam turbine. Stein et al. [10] estimated that an increase of 10% of the pressure recovery factor translates into 1% of last stage efficiency. According to Zaryankin et al.[11] the efficiency of the turbine can increase by 0.15% by decreasing 10% of total pressure losses in the exhaust hood. For these reasons, the optimization of the pressure recovery performance of this component is a widely investigated topic in literature.

To perform the mentioned function, there are two main configurations of the exhaust hood: axial and radial (Figure 1.2). The radial solution reduces the axial length of the machine with significant benefits in terms of costs and greater structural stability, lowering the risk of vibration; however, it leads to significant drawbacks to aerodynamic performance. Indeed, the steam has to turn by 90° degrees in a short distance, generating a complex 3D flow with a strong swirl that increases the aerodynamic losses. The axial configuration is more efficient but it drastically increases the length of the turbine, for this reason, it is used only in small size steam turbines while large scale steam turbines have a radial diffuser, as illustrated in Figure 1.3, with the condenser located below the rotating axis of the turbine.

Due to the higher complexity of the flow field and due to the widespread use of this configuration, the radial exhaust hoods are widely investigated in the literature on the contrary respect to the axial one. The latter presents traditional design criteria that can be easily found in the state-of-art of conical annular diffuser. In this work both the exhaust hood configurations are studied, however, the optimization procedure is focused only on the radial one.

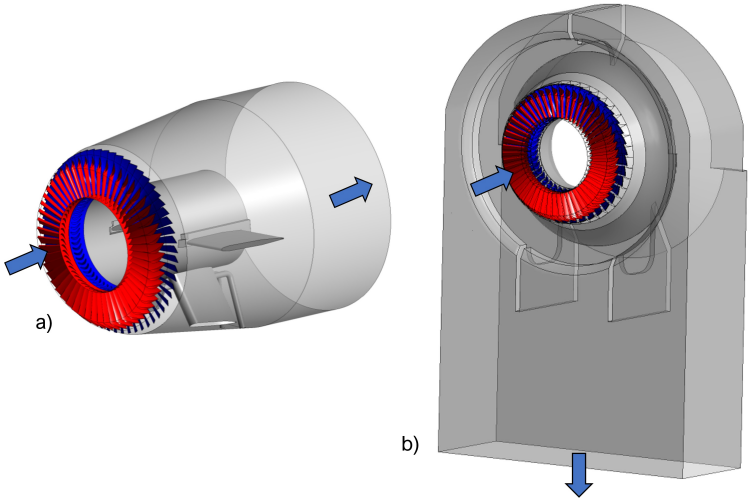

Figure 1.2: Different configurations of exhaust system: a) Axial b) Radial

Before presenting the state-of-art of steam turbine exhaust hood, it is worth clarifying the nomenclature of the different surfaces of this component and the most impacting geometric areas since the influence of these areas on the pressure recovery performance is a recurring theme. In this regard, in Figure 1.4 a schematic representation of a radial exhaust hood is presented, looking at this image it is interesting highlighting how this component can be divided into two parts: the diffuser, which is the first zone immediately after the LSB where the pressure recovery occurs, and the external casing, which guides the steam from the diffuser to the condenser. The latter does not contribute to the pressure recovery but it is fundamental to limit the pressure losses and therefore avoiding an abrupt drop of the pressure recovery downstream to the diffuser. As will be presented in this work the optimization of both this part of the exhaust hood is essential in order to obtain high aerodynamic performance of the exhaust system.

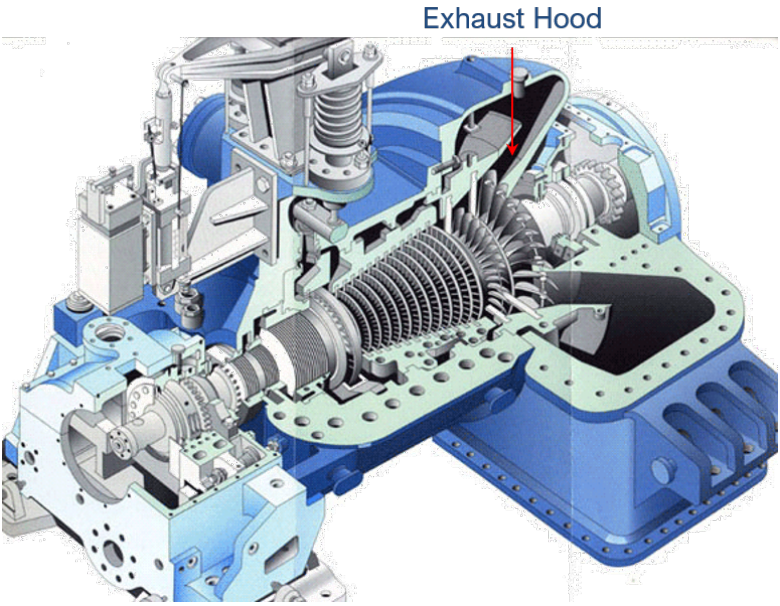

Figure 1.3: Representation of a steam turbine with radial exhaust hood

As clarified by Figure 1.4b and c, the diffuser shape is defined by two surfaces: the steam guide and the bearing cone. They have a strong impact on the performance as will be presented in the section which illustrates key parameters for the optimization process. Finally, in Figure 1.4d the main areas are illustrated, A_0 is the exhaust system inlet area, and its dimension is defined by the rotor blade span-wise dimension and therefore it can not be used as an optimization parameter in the exhaust hood design. As a general criterion, this area should be maximized to reduce the steam velocity at the LSB outlet, optimal velocity values are around 215 m/s [5]. A_1 is the final section of the diffuser, controlling both the area-ratio and the diffuser axial size, this is a key parameter for the optimization of the performance, as well as A_2 and A_3 which are respectively the area in the upper part of the exhaust hood, linked to the

exhaust system maximum height (upper wall in Figure 1.4b), and the area in half joint plane.

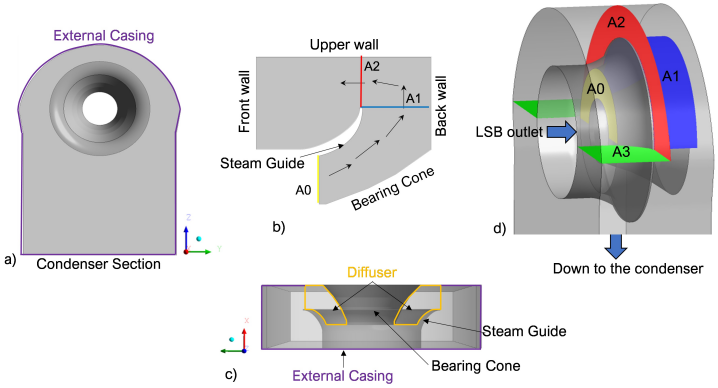

Figure 1.4: a) Front view of a radial exhaust hood b) 2D slice of the upper part of the exhaust hood c) Top view of a radial exhaust hood d)Characteristic areas of the steam turbine exhaust hood

In the following of this chapter, the state-of-art of several steam turbine exhaust system topics will be presented. This has been realized by starting from the extensive review proposed by Burton et al. [12] and integrating it with the most recent investigations.

1.1 Exhaust System Flow Field

This subsection is focused on the flow features which characterize the flow field in the radial exhaust hood. In the last decade, due to the complexity of the flow field and due to the costs related to experimental activities, CFD has become crucial for the understanding of the fluid dynamic behavior within this component. In this regard, Mizumi et al. [13] presented a sector-wise streamlines flow field visualization which can be used to understand the 3D flow field. An example of the application of such technique is reported in Figure 1.5, the fluid domain and the numerical setup used in this CFD simulation are explained later while

in this section it is useful as a qualitative representation of a typical exhaust system flow field. In Figure 1.5a the 2D velocity streamlines computed in Y0 surface (Mid-Surface) are reported. the streamlines show a wide separation area originating from the bearing cone wall which drastically reduces the available passage area, such separation area is called "Hub Cone Separation" or "Bearing Cone Separation" and it has been observed in many different publications. In this regard, Zhang et al. [14] investigated the flow field in the exhaust system with a particle image velocimetry (PIV) highlighting the presence of this separation area, concluding that it is generated by the adverse pressure gradient and by the low kinetic energy of the flow in the boundary layer.

As can be seen by Figure 1.5, the bearing cone separation promotes the onset of a recirculation region, pointed as Secondary Vortex A, which extends along the entire exhaust hood up to the condenser section. Limited information can be found in literature about the secondary vortex since it is associated with small losses if compared with the Exhaust Tip Vortex, that is explained in detail later. By looking at the 3D streamlines reported in Figure 1.5b, it is clear how the magnitude of the secondary vortex drastically decreases with the progression downstream, in line with the findings proposed by Xu et al.[15]and Fu et al.[16].

Finally, both the 2D streamlines and the 3D ones in Figure 1.5b revealed the presence of two counter rotating vortices, called Exhaust Tip Vortices which dominate the flow field within the exhaust hood. Such vortices are the main source of losses in this component, as highlighted by the high value of entropy, and in the with the findings of Munyoki et al. [17].

In figure 1.5a no separation along the steam guide is shown, although several investigations have detected a flow separation along this surface. However, it is strongly dependent on the Steam Guide geometry and on the modelling of the rotor tip clearance since it has a positive impact on the separation by energizing the flow in the boundary layer.

An important parameter that affects the exhaust hood flow field is the inlet swirl, the effect of this parameter on the axial annular diffuser

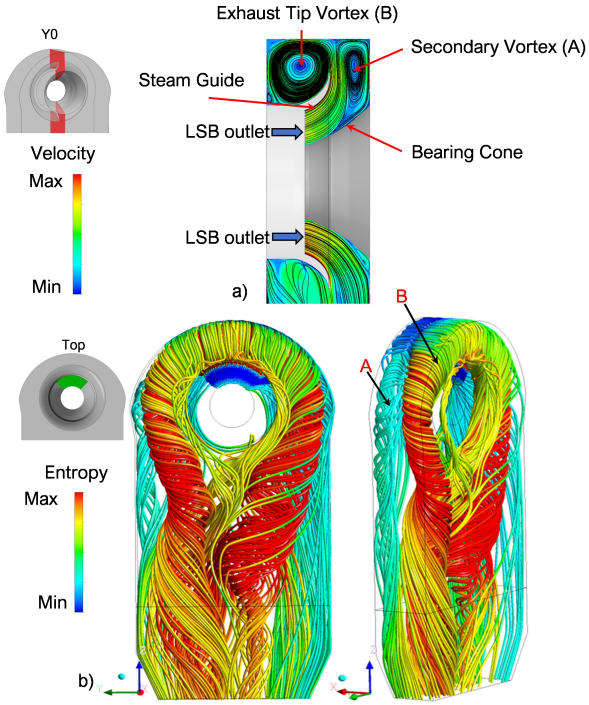

Figure 1.5: Exhaust hood flow field

is well-known [18, 19]: a weak inlet swirl was demonstrated to have a positive effect on the pressure recovery by suppressing the flow separation, respect to a purely axial flow, however, this positive effect decays at high swirl number. However, these studies are focused only on the diffuser neglecting the coupling with the rear stage, and consequently, they do not consider the effect of inhomogeneous flow at diffuser inlet. Indeed, Uvarov et al. [20] have demonstrated the limited applicability of these concepts to a turbine exhaust system. Although the literature about stand-alone axial annular diffusers can not be directly exploited, the strong effect of the swirl in radial exhaust hood has still been proven by Fu et al. [16, 21].

Specifically, the effect of the swirl angle at different span positions at the diffuser inlet was studied, the results show that a high swirl near the hub reduces the pressure recovery factor, due to flow separation, while a high swirl near the tip has a positive effect on the pressure recovery. Similar conclusions were presented by Yin et al. [22] by using the post-processing approach proposed by Mizumi et al. [13], according to the authors the inlet swirl is the most important parameter which affects the pressure recovery. Beveers et al.[23] quantified the impact of this separation on the exhaust system performance demonstrating that the earlier is the separation the less is pressure recovered.

1.2 Exhaust System Computational Methods

In this section, the main numerical modeling strategies used to study the flow field within the exhaust hood are presented. As already mentioned, CFD has become crucial for the design of the exhaust system. From a numerical point of view, the flow in the exhaust system is extremely complex, not only for the three-dimensional and unsteady nature of the flow but even more, because it is necessary to consider the presence of the last stage of the low-pressure turbine in the fluid domain, due to strong coupling between the exhaust hood and the turbine exit flow.

Modeling the unsteady full 3D turbine stage coupled to the exhaust system results in a remarkable number of grid elements with a significant computational effort. Such an approach is not suitable as a design tool, however, it is essential for the off-design analysis where the flow unsteadiness can not be neglected. In this work, unsteady simulations have been carried out to investigate the flow field unsteadiness in off-design operating conditions, the state-of-art of this topic is widely explained in the following subsection.

Many simplified numerical procedures have been developed to reduce the computational costs respect to the already cited full 3D unsteady simulations. The initial assumptions aimed at simulating the exhaust hood only neglecting the strong fluid dynamic coupling between this and the

rear stage. However, it was demonstrated the imposition of the uniform boundary at the exhaust hood inlet does not determine the resolution of the correct flow field within this component [24, 25]. Other strategies are focused on the definition of empirical boundary conditions to be imposed at the exhaust hood inlet, still considering the exhaust hood only, this can help to improve the fidelity of the numerical simulations [26, 27, 28].

In order to explain the importance of the rear stage-diffuser interaction, it is worth mentioning that in radial exhaust hood, due to non-axisymmetric shape, a significant pressure gradient exists between the upper and the lower part of this component. This pressure gradient leads to a different loading of the rotor blades during their rotation causing different exit velocities and swirl angles which consequently affect the flow field in the exhaust hood. It can be concluded that the presence of the rear stage in the fluid domain is essential. In this regard, Liu and Hynes [24] presented a simplified model based on actuator disk theory. This method approximates the last stage as a zero-thickness disk to produce the asymmetry of the flow at the diffuser inlet and to consider the losses generation across the blade passage. In the second part of the study [24], they applied this method to improve the performance of the exhaust hood. Recently, Sadasivan et al.[29, 30] have applied the actuator disk model, with rotor tip clearance effect included, to study the physics of flow behavior in the exhaust hood.

With the aim of considering the last stage-exhaust hood interaction, Beevers et al. [23] have presented a two steps procedure, based on one-way coupling, called exhaust design system (EDS), inspired by the methodologies proposed by Benim [31] several years before. In the first step, the fluid domain considers the presence of the last stage with a single blade passage and a slice of the exhaust system to create a database of 2D diffuser inlet profiles in different operating conditions. In the second step, CFD calculations with the entire exhaust hood, without the last stage, are carried out with an iterative approach to impose the boundary conditions at the hood inlet starting from the solutions stored in the database. The main limit of the EDS method is related to the low range

of operating conditions that can be computed due to numerical stability problems [10, 32]. A similar procedure, which uses an external iteration method, has been used by Fu et al. [33] to couple the last stage and exhaust system to optimize diffuser performance.

In order to perform a single-step calculation, the presence of all the components in a single CFD simulation can be modeled, exploiting different coupling strategies to link the stator to the rotor and the rotor to the exhaust hood domains. The most adopted strategies allow solving steady Reynolds averaged Navier–Stokes (RANS) equations instead of transient ones. For instance, the frozen rotor approach produces a steady-state solution by freezing the rotor, therefore fixing the relative orientation of the component across the interface. In the last years, the frozen rotor approach has been successfully used to couple the rear stage with the exhaust system with great results in terms of accuracy of pressure recovery prediction [33, 34, 35, 36, 37]; however, it still requires high computational effort, since the full annulus of the rear stage has to be modeled, and hence, it is hardy to use for an exhaust system optimization procedure. Živný et al. [37] presented a numerical validation of the frozen rotor interface by comparing CFD results with experiments. The comparison shows a good agreement in pressure, velocity and wetness prediction in both exhaust hood inlet and outlet sections.

A computationally cheaper alternative to the frozen rotor interface is the mixing plane approach that usually solves one blade passage, performing a circumferential averaging of the fluxes through the interfaces. This method, widely used in turbomachinery applications, allows a considerable reduction of computational costs respect to a frozen rotor with good results in terms of accuracy. Fan et al. [38] applied a mixing plane interface to model the interaction between the exhaust hood and the rear stage showing significant differences respect to the single exhaust hood model. Verstraete et al. [39] evaluated the diffuser performance in design and off-design operating through CFD simulations, including the last turbine stage with the mixing plane model. The main limit of the mixing plane approach is related to the loss of the flow circumferential

non-uniformity at the diffuser inlet. In this regard, Burton et al. [40] presented a novel direct coupling approach, based on a nonlinear harmonic method capable to capture a non-uniformity of the flow at the exhaust hood inlet, the comparison with the mixing plane shows improvement in the rear stage-exhaust hood interaction modeling. In addition, such an approach allows a significant reduction in computational time if compared with the frozen rotor interface.

The limitations of the mixing plane have been overcome also with the novel coupling approach proposed by Stein et al. [10]. Such an approach is based on the use of multiple mixing planes in a steady-state numerical simulation still allowing circumferential non-uniformity of the flow. The multiple mixing plane has been compared both with a steady-state Frozen Rotor computation and with a full annulus transient simulation, showing a good agreement in terms of both pressure recovery factor prediction and flow field resolution with a significant reduction in terms of computational costs. The multiple mixing plane model is capable of predicting a similar flow field respect to the other more computational demanding strategies, the main difference is in the blade wakes, which are smeared out by the mixing plane. However, the comparison between Frozen Rotor and Transient Rotor Stator highlighted how the Frozen Rotor identified intense wakes in the Mach number which are instead smeared by the transient simulation.

In the same work, the authors have demonstrated the limits of the one-way coupling, such as the presented EDS method, which is not able to provide stable results in the same range of operating conditions simulated with the direct approaches. The multiple mixing plane approach has been recently validated by Mabro et al. [41] with a comparison with experimental data showing that it is capable of predicting the flow field.

Stanciu et al. [42] performed a comparison between different interface methodologies including mixing plane, frozen rotor up to detailed full 3D unsteady simulations. According to the authors, the steady-state approaches tend to overestimate the exhaust hood and last stage performance.

Regardless of the used domain coupling approach, several researchers have highlighted the importance of the blade tip clearance jet modeling on the flow structure within the exhaust system. Zimmermann and Stetter [43] experimentally studied the influence of tip clearance gap in a low-pressure model turbine with a radial diffuser, the results show an increase in the diffuser pressure recovery with increased clearance. This finding has been confirmed by the numerical simulations presented by Willinger and Haselbacher [44]. The physical explanation behind this trend is the high-velocity jet, due to rotor clearance, which energizes the boundary layer along the steam guide avoiding the separation, leading to a significant rise of the pressure recovery as also demonstrated by Becker and Burton [45, 46].

Most of the investigations found in the state-of-art are based on numerical modeling and therefore quantification of the error respect to the experiment should be useful to assess the accuracy of such models on the flow field prediction. As a general trend, the experimental measurements highlighted an overestimation of pressure recovery performances calculated with CFD [21, 23], quantified by Liu et al. [28] in 7%. The quantification of the overestimation is strongly related to the numerical setup used, possible reasons behind this trend may be due to unrealistic boundary conditions, not suitable turbulence models, geometric simplifications, or wetness effect neglect. The differences between experiment and CFD are higher in the strong off-design cases where the hub cone separation is wide, in particular, significant differences are highlighted in the separation area prediction. This supports the thesis that the differences between experiment and CFD may be mainly related to an unsuitable turbulence model. By considering the physics involved in this problem, the SST k-ω turbulence model seems the most suitable for this application due to its high accuracy in predicting the strong separated flow, as demonstrated by Bardina et al.[47].

Another source of error in the numerical modeling may be related to the wetness effect, indeed, the flow at the LSB outlet has a moisture

content of 6-14% [48]. According to the findings proposed by Kasilov [48] the effect of wetness on the exhaust system performance depends on the performance itself. For high-performance exhaust hood, the losses due to wetness are greater if compared to the ones in a low-performance exhaust hood.

Tanuma et al.[49] presented 3D unsteady numerical results obtained with a non-equilibrium condensation model, the comparison with experiments shows that the wetness effect can be numerically reproduced. It is worth highlighting how this investigation demonstrates how the large vortex structures within the exhaust hood decrease the wetness due to the entropy generated. In addition, the authors reported the effect of inlet wetness on the vortices size showing that an increase in the wetness from 3.5% to 8.2% results in an appreciable change in the vortex size. The non-equilibrium condensation model applied to low-pressure turbine has been validated also by M. Grubel and M. Schatz [50, 51] through a comparison with experimental data.

Sadasivan et al. [30] evaluate the effects of wetness on the flow structure and the pressure recovery of steam turbine exhaust hood by using an Eulerian–Eulerian multi-phase equations with 3D CFD. On the contrary, respect what was previously shown by Kasilov [48], it is found that the wetness effect enhances the pressure recovery due to a reduction of vortices strength. In addition, the presence of liquid droplets leads to a decrease in turbulence intensity and consequently to a decrease in losses.

fThe simplifications of the fluid domain may be another cause of the difference between experiment and CFD [52], among these, neglecting the internal structural struts of the exhaust hood is one of the most adopted. Stein et al. [53] evaluated the effect of struts by performing detailed CFD simulations on a steam turbine exhaust system with the internal struts included. By looking at the results it is clear how the simplification of the fluid domain may lead to significant errors in the losses prediction. In the second part of this work, Telschow et al. [54] presented a 1D tool, calibrated on 3D CFD, for the estimation of the pressure losses within the exhaust system. Xu et al. [55] numerically investigated the

flow field in the exhaust hood with and without the steam extraction pipelines demonstrating that a significant increase of losses (and decrease of pressure recovery) is linked to these features.

To summarize, this literature review has shown how for a proper resolution of the flow field within the exhaust hood it is essential to consider the presence of the rear stage, with rotor clearance included, in the fluid domain. In order to avoid computationally expensive 3D unsteady simulations, a different domain coupling strategy can be adopted: starting from the less expensive mixing plane up to the high computationally demanding frozen rotor. The choice between these is strongly related to the applications, the mixing plane is a valid strategy for the optimization approaches which require a high number of numerical simulations while the frozen rotor can be adopted as a validation tool.

Concerning the accuracy of the numerical model prediction, as a general trend, a slight overestimation of the pressure recovery performance of the numerical simulation respect to the experiments is reported. A possible explanation behind this trend may be due to the numerical setup, for instance, a coarse mesh, a not suitable turbulence model or geometric simplifications. Among the geometric simplification, the most adopted is neglecting the structural struts which have been demonstrated to have a significant impact on the exhaust hood performance. Also, the wetness effects may be a source of error in the numerical modeling, they can indeed affect the vortices strength and consequently the pressure recovery performances. Concerning the turbulence model, the SST k-ω is probably the most suitable for this application, due to its high accuracy in predicting the strongly separated flow.

1.3 Aerodynamic Optimization Strategies

This section offers a theoretical (in the first part) and applied (in the second one) overview of the numerical optimization approaches. In the first part, the idea and theory behind the numerical approaches used in literature and in this work for the aerodynamic optimization is presented,

while the second part is focused on the state-of-art of application of such methods in the steam turbine exhaust hood context.

1.3.1 Numerical Models for Surrogate-based analysis and optimization

As already mentioned, in this subsection the main numerical models useful to perform optimization procedure will be presented, highlighting concepts, methods, and techniques used in such models. A specific focus on the techniques used in this work is considered.

In the last years, The development of computer technology has fostered the spread of the CFD into many engineering problems. Numerical simulations have been widely used not only for more in-depth knowledge of fluid dynamic phenomena but also to improve performance. Historically, the latter task was accomplished by using trial-and-error design procedures, often based on the designer's experience. At the present time, such procedures are almost completely replaced by rigorous optimization methodologies allowing the definition of optimized geometry in a more fast and more efficient way. Among these, the Surrogate-Based analysis and Optimization (SBAO) has proven to be an effective tool for several engineering applications, in particular for computationally expensive models. The literature review proposed by Quiepo et al. [56] on SBAO methodologies clarifies how such procedures have been widely used in the turbomachinery context ranging from airfoil shape optimization [57, 58], aerodynamic diffuser optimization [59] up to supersonic turbine [60, 61].

Usually, the definition of a surrogate model follows specific key steps, as in the case of the approach proposed in this work. Such steps are generically presented in Figure 1.6.

The first essential step is the Design of Experiment (DOE), in this step the input variables of the procedure are selected together with the sampling strategy to be used to generate the design points. The latter are then simulated in the following step, is therefore fundamental to select the number of design points as the best trade-off between the numerical costs and the desired accuracy in the surrogate model prediction. As presented

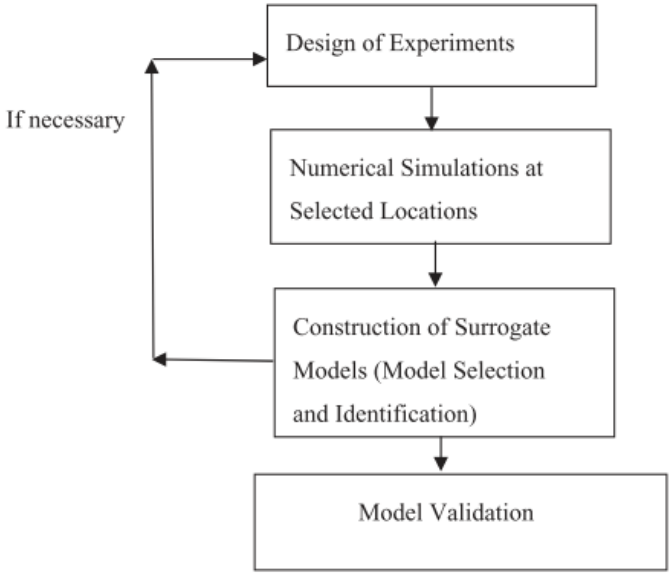

Figure 1.6: Key steps for the application of Surrogate-Based Analysis
Figure adapted by [56]

later, such a number depends on the sampling strategy used. Once the numerical simulations are carried out the results are used to build the surrogate model, the accuracy of which can be verified with different strategies, in the model validation strategy, allowing to understand if the surrogate model is ready for the following optimization step. If not, additional design points are required to increase the accuracy of the model.

By considering the idea behind the definition of a surrogate model, it seems clear how it is an inverse problem aimed at determining a continuous function (f) of a set of design variables starting from an initial data set. The output of the model can be therefore defined as follow:

$$f_p(\mathbf{x}) = \hat{f}(\mathbf{x}) + \varepsilon(\mathbf{x}) \tag{1.4}$$

Where $\hat{f}$ represents the surrogate model and ε is the error associated

with the surrogate model prediction.

In the application where the surrogate model is based on numerical simulations, an error linked to the numerical noise is likely to exist. In order to better explain the concept of error it is worth considering two different parameters linked to it:

- Bias: quantifies how much the surrogate model prediction differs from the true value.
- Variance: quantifies how much the surrogate model prediction is sensitive to the selected data set.

By assuming E_{ADS} as the expected value, the following equations can be used to calculate these parameters:

$$E_{\mathrm{bias}^2}(\mathbf{x}) = \left\{ E_{\mathrm{ADS}}[\hat{f}(\mathbf{x})] - f(\mathbf{x}) \right\}^2 \tag{1.5}$$

$$E_{\mathrm{var}}(\mathbf{x}) = E_{\mathrm{ADS}} \left[\hat{f}(\mathbf{x}) - E_{\mathrm{ADS}}[\hat{f}(\mathbf{x})] \right]^2 \tag{1.6}$$

Usually, these parameters are in a natural trade-off since a surrogate model that fits well a data set presents a large variance. As a general strategy, a high number of design points can help to both increase the bias and decrease the variance. However, the number of points is often limited by the numerical cost and consequently a balance between these parameters should be sought. The bias error can be also reduced by a proper selection of the sampling algorithm used in the DOE.

A uniform distribution of the samples can help to reduce the bias, however, a full factorial design is often unmanageable from a computational costs point of view. As an alternative strategy, an equally spaced sampling can be reached maximizing the minimum distances among design points. Among the alternative strategies, it is worth mentioning orthogonal arrays (OA) [62] or the Latin Hypercube Sampling (LHS) [63]. The latter is the one used in the presented approach and it is therefore discussed in detail. LHS is a stratified sampling strategy with the constraint that each of the input variables (x_k) has all portions of its distribution represented

by input values. This concept is illustrated in Figure 1.7, which shows how by considering a number of samples N_s=6, the LHS can be built by diving the range of each input variable (reported in x and y-axis) into a number of N_s strata of equal marginal probability $1/N_s$, in each stratum is then inserted a design point.

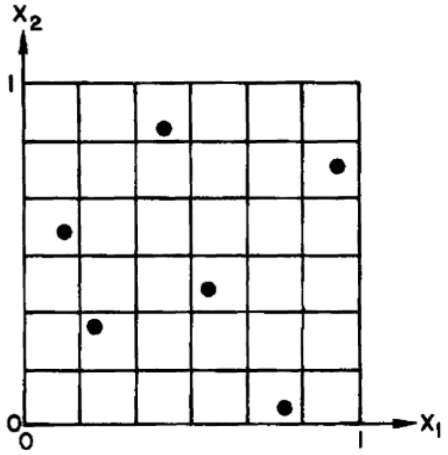

Figure 1.7: Schematic representation of the Latin Hypercube Sampling strategy with Ns=6 and Nv=2.
Figure adapted by [56]

As depicted in Figure 1.6, once selected the design points and simulated them, the following step is the definition of the surrogate model. The main distinction among these is if they are parametric or non-parametric models. The parametric models imply the knowledge a priori of the global functional form of the relationship between the response variable and the design variables, while the non-parametric ones use distinct kinds of functions in different regions of the data in order to obtain an optimal fitting. In this work, due to the difficulty in predicting the shape of the global function, a non-parametric method has been used. Among the several non-parametric models, the Non-Parametric Regression Method

available in Ansys Design Exploration has been used. Such a model uses the Support Vector Regression (SVR) method to optimally fit the data. The SVR is an optimization problem that entails finding the maximum margin separating the hyperplane while correctly classifying as many training points as possible. Such a task is accomplished by introducing ϵ-insensitive region around the function, called ϵ tube. This implies the reformulation of the problem in the research of a tube that best approximates the function, while at the same time balancing model complexity and prediction error. The hyperplane is represented in terms of support vectors, which are training samples that lie outside the boundary of the tube. In other words, SVR gives the flexibility to define how much error is acceptable in the model and finds the appropriate hyperplane to fit the data.

This concept is illustrated in Figure 1.8 where a mono-dimensional example of linear SVR is reported. The data points out from the ϵ-tube are not used to build the model. The role of ξ is discussed later.

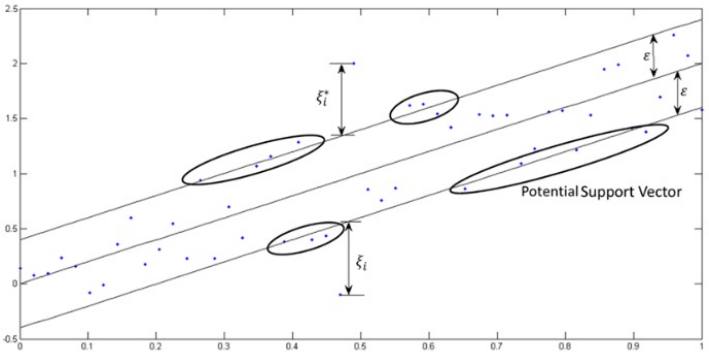

Figure 1.8: One dimensional linear SVR.
Figure adapted by [64]

Considering a general polynomial regression:

$$f(x,w) = \sum_{i=1}^{M} w_i x^i, x \in \mathbb{R}, w \in \mathbb{R}^M \tag{1.7}$$

Finding the narrowest tube centered around the surface, which is the primary objective of SVR, means solve the following equation:

$$\min_{w} \frac{1}{2}\|w\|^2 \tag{1.8}$$

with the constrain of the error minimization:

$$|y_i - w_i x_i| \leq \varepsilon \tag{1.9}$$

Considering the equation 1.7, it is worth mentioning how the higher is the number of w_i different from zero the higher is the order of the solution. For instance, the 0th-order polynomial solution has a very large deviation from the desired outputs, and thus, a large error. On the other hand, a high order solution has an almost zero error but a high complexity and consequently, it is likely to over-fit the data set. Therefore, it seems clear how the magnitude of w acts as a regularizing term by providing control on the optimization problem in both the accuracy and the complexity of the solution. In addition, the introduction of the ϵ-insensitive region allows the reduction of the effect of the noise, making the model more robust. However, on the basis of ϵ extension, significant information may be lost. This problem can be overcome by considering a soft-margin approach based on slack variables ξ. These variables determine how many points can be tolerated outside from ϵ-tube, as illustrated in Figure 1.8.

To summarize, considering the equations 1.8 and 1.9, the optimization problem for the application of SVR method can be written:

$$\begin{gathered} \min \tfrac{1}{2}\|w\|^2 + C\sum_{i=1}^{N} \xi_i + \xi_i^*, \\ y_i - w^T x_i \leq \varepsilon + \xi_i^* \quad i = 1 \ldots N \\ w^T x_i - y_i \leq \varepsilon + \xi_i \quad i = 1 \ldots N \\ \xi_i, \xi_i^* \geq 0 \quad i = 1 \ldots N \end{gathered} \tag{1.10}$$

Where C is regularization and tuneable parameter useful to target

the problem to minimize the flatness or the error for the multi-objective optimization problem. This constrained quadratic optimization problem can be solved by finding the Lagrangian.

An alternative to the non-parametric regression is the Kriging Modelling (KRG). In this work, this model has been tested and compared with the non-parametric regression, such comparison shows how for the present application the latter is the more suitable. The explanation can be found by considering the main difference between these models, indeed, the KRG model, in contrast to the concept already shown for the non-parametric regression, automatically fits through all data points and, in the present work application, this leads to an overfitting problem. The detailed explanation of the mathematical derivation behind the KRG is out of the scope of this work, however, it is interesting highlighting the working principle of this method. The KRG method estimates the value of a function in some unsampled location as the sum of a linear model plus a fluctuating component composed of low and high-frequency variation components.

The construction of the surrogate model is usually followed by a verification step aimed at assessing the quality of the surrogate prediction. The simplest scheme which can be used for this step is the so-called Sample Split (SP). It is based on a distinction between training and test points, the former are used to build the surrogate model while the latter to check its quality allowing to compute an unbiased estimate of the generalization error. The main limit of this approach is the high variance often obtained in the error estimation. An improvement of this scheme is the Cross-Validation (CV). The scheme is based on the definition of k subsets, the surrogate model is constructed k times and each time leaving out one subset from training and using it to compute the error. The main improvement respect to the SP is the lower variance of the error, which is obtained by considering that some design points are used both as test and training points. The main drawback is the necessity to compute the surrogate model k-times.

Once verified the quality of the surrogate model, it can be used by an

optimization algorithm to find out an optimal solution for the investigated problem. It is worth highlighting both the fundamental importance of the surrogate model quality check since it is interrogated by the optimization algorithm, and the huge saving in computational cost and time respect a direct optimization approach, which uses the numerical simulation (i.e. CFD) to identify the optimum.

In this work a multi-objective optimization approach has been used, it aimed at achieving multiple goals by respecting a series of constraints. The traditional schemes used to solve this problem are based on a weight vector that specifies the relative priority of each objective and then combines them into a scalar cost function. Since the objectives are often in conflict, it is not easy to determine an optimal solution. For this reason, the multi-objective optimization methods commonly adopt a set of Pareto optimal solutions, which represent a trade-off between the different objectives. Among the different models used to build the Pareto front, the Evolutionary Algorithms (EAs) are the most efficient, the idea behind this approach is to mimic natural processes that are inherently multi-objective. Unlike the classical optimization schemes, the EAs identify many different Pareto-optimal solutions in a single run allowing significant speed-up respect to the classical scheme. Several EAs exist, the one used and described in detail in this work is the Multi-Objective Genetic Algorithm (MOGA). However, all the EAs follow the same principle inspired by the evolution of the natural process, where the individuals represent possible solutions, and a set of individuals (or possible solutions) is called a population.

The first step of an EA consists of the application of a fitness factor to evaluate the population in the objective space, in other words, an assessment of the solution quality; a mating pool is then created by selecting the population from the previous step using a likelihood-based selection criterion, individuals with a high fitness measure are more likely to be selected to the mating pool. This concept can be expressed with the following equation:

$$P_i = \frac{F_i}{\sum_{j=0}^{N} F_j} \tag{1.11}$$

Where P represents the probability of an individual to be selected for the mating pool, while F_i represents the operating fitness of the individual solution and the N is the total number of individuals in the population.

Once built, the mating pool is subjected to a recombination and mutation process which determines a second-generation population. The mating pool is an essential step of the procedure since it allows to identify an optimal solution as a consequence of a combination of the high-quality individuals of the previous generation. The solutions with the weaker fitness measures are naturally discarded. A Schematic representation of this process is illustrated in Figure 1.9.

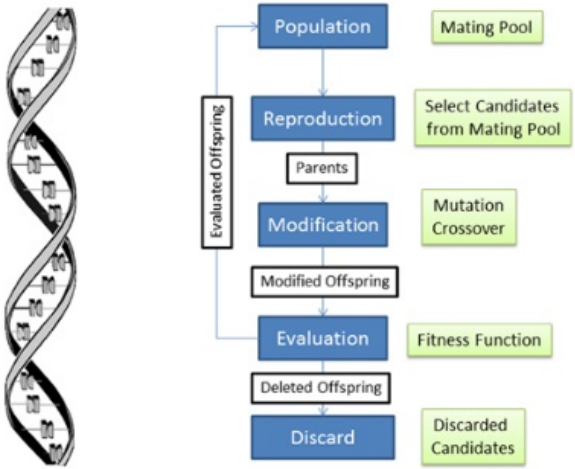

Figure 1.9: Genetic Algorithm scheme
Figure adapted by [64]

1.3.2 State-of-Art of Exhaust System Optimization

The aerodynamic optimization of the exhaust hood is a widely investigated topic in literature since the maximization of the pressure recovery has a direct effect on the steam turbine efficiency. In this subsection, several investigations will be presented, with a specific focus on the most influential exhaust hood geometric parameters and different optimization strategies.

One of the first studies aimed at comparing two different geometries was proposed by Tindell et al. [25], the work is focused on the Steam Guide geometry (illustrated in Figure 1.5) and the results show how a shorter flow guide results in higher performance.

Yoon et al.[65] re-designed a radial exhaust hood for a retrofitting application, however, the new geometry causes a blockage in the upper part of the exhaust system. Such a problem was solved thanks to cut-back of the diffuser in the upper region resulting in a circumferential asymmetry of this component which maximizes the aerodynamic performance.

Yin et al. [22] optimize the bearing cone geometry with a genetic algorithm identifying a more performing geometry. Musch et al. [66] presented an optimization strategy, focused on the steam guide, based on the combination between a through-flow code and boundary layer solver, then the results have been confirmed with 3D CFD. Subsequently, Mush et al. [67] presented an optimization procedure, again focused on the steam guide, based on CFD carried out on a simplified fluid domain validated with a comparison with experiments. The results obtained with CFD have been used to create a meta-model used to identify a more performing geometry allowing a significant increase of performance respect to the baseline geometry.

Mizumi et al.[13] discovered that the upper part of the exhaust hood is the most critical in terms of aerodynamic performance due to the onset of the so-called Exhaust Tip Vortex (reported in Figure 1.5). Based on these findings, they proposed a geometric adjustment of the exhaust hood with additional ducts capable to decrease the vortices' strength verifying the improvement on a scaled test rig. In the following study, Mizumi and

Ishibashi [68] proposed a design method for the exhaust hood based on performance charts calculated with CFD simulations. In these charts they analyzed the effect of different geometric parameters and thermodynamic conditions, however, the exhaust hood performances are calculated with a single hood calculation neglecting the effect of the rear stage.

Kreitmeier and Greim [26] highlighted the central role of the kink angles of both steam guide and the bearing cone surfaces by presenting an optimization procedure of such angles. Fan et al. [38] presented a design of experiment analysis based on the Taguchi method, this study revealed how the bearing cone kink angle and the diffuser length are the most important parameters affecting the exhaust system performance. Cao et al. [69] investigated the influence of different steam guide tilt angles, the results show that the pressure recovery increases by gradually increasing the steam guide angle.

Wang et al. [70] presented an optimization procedure with 3D CFD aimed at maximizing the pressure recovery factor of the exhaust hood. The bearing cone and steam guide surfaces have been parameterized with two cubic Bezier curves and a Kriging surrogate model has been used to link the input parameter with the objective function. The optimal geometry presents a significant improvement in the performance respect to the baseline one. A similar approach was proposed by Verstraete et al. [36] based on a numerical optimization method with an evolutionary algorithm and a 3D CFD applied on the exhaust system diffuser, however, only the exhaust hood is considered in the fluid domain. The last stage-exhaust hood interaction is modeled in a decoupled way by imposing as inlet boundary condition the flow field extrapolated from a Frozen Rotor calculation. In the extension of the work [39], they evaluated the diffuser performance in design and off-design operating through CFD simulations, including the last turbine stage with the mixing plane model. As a final validation of the optimized geometry, they compare results with a frozen rotor computation. As clarified by these investigations [36, 70], the cubic Bezier curves represent the state-of-art for the design of the steam guide, however, Ding and Xu [71] proposed a different method

based on Minimum Energy Curves (MEC) which allows optimizing the diffuser performance with a speedup of 100 times the computational time and fewer input parameters respect to the Bezier Curve. In a subsequent study, Ding et al. [72] presented a numerical parametric study aimed at investigating the effect of both the diffuser geometry variation, with the procedure already presented [71], and the restaggering of the last stage rotor blades. The restaggering of the LSB was demonstrated to be an efficient way to control the conditions at the diffuser inlet. In addition, they demonstrated that the geometric optimization of the diffuser is relatively independent of the blade restaggering, meaning that these two components can be optimized separately. They also found that optimal values of the diffuser geometric parameters are linked to the operating conditions.

Fu et al. [33] tested different diffuser casing configurations to improve the aerodynamic performance of the exhaust hood. Liu and Hynes [73] compared two different exhaust hood geometries, the first one presents a gradually increasing cross-sectional area from A_2 to A_3 (in Figure 1.4) while in the other it remains constant. The latter leads to a flow acceleration and consequently to pressure recovery drop. This effect was also demonstrated by Finzel et al. [74] by experimentally investigating a full-scale Mach number test rig of an exhaust hood. The influence of A_2 and A_3 has been assessed and the result show how initially a small decrease of this area leads to a small change in performance for both the investigated operating conditions, while when this area is excessively restricted the performance drops abruptly. Concerning A_3, a stronger effect is shown, in particular in the operating condition characterized by 1.2 Mach at the tip, and also in this case an excessive reduction of this area leads to a decline of the performance.

Similar results were presented by Taylor et al. [32] by carrying out numerical simulations with the EDS method already presented in the Computational Methods sections and with experiments. The effect of the exhaust hood dimensions have been investigated, acting on the exhaust hood width, maximum height and diffuser length, (which affects

respectively A_3, A_2 and A_1 in Figure 1.4) showing a drastic reduction of the pressure recovery performance when the flow passage areas are significantly restricted.

The same test rig of Finzel et al.[74] was also investigated by Munyoki et al. [17] by performing numerical simulations to further enhance the knowledge about the main sources of losses within the exhaust hood, highlighting the importance of swirl flows. In subsequent studies [75], the same authors also investigated the influence of hood height variation but in this case, the influence of higher height respect to the baseline is assessed in order to discover an optimum value of A_2. They found that the optimal value is linked to the operating condition and a reduction or an increase of the hood height respect to this value leads to a decline in performance. The optimal geometry presents a pressure recovery factor improvement up to 9%. Finally, in an extension of this work Munyoki et al. [76] numerically showed a geometric solution to reduce the exhaust hood tip vortex (Figure 1.5) strength and to suppress the steam guide separation, such solution is based on flow deflectors in the upper region of the exhaust hood and it allows a significant increase of performance up to 20% in design condition and up to 40% in off-design condition.

1.4 Off-Design Operating Conditions

The studies presented in the previous section aimed at maximizing the exhaust hood performance, which is a crucial point when the steam turbine operates in design operating conditions. However, in the already presented energy scenario, due to intrinsic variability of the green-energy resources, the steam turbines address the need to increase their flexibility to ensure the stable functioning of the power grid. This higher flexibility has led to radical changes in steam turbine design practices, which, traditionally, were designed to operate at fixed conditions and now they have also to operate at low loads. During low load operation mode the machine experience a reduction of the volume flow, when volume flow reaches almost 30% respect to the design value the last stage acts as a

compressor extracting power from the shaft, this operation mode is known as ventilation and it is illustrated in Figure 1.10a.

In LVF conditions the optimization of the performance is no longer of primary importance since the LSB is no longer generating power while the focus is moved on the structural integrity of the last stage rotor blades. They may indeed experience non-synchronous aerodynamic excitations triggered by the onset of unsteady rotating instabilities. The dynamic stresses induced by these phenomena, reported Figure 1.10b, could be extremely dangerous since they are really hard to predict during the design process. In addition, such stresses are superimposed to the high stresses caused by centrifugal forces leading to LSB High Cycle Fatigue (HCF) failure.

Due to the significant fluid dynamic complexity of this phenomenon, the determination of the off-design alternating stress is not yet included in the industry design practices. The latter are usually based on avoiding the resonant responses at turbine running speed, therefore neglecting the non-synchronous aerodynamic excitations in LVF conditions, which are measured in engine test once the design phase is largely completed. Under these conditions, the only solution is to conservatively design low-pressure blades by over dimensioning the blade stiffness, for instance, adding the snubbers. In light of the above, the integration in the design process of a numerical procedure to characterize the unsteady fluid behavior during LFV conditions seems of primary importance.

As stated by Megerle et al. [78], the first question which arises by thinking about this engineering problem is the link between the fluid and the structure, more specifically: it is an aero-mechanical stability phenomenon or is just an inherent fluid dynamic one. Recently, Bessone et al.[79] and Pinelli et al. [80] presented an extensive experimental and numerical campaign, split in a two-part paper, aimed at characterizing the flutter behavior of a newly designed last stage blade at very low load operations. Both numerical and experimental results are in agreement in showing that blade flutter stability is reliable for low-pressure turbines operating under low-load conditions. These results are confirmed also

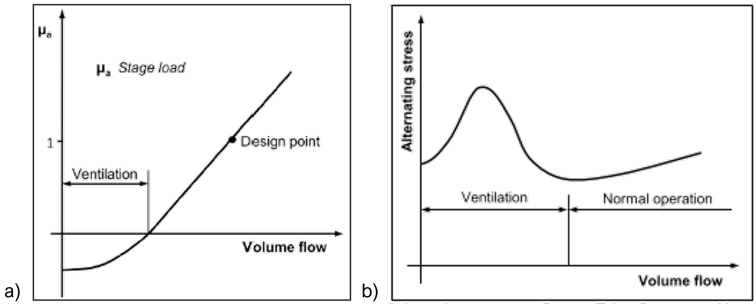

Figure 1.10: a) Stage load against volume flow b) Alternating stresses against volume flow, Figure adapted by [77]

by Pinelli et al. [81] with different low-pressure turbine blades. In the light of these investigations and as will be further shown in the following of this literature review, there are pieces of evidence of the purely fluid dynamic nature of the blade vibrations under LVF conditions.

Another potentially dangerous effect correlated to LVF conditions is the steam increase of temperature due to windage [82, 83, 84], which could lead to creep, rubbing or blade failure. This topic will not be discussed in this work while significant importance will be reserved for flow-induced vibrations.

During the LVF conditions, the flow field in the last stage presents the characteristic behavior shown in Figure 1.11. The low reaction at the hub implies that such a section is the first one affected by the reduction of the volume flow, indeed, the flow can not pass throw the root of the blades and it is centrifuged towards the tip generating a separation region in the diffuser behind the rotor blades. Another recirculation region, called torus vortex in the figure, appears in the axial gap between stator and rotor. This vortex, by rotating in the circumferential direction, may lead to non-synchronous aerodynamic excitations of the LSB.

Many researchers have identified the flow field reported in Figure 1.11 in the last stages of the low-pressure turbine, however, the major differences among these are the onset and the size of the separation zone,

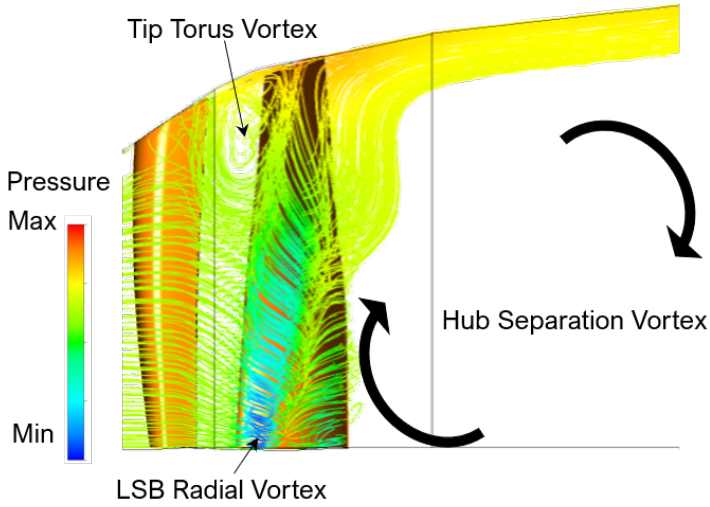

Figure 1.11: Characteristic flow field in last stage during LVF conditions

probably because they are related to the turbine geometry or affected by some modeling uncertainties. The common trait among the studies on this topic is instead the increase in dynamic loading in the LSB during LVF conditions, this phenomenon has been identified 50-years ago, starting from Soviet Union studies in the 1970s. Shnee Et al. [85, 86] presented experimental results obtained by monitoring the LSB with strain gauges during LVF conditions. The measurements highlighted a peak in blade stresses 2-3 times higher respect to the design case when ventilation of the last stage occurred. Similar conclusions were presented by Gloger et al.[77], this study identifies the operating condition with maximum blade stresses when the volume flow is 30% of the zero work volume flow.

Schmidt et al. [87] contributed on this topic by using unsteady pressure probes in a four-stage air turbine showing the peak of pressure fluctuations in a volume flow between 10 and 25% respect to the design one without detecting any blade vibration in such conditions; This would

seem to confirm the fluid dynamic nature of the phenomenon since the unsteady pressure fluctuations in the last stage of the steam turbine are not generated by the blade vibration but they have the potential to trigger them. The pressure fluctuations were generated by four-five pressure cells moving in the circumferential direction with half the rotor speed; similar fluid dynamic behavior has been widely investigated in the compressor rotating stall.

According to Shnee et al. [86], the pressure cells responsible for blade vibration are located in the tip region between the last stage stator and the rotor, while the hub region of separation behind the rotor was characterized by the minimum pressure fluctuations, due to the low energy of the separation zone. It is worth highlighting how the latter result is in disagreement with others reported in the following of this literature review which identifies flow unsteadiness also in correspondence of the hub separation vortex. The maximum of the pressure fluctuations was almost 16% of the pressure drop across the last stage in design conditions. Another interesting finding presented by Shnee et al.[86] was the demonstration of the non-synchronicity of this phenomenon with the rotor rotational frequency.

W Gerschutz et al [88] carried out an experimental investigation on two different three-stage LP steam turbines during ventilation operating conditions, with flow rates between 0 and 30% of the design. In order to catch the unsteady pressure fluctuations, fast response probes were developed while the blade stresses were measured thanks to the strain gauges. The main results of this work are presented in Figure 1.12 together with the experimental setup.

Concerning the blade structural behavior, the study reported strong vibration in the first turbine triggered by aerodynamic excitations at the resonant frequency of the second mode in correspondence of a flow coefficient of 0.13, as illustrated in Figure 1.12b. On the contrary, no resonance was identified in the second turbine up to the fourth mode and the highest vibrations were measured during the zero flow condition, meaning that this phenomenon is strongly geometry-dependent.

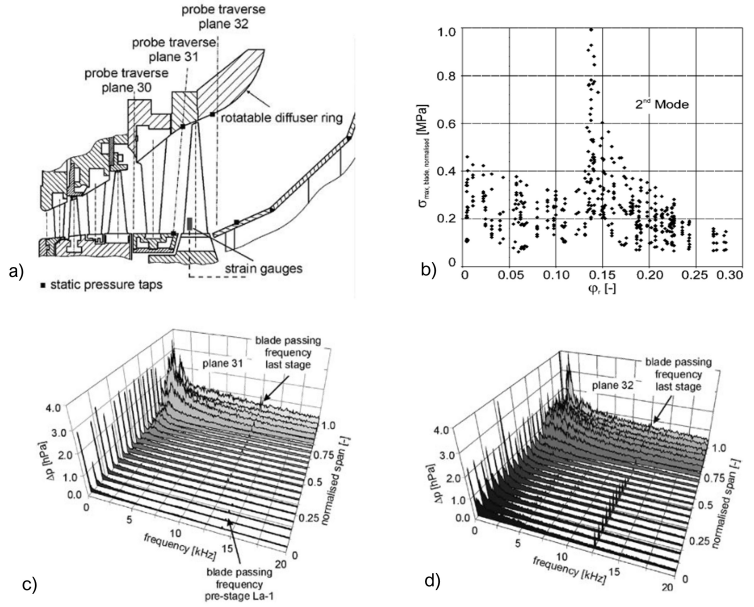

Figure 1.12: a) Experimental setup b) Second mode dynamic stresses at different flow coefficients c) Frequency spectra of pressure signal in plane 31 for flow coefficient of 0.13 d) Frequency spectra of pressure signal in plane 32 for flow coefficient of 0.13
Figure adapted by [88]

From a fluid dynamic point of view, the results are presented in Figure 1.12c, 1.12d in terms of frequency spectra of the pressure signals. In plane 31 located between the last stage stator and rotor, in addition to the blade passing frequency of the previous last stage rotor, a region of high amplitude can be seen at low frequency with a peak of amplitudes at 95% of the span, these disturbances are potentially responsible for the blade vibration reported in Figure 1.12a. A high level of unsteadiness at low frequency has been also measured in plane 32, as shown in Figure 1.12d. In this case, the disturbances are still maximum at the blade tip but with a high level of unsteadiness over the entire span. By comparing the two

signals the authors found a quite high level of coherence meaning that they are probably generated by the same phenomenon.

To summarize, in line with the previous studies, the maximum amplitude disturbances was reached in the tip section near the casing in the operating conditions characterized by the highest pressure rise across the blade tip. According to the authors, the rotating instability arose by the tip leakage jet, however, subsequent studies demonstrated that [89] the onset of the phenomenon is not directly linked to the tip leakage jet.

Concerning the parallelism between the RI in the steam turbine and the one in the compressor, despite some similarities, there are some differences: the rotating stall starts to a specific flow rate near the surge limit while the rotating instability observed in the steam turbine develops very slowly by decreasing the flow rate as reported by Gerschutz et al [88].

Similar measurements were presented by Segawa et al. [90], they investigated a four-stage low pressure model steam turbine under low-load conditions (load between 0-20% of design one). Pressure fluctuations were measured with unsteady pressure transducers installed at inner and outer casing walls and on stationary blades. The results show how the pressure fluctuations became higher in both outer and inner casing by decreasing the volumetric flow in all the stages, except for L3 (first low-pressure stage). A good agreement in reverse flow region prediction between experiment and numerical simulations, presented by Seeno et al. [91], is reported. Considering the 20% load case, both experiment and CFD show pressure oscillation only after the last stage. Since any tip vortex is shown in this operating condition is possible to conclude that such oscillations are generated by the interaction between reverse flow and through flow. By decreasing the fluid volume, pressure fluctuations arose in the former stages. In particular, the dynamic pressure fluctuations become larger just outside the reverse flow region and it is possible to conclude that they are higher on the outer side (at the tip) than on the inner side. According to the authors, this effect could be explained by considering the unsteady oscillation of a vortex, which is generated by

the reverse flow region in the inner region but which affects the forward flow in the outer region.

In the last decades, computational fluid dynamics (CFD) has become crucial for the analysis of the presented phenomenon. However, the transient flow field which characterizes the LSB during low fluid volume conditions is extremely computationally consuming, and some assumptions are crucial in order to reduce the numerical costs, as in the case of the numerical simulations carried out by Herzog et al. [92] based on steady-state assumption, which is one of the first numerical studies on this topic. The comparison with the experiment revealed that RANS simulations were able to catch just the main features of the flow field. Steady-state assumption has been also used by Sigg et al.[93], the comparison with experiments shown a qualitatively good agreement in the pressure ratio across the stages and in the power output prediction. However, the RANS simulation fails to predict the detailed spanwise distribution of the flow field probably due to the coarse mesh and the neglected transient effects. It seems clear that, for in-depth knowledge of the flow field during LVF conditions, the steady-state simulation can offer just a coarse approximation due to the inherent unsteadiness of the flow. For this purpose, unsteady CFD simulations are required. In this regard, Zang et al. [89] carried out unsteady simulations to observe the basic features of the RI in the same low-pressure steam turbine already studied by Sigg et al.[93]. They carried out unsteady 2D whole annulus multi-passage calculations. Although the flow field in this operating condition has a strong radial component, as highlighted by the streamlines in Figure 1.11, a 2D blade-to-blade approach has been used to reduce the computational effort. This is a very strong assumption since it does not allow to consider 3D fluid dynamic phenomena which could be essential for the onset of the RI, however, the RI has been still detected, meaning that 3D phenomena, such as tip clearance jet as proposed by Gerschutz et al. [88], are not the key features to trigger the RI. The frequency spectrum of the pressure signal in a 90% span section shows a region of disturbances in the low-frequency region with evenly spaced peaks, similar to the one found by

Gerschutz et al. and Sigg et al. [88, 93]. Another interesting finding proposed by Zang et al.[89] is the identification of the circumferential nodal pattern of the RI, this has been accomplished by carrying out a circumferential spatial Fourier analysis at several time instants identifying a 16 cells flow structure.

To summarize, the main finding of this work is the demonstration that the non-synchronous rotating instability can be found also with a 2D simulation, meaning that 3D phenomena, such as tip clearance vortex, are not the key features to trigger the RI. The same authors have extended their investigation with a subsequent study [94] aimed to perform a 3D unsteady simulation with the LP pressure turbine and the exhaust diffuser. The main objective of the work is to understand the role of the exhaust system on the formation of rotating instability since this component has a strong effect on the last stage. Due to the findings of their previous investigation [89] tip clearance jet is not modeled. Since a whole annulus 3D calculation would be extremely time-consuming, a reduced domain with an approximate blade counts ratio is considered. As a first finding, the authors show how the large-scale hub cone separation of the diffuser is not linked to the onset of the RI since this separation is also present in an operating condition outside the instability range. They suggest that a more likely key for the onset of the instability might be the compressor mode operation of the blade tip, as already pointed out by other works [88, 92, 93]. By comparing the 2D e 3D results in the tip section, the authors pointed out that the 2D simulation leads to an underestimation of the flow separation in the rotor passage and consequently it generates an instability signal much stronger than in the 3D case. The 3D effect seems to stabilize the flow, however, such 3D results are obtained with a periodic assumption that may affect the accuracy of the numerical results.

In light of the already mentioned studies, the vibration of the rotor blade seems to be connected with pressure fluctuations in the tip region of the axial gap between the last stator and rotor blades. In this regard, N. Shibukawa et al. [95] have carried out a series of experiments aimed at investigating the link between the pressure field and the vibration stresses.

The test rig studied is a model 10 MW steam turbine with a typical last stage of a large size nuclear power plant. The experimental results identified a peak of stresses when the axial velocity goes down between 30-25 % respect to the design in the operating point with maximum pressure rise across the LSB tip, in line with previous investigations [88]. However, this does not seem a sufficient condition but just a necessary one, indeed, another operating point, characterized by a similar pressure rise across the last stage blade tip, presents a low level of vibrations. The unsteady pressure signals have been post-processed with FFT and the results show that the pressure fluctuation can excite the blades, and its frequency depends on the steam condition. The operating point characterized by maximum vibration stress coincides with the one with the highest pressure oscillations.

In a subsequent investigation reported by N. Shibukawa et al. [96] the measurements were instead realized on a six-stage full-scale steam turbine, the experimental setup is shown in Figure 1.13a. As illustrated in Figure 1.13b, two different approaches have been used to investigate the LVF conditions: Test A has been realized by maintaining a constant condenser pressure and therefore varying the mass flow while Test B on the opposite so by keeping the mass flow constant. Test A presents gradually increasing stresses up to reach a peak of stresses around 40 m/s of L0 outlet axial velocity, further reduction of axial velocity leads to a decrease of the stresses. A different trend is instead obtained in Test B where the stresses gradually increase with a rise of the condenser pressure. It is worth noticing how the difference between the stresses in Test B and Test A is almost equal to the density ratio, this highlights the key role of the density in determining the blade vibration stresses. Although the effect of the density ratio the Test A presents an abrupt increase of the blade stresses, even higher respect to the Test B maximum, which is necessarily linked to unsteady fluid force excitations.

The link between blade vibration and fluid dynamic pressure fluctuations is reported in Figure 1.13c, as can be seen, the stator exit tip pressure fluctuations are the only good indicator for blade vibrations

while the others flail to predict the blade vibration trend. This is the demonstration that the source of the blade vibration should be sought in the area where the RI has been found by other studies. Concerning the hub measurements, a much different behavior between pressure fluctuations and blade vibration is reported meaning that the flow unsteadiness in the separation area behind the blade has less potential to trigger blade vibration probably due to the high stiffness in such region.

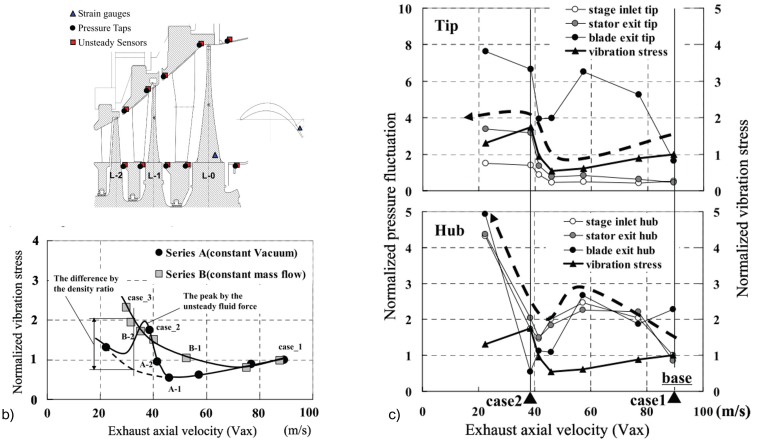

Figure 1.13: a) Experimental setup b)measured vibrations stress against axial velocity at L0 outlet c) Pressure Fluctuations (and vibration stresses) against axial velocity at L0 outlet
Figure adapted by [96]

In Figure 1.14 the frequency spectra of the pressure signals at the last stage stator and rotor outlets are reported. Concerning the stator exit tip, both the operating points showed a high level of unsteadiness probably due to the presence of the RI while at the stator hub strong disturbances are revealed for Case 3 which are not due to the RI since it is usually located near the tip. The source of such unsteadiness seems instead located at the rotor exit hub where huge pressure oscillations are measured (Figure 1.14b), such oscillations may be linked to the hub separation vortex presented in Figure 1.5.

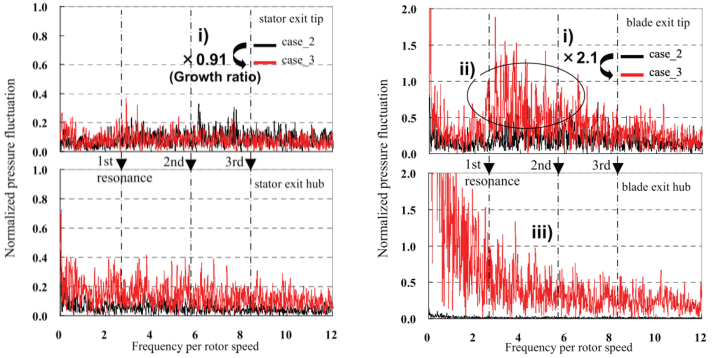

Figure 1.14: a) Frequency spectra at last stage stator blade exit b) Frequency spectra at last stage rotor blade exit
Figure adapted by [96]

Once demonstrated the existence and the dangerousness of the flow-induced vibration under LVF conditions, several FSI approaches arose in literature to numerically evaluate the impact of such vibration on the structural integrity of the LSB. A fully coupled FSI is not required due to the already mentioned purely aerodynamic nature of the rotating instability phenomenon and the focus of the analysis is one-way: from fluid to solid. In this regard, Tanuma et al. [97] have extended the results obtained by N. Shibukawa et al. [95] by carrying out 3D unsteady simulations at LVF conditions, however, they considered just a two nozzle and three-blade spacing domain to save computational time respect to a full arc simulation. Despite the fluid domain simplification, they numerically demonstrated that a rotating instability exists. The unsteady pressure field computed with the URANS simulation has been used to generate unsteady load for a one-way FSI analysis. However, the authors reported that a full arc unsteady simulation would be necessary to predict with accuracy the vibration stress by taking into account any asymmetries induced by fluid dynamic effect or by the radial exhaust hood. In this

regard, a methodology to predict to consider blade vibration during LFV in the design phase is presented by Tanuma et al. [98]. The procedure is based on boundary conditions taken from measured data in real steam turbines, full 3D CFD and unsteady structural analysis with a six-blade group. The results of the analysis are in line with ones already reported in the literature: the source of blade vibration seems the tip torus vortex.

Another FSI approach has been proposed by Zhou et al. [99], it is based on transient CFD and structural modal analysis. The one-way coupling FSI analysis used is the sequentially coupled forced response approach, proposed by Moffat and Ning [100, 101], in which the aerodynamic load is calculated stand-alone without the input of blade vibration and is only subsequently coupled with a structural model to predict blade response. The transient history of the blade integral pressure is converted into the frequency domain and compared with vibratory modes. After this screening phase, the 3D pressure distribution at the frequency of interest can be extracted and interpolated over the blade surface to derive a modal force. Finally, a single degree of freedom (SDoF) analysis is performed with damping coefficients obtained from test data. In this work two operating points have been investigated: TP-C6 and TP-A2, both present an axial velocity at the diffuser outlet of almost 61 m/s with a different exhaust pressure, TP-C6 has a higher exhaust pressure roughly 3 times respect TP-A2. Despite the density ratio existing between the two operating points, it is worth highlighting how the experimental data presented by Zhou et al. [99] in Figure 1.15a shows a peak of frequency response, in correspondence of the 1^{st} axial mode, for the TP-A2 strongly higher respect to the response of the other operating point. The explanation of this effect can be understood by looking at Figure 1.15b where the frequency spectrum of the integral blade pressure is reported. This spectrum shows clear peaks corresponding to nozzle passing frequency (NPF), tip vortex frequency and low engine order frequency (LEOF) generated by the separation area downstream of the last stage rotor blade since only the lower half of the bucket is exposed to LEO excitations, where flow separation and circulation exist. According to the authors,

the low engine order instabilities are responsible for the first axial mode excitation.

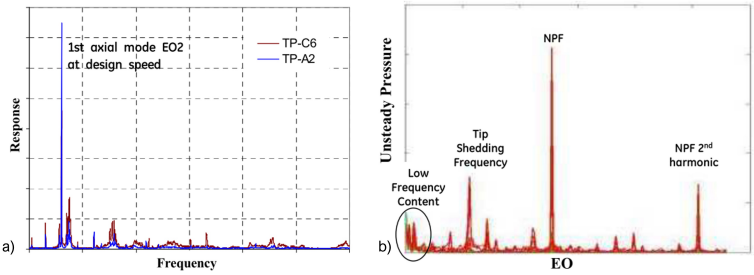

Figure 1.15: a) Blade response in frequency spectra b) Frequency spectra of unsteady blade pressure for TP-A2
Figure adapted by [99]

The presented FSI approaches are based on harmonic or multi-blade analysis, however, Qi et al.[102] highlight how only the full annulus can predict an asymmetric stress oscillation caused by uneven frictional damping generated by the presence of shrouds and snubbers. Qi et al.[102] presented an aerodynamic and structural coupled method based on full annulus FEM calculation. The fluid domain includes the full annulus of the last stage with shrouds and snubbers coupled with a radial exhaust hood. It is worth noting how, contrary to what was found by Gerschütz and Shibukawa [88, 95], the condition of maximum stress is not the same one with the maximum pressure rise in the blade tip. According to the authors, this may be due to the effect of the shrouds.

The CFD investigations presented up to this point, except for [98, 102], which are recent work, are characterized by strong assumptions in the numerical setup: the most limiting seem to be the steady-state and the fluid domain simplifications, such as 2D or periodic 3D. The first attempt to simulate the full 3D annulus of the last stage coupled with a simplified exhaust hood has been presented by Megerle et al.[78]. The unsteady CFD simulations have been carried with the commercial code CFX by using the turbulence model standard k-ε with the automatic wall treatment to limit

the number of near-wall computational nodes. Both the experiment and numerical model are with air, but the existence of the rotating stall cells is demonstrated, meaning that such phenomenon is not linked to the fluid type. Two different exhausts are tested in order to evaluate the effect of different boundary conditions on the investigated phenomenon, one with a convergent outlet extrusion, with a standard outlet, to avoid recirculation at fluid domain boundary and another with an opening boundary type, which allows reverse flow at the outlet. The outlet boundary affects the number of tip stall cells, which is an expected trend since it is stochastic, while rotational speed is very similar meaning that this phenomenon is not so sensitive to the outlet type. Also the effect of the tip clearance is evaluated, and, in contrast with the results presented by Gerschutz et al. [88], the number of cells and their rotational speed seem to be insensitive to such flow feature. Concerning the comparison with experiments, the author reported differences in the fractional speed of the stall cells.

The effect of the exhaust hood on the unsteady fluid behavior has been also experimentally assessed by Sigg et al. [103]. The same LSB were tested with different exhaust shapes, obtained by varying the back wall distance, of the model air turbine already investigated by Megerle et al [78]. The results show how the rotating instabilities can be influenced by the exhaust shape. Indeed, for a fixed operating point (fixed flow coefficient), the amplitude of the RI is strongly affected by the back wall, specifically, it ranges from zero to the maximum value by increasing the back wall distance (increasing B, the ratio between diffuser length and blade span). This monotonically increasing trend is interrupted when a peak of amplitude is reached, beyond this value it seems insensitive to the back wall distance. It is also worth highlighting how the exhaust hood affects the value of the flow coefficient by which RIs are detected. According to the authors, a possible explanation behind this trend is the dimension of the diffuser hub separation area, which is influenced by the exhaust volume. Different behavior of the recirculation zone may indeed impact the flow impulse, density and turbulence leading to different behaviors of the RI mechanisms.

In a further investigation Megerle et al. [104] studied a model steam turbine with a 7 m^2 exhaust area. As in the previous work the full annulus of the last stage is considered coupled with a 3D radial exhaust hood. The steam is considered an ideal gas since the measurements show that under LFV conditions it is far above the saturation line. The results obtained with such an exhaust hood are compared with the ones calculated with symmetric exhaust hood, similar to the one shown in [78], such comparison shows how the amplitude of the pressure fluctuations is an order of magnitude higher in the realistic exhaust case while the frequency of the peak is almost the same. These results demonstrated again that a real exhaust configuration is necessary to capture the amplitude of the pressure fluctuations, while the triggering of the rotating instability seems to be not affected by the exhaust type. Despite the differences existing in the geometry and in the material respect to the previous work [78], the tip RI is found for a similar value of the flow coefficient, between 0.04 and 0.15. It can be concluded that the flow coefficient is a key parameter to investigate this phenomenon. Finally,a discrepancy in the fractional speed numerical prediction respect to the experiments is reported also for the steam model turbine.

Concerning the parallelism between this phenomenon and the compressor rotating stall, the authors highlight some similarities, in particular with the part-span stall. The first one is the propagation speed that in compressor stall is usually counter rotating respect to the rotor and with fractional speed values ranging from 50 and 80%, this mechanism is similar respect to the RI phenomenon observed in steam turbine LSB. Another similarity is on the trigger mechanism, which is linked to a suction side separation in compressor leading to the blockage of the passage; Consequently, the flow is deflected towards the adjacent passage with high incidence and this causes the stall of also this passage. With a similar mechanism also the RI onset may be linked to a suction side separation.

In the light of the above investigations, the prediction of the RI propagation velocity is an extremely challenging task for the CFD modeling. In this regard, Megerle et al. [105] carried out an enhanced numerical

simulation by using a scale-resolving turbulence modeling: Scale Adaptive Simulation (SAS), which is able to simulate large-scale turbulent fluctuations in an extremely pragmatic way since it demands less mesh density requirements respect to a Large Eddy Simulation (LES) or other hybrid approaches. The comparison between URANS, SAS and experiments show small differences between the numerical models in the flow field resolution and both fail to predict the axial velocity near the casing, probably due to the coarse mesh used.

Significant differences between the numerical models are instead reported by considering the STFT (Short Time Fourier Transform) of a static pressure time history in a monitor point located between stator and rotor at 87% span, where SAS shows a higher level of unsteadiness over the entire range of frequencies. The URANS predict only two major sources of unsteadiness, one, at high frequency, is the effect of the stator wake and the other, at low frequency, is the effect of the RI. The SAS model is able to predict a two-band behavior of the rotating instability at low frequency, which means that two RI patterns are present simultaneously. In particular, a stronger 7 stall cell pattern at 3.2 EO (ratio between frequency and rotational frequency) and a 13-14 weaker one at 7-6 EO. In the experimental results, a strong instability between 3.5 and 4 EO is clearly visible and, consequently, the low stall cell pattern is confirmed, while the high stall cell is hardly observable. It is worth highlighting the huge disparities between the experimental and CFD conditions, in particular in the experiments several rotor revolutions con be measured rapidly in contrast with the CFD where each rotor revolution is extremely time-consuming and the physical time simulated is inevitably lower. On the other hand, the time step used for the CFD is significantly lower respect to the time of acquisition of measuring instruments this means that the CFD can predict physical phenomena at higher frequency respect to experiments.

Concerning the velocity of propagation of the stall cells, the SAS model presents a good agreement with the experimental results. Both the experiment and simulation show a reduction of the propagation speed

with an increase in the volume flow and it can be concluded that the fractional speed of propagation is linked to the flow coefficient.

Further developments in the numerical modeling of the LVF conditions are proposed by Ercan and Vogt [106] by carrying out improved Delayed Detached Eddy Simulations (iDDES). In this work, a comparison between URANS, iDDES and experiments in different operating conditions is presented, characterized by 6,3%, 12% and 18% of the design mass flow, with a fixed outlet pressure of 23.5 kPa. The fluid domain consists of 3 stages with a full annulus extension and a radial exhaust hood. The tip gap is included in the fluid domain and the steam is considered an ideal gas. Both the experimental measurements and numerical simulation monitor points are focused on the axial gap between the last stage stator and rotor where previous investigations [78, 88, 104, 105] have shown the RI. A comparison between the FFT spectra of the pressure signal in this area is reported for different operating conditions. In the 18% design mass flow, the experiments show a high amplitude region between 0-2 EO and another between 7-10, while both the CFD models predict only the high-frequency region. At the 12% design mass flow, both the numerical models predict the region of instability between 0-2 EO in agreement with experiments, while a higher frequency region of instability, observable in the experiments, is well predicted only by the iDDES. A similar trend is shown in the 6.3% design mass flow case. To summarize, both the CFD models agree quite well with experiments for the lower mass flow cases while they fail to predict the lower frequencies at 18% mass flow. The improvements achieved with the iDDES are linked to the tendency to show more RI configurations due to the instabilities of the flow field generated by the turbulence effects. Concerning the prediction of the propagation velocity of the stall cells, a very good agreement between numerical models and experiments is shown for the 6.3% design mass flow while in other operating conditions the agreement is slightly worse.

Most of the works presented up to this point were focused on pressure monitor points located in the axial gap between the last stage stator and rotor, which has proved to be a valid strategy for the identification of the

RI. A different approach has been instead proposed by Liu et al. [107] and Rzadkowski [108], both these investigations are focused on the unsteady blade forces using a full 3D numerical model of the last stage coupled with the exhaust hood. The results show how also this strategy can be used to detect the flow instabilities caused by unsteady phenomena such as stator wakes, last stage-diffuser interaction and the RIs at the LSB tip.

To the author's knowledge, in literature, there is a lack of investigations concerning axial exhaust systems during LVF conditions. Recently Hoznedl et al.[109] presented experimental results of flow in the LSB of a steam turbine with an axial diffuser, the experimental setup presented in Figure 1.16 consists of pressure tap and temperature measurement at the hub and tip of the blades. In addition, the blade vibrations are measured with the blade tip-timing.

Temperature and pressure measurements highlight how the steam at L1 inlet is superheated during LVF conditions. They also demonstrated how a flow coefficient of 0.17 is the transition point for the ventilation of the last stage. In Figure 1.16b the blade vibration as a function of flow coefficient is reported, it is worth highlighting how the blade vibration experiences a significant increase in correspondence of a flow coefficient of 0.27 where the hub separation appears in the diffuser. Such vibration may be triggered by the flow unsteadiness in the hub separation vortex. The blade vibration increase continuously by decreasing the flow coefficient in the region of ventilation (pressure ratio at the tip higher than 1) up to reach a maximum in correspondence of a flow coefficient of 0.05, with the maximum pressure rise across the blade tip. Further decrease of the flow coefficient beyond this value leads to a decrease of blade vibration.

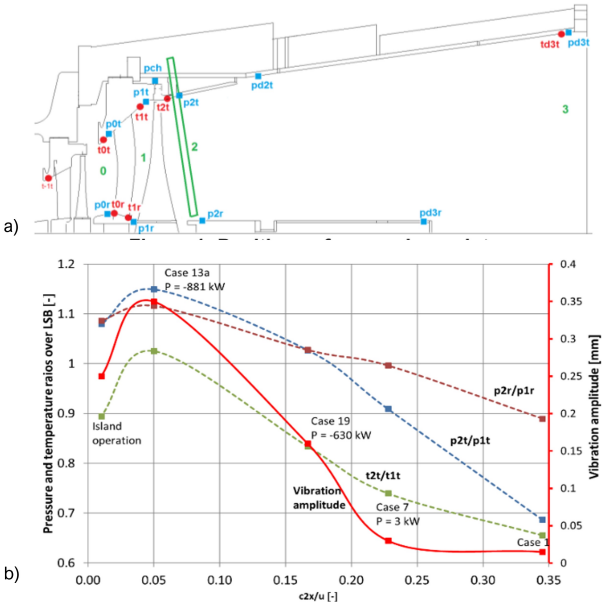

Figure 1.16: a) Experimental Setup b) LSB vibration and temperature/pressure ratio against flow coefficient
Figure adapted by [109]

1.5 Post-Processing Techniques

In this section, the theory behind the modal analysis techniques used in Chapter 4 is presented. Starting from a description of the classical Discrete Fourier Transform (DFT) analysis up to the advanced data-driven technique Proper Orthogonal Decomposition (POD). The latter is a useful tool to extract as much information as possible from large amounts of data, specifically, it enables the identification of coherent structures within a turbulent flow, which are often embedded, favoring the understanding of how they interact and how they contribute to the development of a specific phenomenon.

The DFT analysis is used to decompose a signal, the evolution in time of a specific quantity, into a sum or an integral of harmonic functions.

In this work, to be clear, the Fast Fourier Transform has been used, which is an algorithm that computes the discrete Fourier transform (DFT) allowing significant speed-up respect to the classical DFT [110]. Although this, it is fundamental starting to describe the DFT, which is given by:

$$\hat{f}_k = \sum_{j=0}^{n-1} f_j e^{-i2\pi jk/n} \tag{1.12}$$

Where j identifies the time domain, n identifies the frequency domain. It is worth mentioning how the DFT is not a data-driven technique (such as POD) since its temporal basis is defined a priori and it depends on the number of time steps and sampling frequency.

The DFT is therefore a linear operator that maps the data points from f (i.e. time domain) to the frequency domain $\hat{f}$. For a specific number of points n, the DFT allows representing the data using the sine and cosine functions with an integer multiple of a fundamental frequency. Considering:

$$\omega_n = e^{-2\pi i/n} \tag{1.13}$$

The DFT may be calculated with a matrix multiplication:

$$\begin{bmatrix} \hat{f}_1 \\ \hat{f}_2 \\ \hat{f}_3 \\ \vdots \\ \hat{f}_n \end{bmatrix} = \begin{bmatrix} 1 & 1 & 1 & \cdots & 1 \\ 1 & \omega_n & \omega_n^2 & \cdots & \omega_n^{n-1} \\ 1 & \omega_n^2 & \omega_n^4 & \cdots & \omega_n^{2(n-1)} \\ \vdots & \vdots & \vdots & \ddots & \vdots \\ 1 & \omega_n^{n-1} & \omega_n^{2(n-1)} & \cdots & \omega_n^{(n-1)^2} \end{bmatrix} \begin{bmatrix} f_1 \\ f_2 \\ f_3 \\ \vdots \\ f_n \end{bmatrix} \tag{1.14}$$

The output vector $\hat{f}$ contains the Fourier coefficients for the input vector f. It is worth highlighting how the matrix F is complex-valued, consequently, the output $\hat{f}$ has both a magnitude and a phase.

The calculation of DFT implies O (n^2) operations, while, as mentioned earlier, the FFT rapidly computes such transformations by scaling as O(nlog(n)) allowing a significant speed-up.

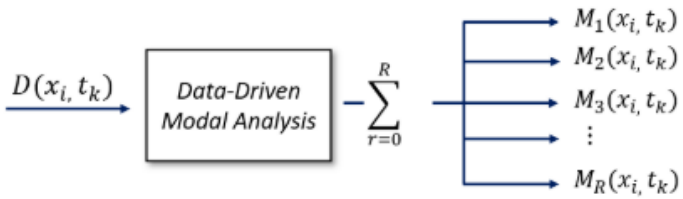

Figure 1.17: a) Schematic representation of DDMA
Figure adapted by [111]

In this work the results of the FFT are presented by computing the amplitude of the oscillations, the amplitude is calculated as the ratio between the magnitude and the number of points in the time-domain signal (N):

$$\text{Amplitude} = \frac{\text{Magnitude}}{N} \tag{1.15}$$

Although the Fourier Transform provides information about the frequency content of a signal, it does not provide any information about the evolution in time of that signal. For signals non-stationary time, like the ones presented in this work, it is essential to characterize both the frequency content and its evolution in time. In this regard, the Short Time Fourier Transform (STFT) computes a windowed FFT in a moving window allowing the characterization of the frequency content in time, the so-called spectrogram.

Before directly describing the POD, it is worth introducing the idea behind the Data-driven modal analysis (DDMA) which is a branch of the data analysis aimed at decomposing a set of data into a series of modes, as schematically shown in Figure 1.17.

The starting data set can be obtained by recording the evolution of a specific quantity in time and space, the DDMA decomposes this set into a linear combination of several modes. The modes may evolve in non-linear way but their combination is still linear. Each mode M_j presents a spatial structure (x_i) and a temporal structure (t_k). The DDMA can be used for

multiple purposes:

- pattern recognition: The mode spatial distributions can provide information about coherent structures usually embedded in turbulent flow, this application of DDMA is used for the post-processing of experiments (e.g. PIV) and CFD simulations, as in the case of the present work.
- data compression/filtering: The identification of low-importance modes, which may be related to background noise, can help to remove useless information in the data set acting as a filter. In the fluid dynamic context, this can be useful for removing background noise from PIV images or CFD analyzes
- model order reduction (Reduce Order Model ROM): This application of DDMA can be used to reduce the complexity of a problem by projecting the problem into the basis generated by a few high-importance modes significantly reduce the computational costs.

The first step for the application of the DDMA is to build the data matrix D (snapshot matrix), which is the matrix to decompose. It can be expressed as follow:

$$\begin{bmatrix} d_1[[1] & \cdots & d_k[1] & \cdots & d_{n_t}[1] \\ \vdots & \vdots & \vdots & \vdots & \vdots \\ & \vdots & \vdots & \vdots & \vdots \\ d_1\,[n_s] & \cdots & d_k\,[n_s] & \cdots & d_{n_t}\,[n_s] \end{bmatrix} \tag{1.16}$$

This matrix is composed by recording the evolution of one or more variables in space and time and placing a snapshot of the system in each column. So, the rows represent the time evolution while the space distribution is presented along with the columns. Ns is the total number of points in the space, the computational grid nodes for the CFD, and nt is the number of snapshots considered.

This matrix can be viewed from two different perspective, the space view:

$$D[\mathbf{i}, k] = \sum_{r=1}^{R} c_r[k]\phi_r[\mathbf{i}] = \sum_{r=1}^{R} \sigma_r \psi_r[k]\phi_r[\mathbf{i}] \tag{1.17}$$

And the time view:

$$D[\mathrm{i}, k] = \sum_{r=1}^{R} c_r[\mathrm{i}]\psi_r[k] = \sum_{r=1}^{R} \sigma_r \phi_r[\mathrm{i}]\psi_r[k] \tag{1.18}$$

Where:

- σ_r are the eigenvalues of the data correlation matrix (explained later), they identify the energy content of each mode and consequently the weight in reproducing the starting data set D

- ψ_r are the eigenvectors of the correlation matrix, they characterize the time evolution of each mode. By performing an FFT of these terms is possible to identify the frequency content of each mode.

- ϕ_r represent the spatial distribution of each mode allowing to identify of the coherent structures in the starting data set

In the spatial view (row variation), each snapshot can be seen as a linear combination between of spatial bases ϕ_r and the coefficients of this linear combination change in time c_r (controlled by the set of ψ_r). On the other hand, the temporal view (column variation) can be obtained as a linear combination of temporal bases ψ_r and the coefficients of this linear combination change as we consider different spatial locations (controlled by the set of ϕ_r). However, spatial and temporal basis are linked and so it is coupled a problem. It is worth considering how is suitable to consider both the basis of unitary length ($\|\phi_r\| = \|\psi_r\| = 1$) so the σ_r directly represents the contribution, or amplitude, of each mode. In the light of the above, it is convenient to write the linear combination as the sum of outer products:

$$D = \sum^{R=\mathrm{rank}(D)} \sigma_r \phi_r \psi_r^T \tag{1.19}$$

Each outer product together with its amplitude σ_r represents a rank-1 approximation of the data D, so the sum of all the possible rank-1 contributions is possible to reconstruct the original set of data D. It is interesting highlighting how if the number of modes considered is equal to the rank of the original matrix, no approximation is done. Otherwise, if the number of modes is less than the rank of D (as usually done in practical applications) the reconstructed matrix is an approximation of the starting one.

By writing the equation 1.20 in a more compact way, the following matrix expression is obtained:

$$D = \Phi \sum \Psi^T \tag{1.20}$$

where:

$$\Phi = \begin{bmatrix} \phi_1[\mathbf{i}] & \phi_2[\mathbf{i}] & \dots & \phi_R^{\dot{L}}[\mathbf{i}] \\ \vdots & \vdots & \vdots & \vdots \end{bmatrix} \tag{1.21}$$

$$\Sigma = \begin{bmatrix} \sigma_1 & 0 & 0 \\ 0 & \ddots & 0 \\ 0 & 0 & \sigma_R \end{bmatrix} \tag{1.22}$$

$$\Psi = \begin{bmatrix} \psi_1[k] & \psi_2[k] & \dots & \psi_R[k] \\ \vdots & \vdots & \vdots & \vdots \end{bmatrix} \tag{1.23}$$

Since Σ is diagonal and the columns of ϕ and ψ are normalized is not possible to choose simultaneously ϕ and ψ. Indeed, usually, ψ is fixed and ϕ is calculated. In addition, if, as already mentioned, the number of modes (R) is less than the rank of D a reduced model is obtained and expressed as follow:

$$\tilde{D} = \tilde{\Phi}\tilde{\Sigma}\tilde{\Psi}^T \tag{1.24}$$

The decomposition approaches differ on how Ψ is obtained. Usually, the matrix ψ is orthogonal and consequently, the following expression is

true:

$$D\left(\Psi^T\right)^{-1} = \Phi\Sigma = C \tag{1.25}$$

By considering also that each spatial basis element has unitary length, it is possible to calculate σ by normalizing each of the columns of the product $\Phi\Sigma = C$, as expressed by the following equation:

$$\sigma_r = \|C_r\| = \|\phi_r\sigma_r\| \tag{1.26}$$

Once calculated all the σ, it is possible to assemble the inverse of the matrix Σ and therefore calculating Φ with the following equation:

$$\Phi = D\left(\Psi^T\right)^{-1}\Sigma^{-1} \tag{1.27}$$

As mentioned earlier, the way in which the data Ψ is computed determines the difference between the different DDMA techniques, the decomposition can indeed be classified in two main categories: energy or frequency-based, the latter is not discussed in this work.

The POD is the fundamental energy-based decomposition technique, and it is a data-driven technique since its basis is tailored to the data set. The POD is aimed at determining the best approximation of a data set for a given rank. By recalling the equation 1.20, a rank R approximation of the data set can be written as follow:

$$D = \Phi\Sigma\Psi^T \longrightarrow \Phi = D\Psi\Sigma^{-1} \longrightarrow D = D\Psi\Psi^T \longrightarrow \tilde{D} = D\tilde{\Psi}\tilde{\Psi}^T \tag{1.28}$$

with $\Psi \in \mathbb{R}^{n_t \times n_t}$and $\tilde{\Psi} \in \mathbb{R}^{R \times n_t}$, by considering the equation $D = D\Psi\Psi^T$, it is clear how if Ψ is a complete orthonormal basis then the equation becomes D=D, however if an approximation is introduced by considering only R columns of Ψ ($\tilde{\Psi}$) then $\tilde{\Psi}\tilde{\Psi}^T$ is no more the identity but it is a projection matrix which leads to the definition of an approximated data set $\tilde{D}$. In the specific case of POD, the temporal basis computed is the optimal one that minimizes the approximation error. The decomposition

problem is therefore traced to an optimization problem that can be solved in two different ways, for the first mode this problem can be solved with error minimization:

$$\min\left(||D-\widetilde{D}||_2\right)=\left(||D-D\widetilde{\Psi}_1\widetilde{\Psi}_1^T||_2\right) \tag{1.29}$$

or with energy maximization:

$$\max\left(\sigma_1\right)=\max\left(||\Phi_1\sigma_1||_2\right)=\max\left(||D\tilde{\Psi}_1||_2\right) \tag{1.30}$$

the constrain of the procedure is

$$\langle\psi,\psi\rangle=\psi^T\psi=1 \tag{1.31}$$

By using the energy maximization approach, it is possible to solve it with the Lagrange multipliers method. First of all, it is necessary to define an auxiliary function $\mathcal{A}$, defined as follow:

$$\mathcal{A}=\left\{(D\psi)^\dagger(D\psi)\right\}+\lambda\left\{1-\psi^\dagger\psi\right\} \tag{1.32}$$

Where the first term is the maximization object while the second is the constraint, λ is the Lagrange multiplier. In order to solve the optimization problem is necessary to derive the auxiliary function respect to the independent variable:

$$\frac{\partial\mathcal{A}}{\partial\psi}=\left(D^\dagger D\right)\psi-\lambda\psi=0 \tag{1.33}$$

The equation 1.33 is true when:

$$\left(D^\dagger D\right)\psi=\lambda\psi \tag{1.34}$$

The equation is an eigenvalue problem, since the best basis to make a rank-1 approximation is must be the eigenvector of the temporal correlation matrix K, defined as $K=D^\dagger D$. So, the eigenvalue problem involves determining the eigenvalues λ and the associated eigenvectors starting from the expression indicated above. It is worth mentioning how the

same procedure can be repeated by firstly computing the spatial basis Φ, depending on this choice different POD methods can be implemented.

In this regard, POD was first applied to the fluid dynamic context by Lumley [112] in a space-only form (spatial POD) and it was focused only on the calculation of the modes spatial distribution, neglecting their temporal evolution. The link between spatial and temporal evolution of modes was found by Sirovinch [113, 114] with the so-called Snapshot POD, which is the one used in this work since such method is suggested when the spatial points are greater than the temporal ones, as often happens in CFD simulations. The algorithm to calculate the Spanshot POD has been implemented in Matlab by following these steps:

- Prepare K: $K = \left(D^T D\right)$
- Diagonalize K: $\mathrm{K} = \Psi_P \Lambda_P \Psi_P^T$
- Compute spatial POD modes and modes amplitude coefficients:
  $\Sigma_P = \sqrt{\Lambda_P}\Phi_P$
  $\Phi_P = D\Psi_p\Sigma_P^{-1}$

In the last years, POD analysis is more and more frequently used in different applications even outside the fluid dynamic context. For a detailed description of this method applied to fluid dynamic problems, it is worth mentioning the work presented by Berkooz et al. [115]. However, since this work is focused on the low-pressure turbine, for a sake of brevity, only the applications of such a technique in a similar scenario are presented. At this regard, S. Sarkar [116] performed a POD analysis of fluctuating flow field obtained from a LES simulation on a low-pressure turbine cascade showing that it is able to identify the dynamics related to the passing wake events. D. Lengani et al. used POD to investigate loss generation mechanisms in a low-pressure turbine (LPT) cascade [117, 118, 119, 120, 121]. In this works, POD is used to identify coherent structure in complex flow field allowing the assessment of their impact in the loss generation. The link between Reynolds stresses and dissipation mechanisms is also evaluated. In [121] they apply POD to high-fidelity

LES simulation to quantify the entropy generated by each of the different dynamical features which characterize the blade passage. It seems clear how the POD can help to the most important modes in a chaotic flow field, ranking them on the basis of their energy content, however, sometimes the physical interpretation of each mode may be complex since, as shown by Mendez et al. [122], it may happen that coherent phenomena are mixed over different modes.

To the best of the author's knowledge, this is work presents the first application of this technique for the study of transient instabilities in the exhaust system during LVF conditions. This can further enhance the understanding of this phenomenon by decomposing the different sources of instabilities. In addition, the post-processing techniques presented in the literature review are based on the analysis of a local signal (obtained with probes or monitor points), the results are so strongly dependent on the position of the monitor points. This can lead to a loss of essential information, which may be instead avoided by using techniques (such as POD) based on 2D or even 3D sets of data.

Chapter 2

Exhaust System Numerical Modelling

This chapter is focused on the application of different numerical models, already introduced in the previous chapter, to compute the flow field within an exhaust hood. The main differences between the investigated approaches concern the stator-rotor and rotor-exhaust hood interfaces modeling. In line with the findings proposed by the literature review both steady, i.e mixing plane and frozen rotor, and unsteady solutions are tested. A numerical grid sensitivity approach is presented, which has been systematically used for the results presented in this work. In other words, this chapter aims to present and justify the numerical choices behind the optimization method proposed in the following chapters, in chapter 3.

This chapter is split into two different sections, in the first one the influence of different numerical setups on the flow field of a radial exhaust hood, manufactured by Baker Hughes, is assessed while in the second the focus is moved to an axial exhaust hood, still manufactured by Baker Hughes, where similar setups are tested. The parallelism between the different geometries allowing to understand the huge differences in the aerodynamic flow field and the different impacts of the interface used on the performance. It is worth highlighting how all the results presented

in this section are obtained with design operating conditions, while the off-design assessment is presented thereafter (in chapter 4).

2.1 Radial Exhaust Hood

In this section a numerical investigation on the flow-field and aerodynamic performance of a low- pressure steam turbine exhaust hood through CFD simulations is presented, it aims at comparing results coming from a full mixing plane approach (FMP) with those resulting by the frozen rotor approach (FFR), that is considered as the reference simulation in the industrial practice. The results described in this section are also reported in [123].

The geometry under investigation consists of a turbine stage and an exhaust system, as shown in Figure 2.1a. In the full mixing plane approach, all computational domain interfaces are treated with a mixing plane model, namely between the stator and rotor domains, as well as between the latter one and the exhaust hood. As a result, only a single rotor blade has to be modeled (2.1b) on the contrary respect to FFR setup in which the full annulus mesh of the rotor is included (2.1c). Both the approaches consider a single passage of the stator domain whose downstream interface is linked to the rotor domain through the mixing plane approach, this is a typical approach found in the industrial design practice since the stator domain of the last stage is usually chocked and only weak variations of the flow in the circumferential direction are present. The rotor tip leakage jet and the exhaust hood struts are included in the simulation due to their high importance in the numerical accuracy in the light of the literature review presented in chapter 1.

The blade rows were meshed using ANSYS Turbogrid, therefore structured grids were realized then converted into unstructured meshes. The parameters used for the grids generation are decided from the author's experience, allowing the generation of sufficiently refined grids, which sizes are summarized in Table 2.1.

The exhaust system was meshed by using ANSYS Meshing, realizing

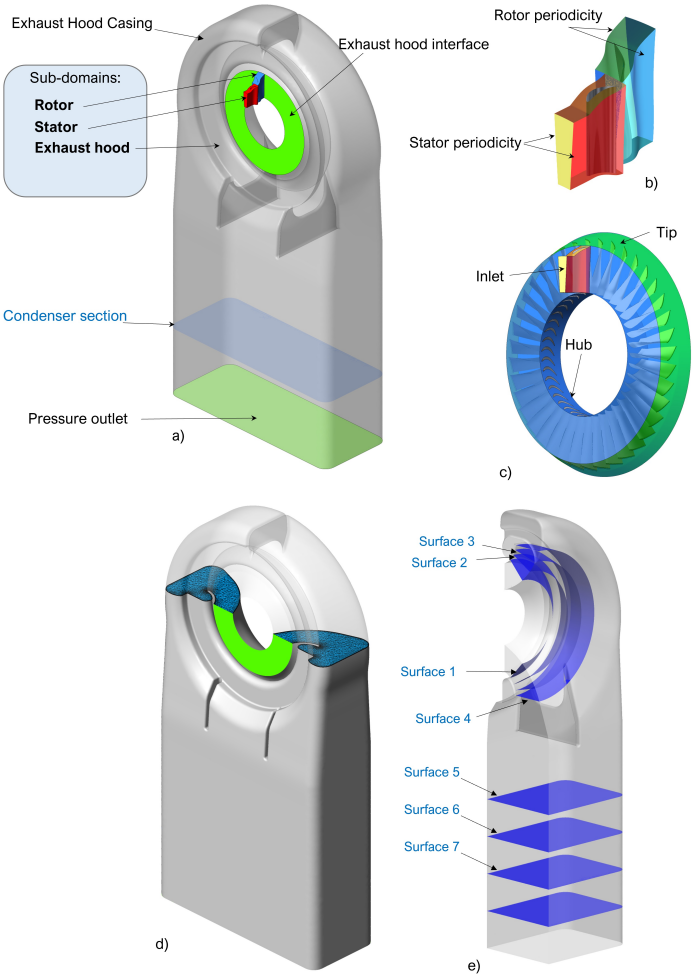

Figure 2.1: a) Illustration of the computational sub-domains , b) stator-rotor domains for FMP model, c) stator-rotor domains for FFR model d) Mid section of exhaust hood e) post-processing surfaces

tetrahedral grids with prismatic layers at near-wall regions in order to well reconstruct the viscous boundary layer, with a y+ value of 2.

Table 2.1: Elements number of stator and rotor grids.

CFD model	Stator elements number	Rotor elements number
FMP	249k	480k
FFR	249k	18.9M

ANSYS CFX v.18 has been used to solve 3D RANS equations, using the coupled solver available in the code. Although the impact of steam wetness is documented in the literature, an ideal gas assumption has been used for a sake of reducing computational costs. Such an approach, widely used in literature, is still valid for qualitative comparisons between different models. In addition, it is worth recalling how such work is preparatory at the development of an industrial optimization procedure, where the speed of the numerical simulation is a key point in order to limit the duration of design time.

By virtue of the findings proposed in the literature review, the turbulence was modeled adopting the SST k-ω model [124] combined with the automatic wall treatment model, which applies a smooth transition between a low Reynolds and standard wall function approach as a function of y+ value. Such turbulence model was developed to offer a better prediction of the separated flow and therefore it is expected to be the most suitable for strongly separated flow as demonstrated by Bardina et al.[47].

The advection fluxes of continuity, momentum and total energy equations are calculated with a high-resolution scheme, essentially a second-order and bounded scheme, while a first-order scheme has been used for the convective terms of turbulence equations since it has a low impact in this application; viscous work term has been included in the energy equation.

Concerning the boundary conditions, by referring to Figure 2.1 for surfaces' names, at the stator inlet were imposed a constant total pressure and total temperature, a normal flow direction and 5% of turbulence intensity, while at the exhaust system outlet a constant static pressure was imposed. As highlighted in Figure 2.1a, the exhaust hood outlet does

not match with the surface representing the condenser inlet (pointed as condenser surface), but it is located downstream; this extrusion of the geometry was performed in order to avoid a back flow phenomenon in the numerical outlet during the computation. All walls were treated as adiabatic, smooth with a no-slip condition, therefore a zero speed was assigned to the stator nozzle and endwalls, to the walls of the exhaust hood and to the rotor blades and hubs, while a counter-rotating speed condition was imposed to the tip surface since the equations in the rotor domain are solved in the rotating frame. Periodic boundary conditions have been applied at the stator domain, as well as in the rotor domain of the FMP model. The simulations were stopped when monitor points and integral quantities had achieved a steady condition, and the scaled residuals had reached a minimum of $1 * 10^{-4}$ for every equation.

2.1.1 Mesh independence study

Before illustrating the results of the different interface models, the computational mesh is presented. It has been selected by virtue of a grid refinement study aimed at assessing the dependency of the numerical results on the mesh grid by applying the grid convergence index (GCI) method proposed by Roache [125]. Such a method is based on the generalized theory of Richardson extrapolation and involves the comparison of discrete solutions at three different grids spacing: h_c (coarse mesh), h_m (mid mesh) and h_f (fine mesh). The representative mesh spacing was computed using the following equation, as proposed by Celik [126], where Vi is the volume of the i-th cell and N is the total number of the grid:

$$h = \left[\frac{1}{N} \sum_{i=1}^{N} \Delta V_i \right]^{1/3} \tag{2.1}$$

The different meshed predictions are compared in terms of static pressure recovery coefficient (C_p), defined in Equation 1.1, which measures the static pressure recovered, at a specific section, from the available total energy at the inlet of diffuser.

Figure 2.2 shows the pressure recovery coefficient trend as a function of grid refinement, evaluated along the flow path on the post-processing surfaces, these are highlighted in Figure 2.1e; the recovery coefficient is normalized by a reference value (Cp) that will be used, from henceforth, in the normalization of every result.

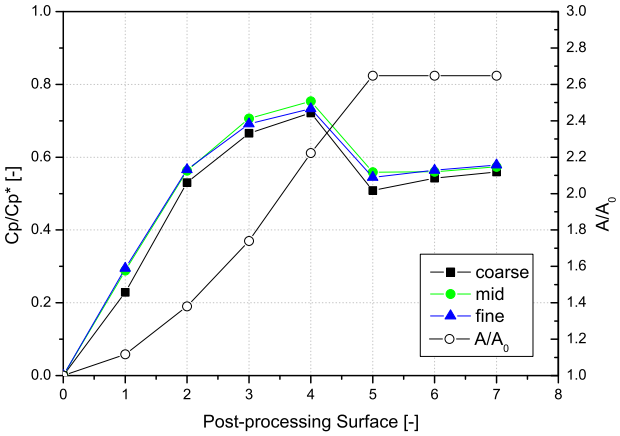

Figure 2.2: Behavior of Cp on post-processing planes as a function of grid refinement

As can be seen from Figure 2.2, the Cp trends resulting from the fine and mid grids as quite overlapping, with the main deviation, less than 3%, located at the diffuser exit (surface 4). At surface 7, corresponding to the condenser section, the fine mesh shows a Cp very close to the mid grid value, in fact, the difference is below 1%. The Mid mesh is illustrated in Figure 2.3.

On the contrary, the pressure recovery coefficient computed by the coarse grid is always below the fine grid trend, with an average deviation of 7%. In the same chart, the geometrical area variation that is experienced by the flow is represented in terms of area ratio (AR), namely the ratio of the post-processing surface area to the diffuser inlet area. As expected, the recovery process is totally localized in the diffuser, where the area

ratio is increasing. Downward from the diffuser, in the collector box, which acts as a junction between the diffuser and the condenser, the Cp drops as the effect of losses although the AR is still increasing. As will be in-depth explained in the chapter 3 and observable in Figure 1.5 the flow field this region is dominated by the presence of strong vortices which are sources of significant losses leading to the drop of performance shown.

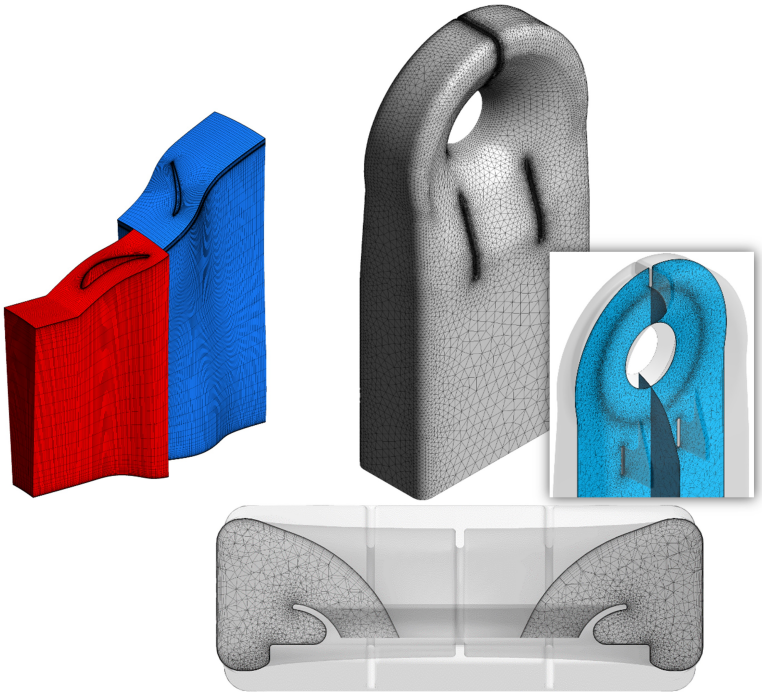

Figure 2.3: Last stage and exhaust hood computational mesh

To conclude the grid independence study, the GCI criteria are reported below, and the outcomes for each mesh resolution, as well as the properties of the grid are summarized in Table 2.2. The pressure recovery coefficient, computed at the condenser inlet, has been considered as the variable subject of the GCI analysis. The results demonstrate that the discrete

solutions converge monotonically as the grid is refined, as shown in Figure 2.4. The ratio of the characteristic grid spacing from coarse to medium (r_{cm}) and from medium to fine (r_{mf}) is 1.68 and 1.44 respectively, consequently the order of convergence of the discretization (p) can be computed solving Equation 2.2 iteratively [126], where Cp_c, Cp_m, and Cp_f are static pressure recovery coefficient of coarse, medium and fine grids.

$$p = \frac{ln\left[\frac{Cp_c - Cp_m}{Cp_m - Cp_f}\right] + ln\left[\frac{r_{mf}^p - 1}{r_{mf}^p r_{cm}^p - 1}\right]}{ln(r_{mf})} \tag{2.2}$$

As the apparent order of discretization is known, the GCI for the fine and medium grids are given by Equations 2.3 and 2.4.

$$GCI_f = \frac{1.25|(Cp_m - Cp_f)/Cp_f|}{r_{mf}^p - 1} \tag{2.3}$$

$$GCI_m = \frac{1.25|(Cp_c - Cp_m)/Cp_c|}{r_{cm}^p - 1} \tag{2.4}$$

Table 2.2: Grid refinement results and mesh properties.

Grid Refinement level	Elements number	h [mm]	Normalized Cp
coarse	0.84 Million	13	0.559
mid	4 Million	7.8	0.575
fine	12 Million	5.4	0.579

The GCI measures the distance between results and the asymptotic value. In the analysis under consideration, the observed order of convergence is equal to 1.93, with a GCI for medium and fine grids of 1.97% and 0.97% respectively, indicating that the computation is within the asymptotic range, the reason why the medium size grid has been selected to perform the interface models comparison.

2.1.2 Rotor-Hood Interface Model Assessment

In this sub-section, the results coming from the FFR and FMP simulations are compared, by studying the trend of normalized Cp along

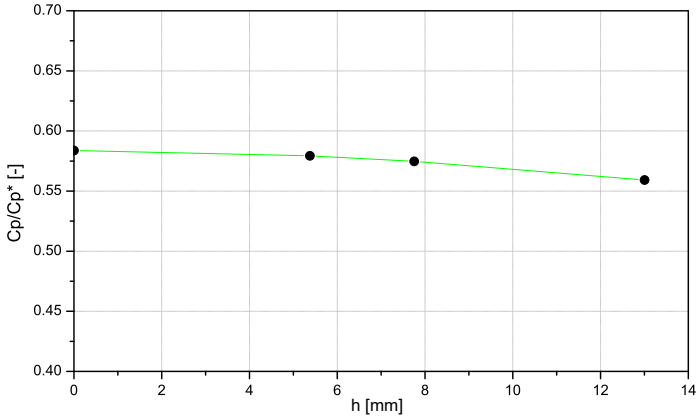

Figure 2.4: Results of GCI criterion: behaviour of Cp as the mesh is refined

the flow path, as well as analyzing the pressure and velocity field distributions within the exhaust hood. In the mixing plane approach, at the stage interface, ANSYS CFX allows two possible averaging operations for velocity on the downstream side. The total pressure can be conserved performing a circumferential average of flow direction in the rotating frame (Constant Total Pressure option, referred as CTP), in this way the downstream velocity profile adjusts naturally to downstream static pressure values; alternatively, the downstream velocity can be computed by circumferentially averaging the absolute velocity in the rotating frame (Stage Average Velocity option, referred as SAV). In this work both options were assessed, therefore the model recurring to the CTP option will be referred to as FMP-ctp model, while the other as FMP-sav model. The FMP-ctp model was adopted in the grid sensitivity study discussed in the previous sub-section.

Figure 2.5 shows the trend of normalized pressure recovery coefficient as a function of interface coupling models, computed along the flow path on the post-processing surfaces.

As it can be seen, both FMP models predict a lower recovery perfor-

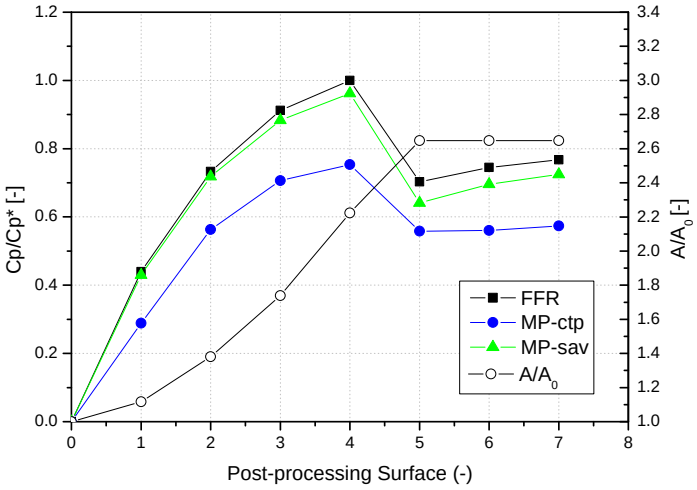

Figure 2.5: Behavior of Cp on post-processing planes as a function of interface coupling modeling

mance of the exhaust system with respect to the frozen rotor solution but, whereas the mixing plane model with the CTP option averagely underestimates about 25 percent, the FMP-sav simulation shows results very close to the FFR ones. Focusing on the FMP-sav model, a very well agreement with the FFR in the diffuser region is clear: it is shown a difference that grows along the flow path, however reaching a maximum underestimation of just 3.8% at the diffuser exit (surface 4). Downstream, the drop of pressure recovery coefficient occurs in every simulation, which is less intense in the case of CTP option, but in the final part of the exhaust hood gets up again in FFR and FMP-sav models. The plot shape of these last simulations is practically the same with a negative deviation of the pressure recovery coefficient at the condenser surface equal to 5.2 percent: such a difference is more than acceptable, given the significant saving in terms of numerical cost, which was reached thanks to a reduction by 80 percent of the grid elements number. For a better understanding of the differences in the pressure recovery coefficient coming

from the interface coupling modeling and, in particular, from the effect of the various averaging options available in the mixing plane model, the contour plots of static pressure and the absolute velocity at the inlet of the exhaust system are presented in Figure 2.6.

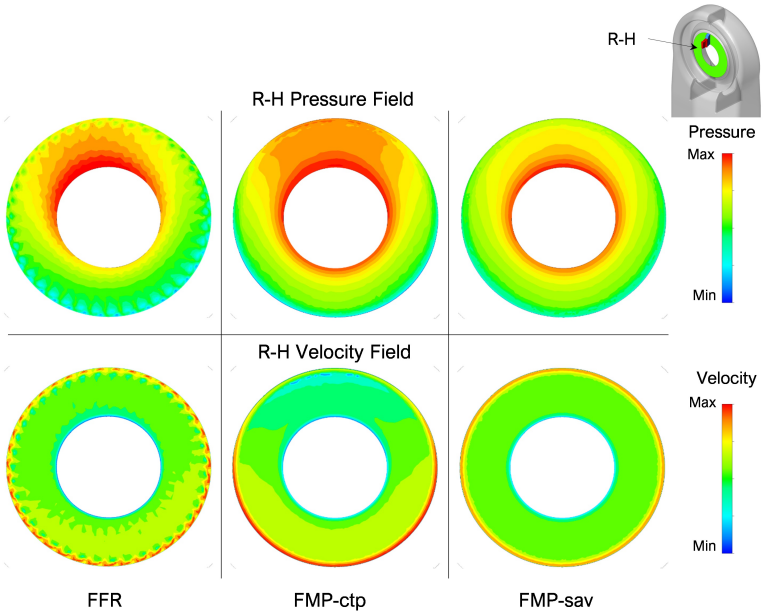

Figure 2.6: Contour plots of static pressure and absolute velocity module at the Rotor-Exhaust hood interfaces, for both FFR and FMP models.

From a qualitative point of view, it can be seen how, in the frozen rotor simulation, the static pressure distribution is characterized by a radial gradient located on the half upper part of the rotor-diffuser interface, while in the lower part the pressure is more uniform. As regards velocity contour, it can be considered uniform in the circumferential direction with a good level of approximation. Focusing on the mixing plane simulations, both models compute a radial pressure gradient at the interface upper region, with the CTP model showing pressure values closer to the FFR solution,

whereas SAV pressure values are lower in average on the interface upper zone. As far as the velocity distributions are concerned, the mixing planes models show significant differences at the maximum radius, right where the rotor tip leakage jet is located, clearly visible in the velocity contour relative to FFR simulation. The circumferential averaging operation of the velocity vector applied by the FMP-sav model leads to a uniform distribution of the velocity field at the exhaust system inlet, while, on the contrary, the CST option introduces a non-uniformity in the rotor tip leakage speed distribution: in detail, such a velocity is constant and with a unit value (normalized velocity) in the lower part of the interface, whereas in the half upper it decreases from the rotating axis towards the top region, where the speed stands at 67 percent of the maximum. In addition, it is interesting highlighting how the asymmetry of the radial diffuser affects the pressure field at the LSB outlet, indeed, as already presented in the literature review the strong pressure gradient between the upper and lower leads to a different load of the rotor blades which moves in that region. By virtue of this, It can be therefore concluded that is essential to consider the exhaust hood in the last stage numerical calculation.

The effect of these differences on the pressure recovery coefficient is assessed through a study of the Cp's circumferential distribution on the post-processing surface S2, shown in Figure 2.1. Such a surface has been circumferentially divided into 40 sectors having the same area, hence on each one, the Cp, as well as the velocity, have been computed, collecting the results into the polar charts shown in Figure 2.7. It is worth mentioning how this approach to characterize the tangential Cp distribution should be used only when the swirl of the flow at the diffuser inlet is near to zero, as in the case of the design operating condition. Otherwise, due to the effect of the swirl, the Cp distribution should be computed by considering the stream tube of the flow.

By looking at Figure 2.7 it can be shown how the diffuser does not work uniformly over the 360 degrees, indeed, the pressure recovery occurs mainly in the upper half, with a reduction in the recovery performance

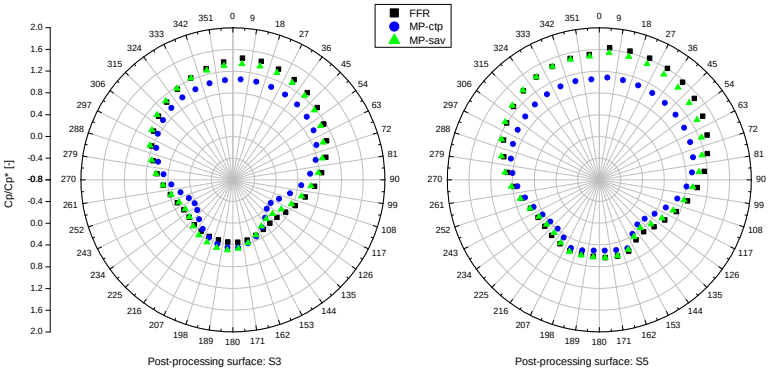

Figure 2.7: Polar charts of absolute velocity (on the left) and normalized Cp (on the right) computed on the post-processing surface S2 for the different interface coupling models.

even the 50% in the lower half. The data related to the FMP-sav model, green triangles in the right chart of Figure 2.7, compares very well with those coming from the frozen rotor simulation, with small deviations mainly located within the angular sector 0° 135°. On the contrary, the FMP-cst model shows Cp values (blue dots) lower than the FFR ones (black squares) on almost the overall annular channel, except for the angular sector 162° 207°, with a maximum deviation between 288° and 63°, precisely in the region where the rotor tip jet is very weak. Moreover, by studying the velocity polar chart, left plot in Figure 2.7, it can be seen how, in that angular region, the area-averaged velocity computed for the FMP-ctp simulation is always below the FFR and FMP-sav results. For an in-depth investigation of this effect is useful to observe the velocity contour reported in Figure 2.8. In particular, by looking at the velocity field on the vertical plane cutting the exhaust hood geometry into two halves, it is clear how the FMP-ctp exhibits a flow separation along with the steam guide. This flow separation acts as an aerodynamic blockage reducing the available flow passage area and causing the pressure recovery drop shown in both Figure 2.5 and 2.7. The FFR and FMP-sav do not reveal this flow feature since, in line with what is shown in literature, it is

strongly affected by the tip leakage flow and both these interfaces predict a strong leakage jet in the tip of the rotor-hood interface, as observable in Figure 2.6, such jet energizes the flow in the boundary layer avoiding the flow separation. This is additional proof of the beneficial action of the tip jet in countering the flow separation at the steam guide, therefore it is paramount that the interface coupling model does not alter the jet velocity on the downstream interface. In addition, it is also interesting to highlight how the presence of counter-rotating tip vortices is revealed by all the numerical setups, the cores of these vortices are clearly visible in the post-processing surfaces located in the collector box with almost zero velocity regions. This means that the formation of these flow structures is not correlated with any flow separation in the diffuser, but it is linked to the radial geometry of the diffuser which forces the flow to experience a 90° degrees change of direction in a very short distance. Such a problem, largely responsible for the pressure recovery drop downstream of the diffuser, can not be therefore solved with an optimization of the diffuser itself but can be just mitigated by acting on the collector box shape.

To summarize, the FMP model has proved to be a good tool to assess the exhaust hood performance, with acceptable deviations from results coming from a frozen rotor simulation and with a significant reduction in numerical cost, especially in the view of using CFD simulations to carry out DOE studies oriented to geometry optimization. Moreover, this research has highlighted as, for the mixing plane model, it is relevant to choose the right velocity averaging operation to be performed on the domains' interfaces, in order to achieve results consistent with the frozen rotor ones, in particular, a circumferentially averaging operation of the absolute velocity in the rotating frame should be adopted (Stage Average Velocity option in ANSYS CFX). However, it is worth recalling how these findings have been obtained in design operating condition where the swirl of the flow at the diffuser inlet is near to zero. In this regard, it is appropriate to expect higher deviation for the interface model in off-design conditions, which are characterized by stronger disuniformities of the flow in the tangential direction.

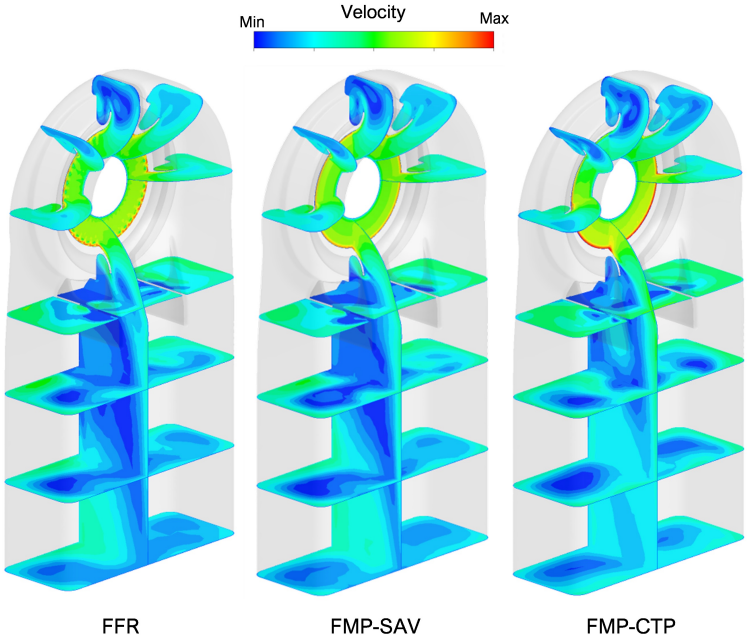

Figure 2.8: Absolute Velocity field within the exhaust hood: FFR, FMP-sav and FMP-ctp

2.2 Axial Exhaust Hood

In this section, a numerical investigation on the flow-field and aerodynamic performance of a low-pressure steam turbine axial exhaust hood through CFD simulations is presented. The characteristic flow field of the axial exhaust hood is presented and the differences respect to the radial configuration are highlighted. Due to the strong coupling between the last stage and exhaust hood, the assessment on the interface models has been repeated and in this case and even expanded with an unsteady numerical simulation which represents the most accurate numerical solution in the state-of-art. In the final part of this section, the focus is moved on the influence of struts by evaluating their impact on the aerodynamic

performances of the diffuser. Both the investigations presented in this chapter are obtained by considering design operating conditions, with an average diffuser inlet swirl near to zero. The effect of swirl on both the interface models and structural struts is instead presented in Chapter 4.

2.2.1 Rotor-Hood Interface Model Assessment

The computational mesh used for this study has been obtained with the same procedure presented in the previous section 2.1. Concerning the numerical setup, for the steady-state simulation, the same choices presented in the section 2.1 are replicated.

In this investigation two different fluid domains, reported in Figure 2.9, have been studied: periodic and fully 3D. Rotor tip clearance is included in both the fluid domains. The periodic model uses the mixing plane as frame change type and it consists of a single last stage passage coupled with a periodic slice of the diffuser, therefore, neglecting the presence of structural struts which break the symmetry of the diffuser.

The 3D domain considers a full annulus mesh of both the last stage and the axial exhaust hood with struts included, as shown in Figure 2.10. In this case, the frame change types used are the already presented Frozen Rotor and the transient interface. Such a method, available in CFX, is capable to capture the flow unsteadiness by using a rotor moving mesh. The main drawback of this approach is the huge computational cost required, almost twenty times higher than the expensive Frozen Rotor and four hundred times respect to the Mixing Plane.

The transient (URANS) simulations have been solved with a second-order backward Euler scheme and a time step of 2.3e-5 [s], resulting in 15 rotor mesh steps per pitch angle, which is sufficient to properly catch the blade passing effect. The total physical time simulated is equal to 10 complete rotor revolutions (REV). Considering the fluid domain and the high physical time simulated, the average computational cost of each unsteady simulation is almost 100 K CPUh. As convergence criterion for unsteady simulations the summation of the resultant force on all blades has been considered, the minimum number of time steps is then

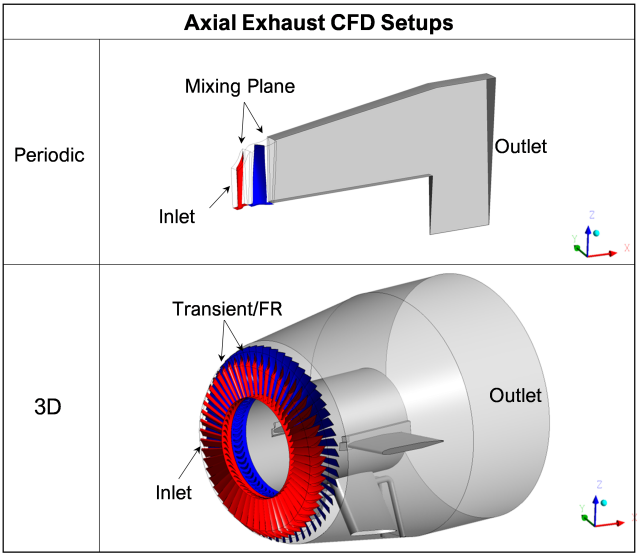

Figure 2.9: Axial exhaust hood numerical setups

reached when this monitor is stable with relative oscillation below 3%, the additional time steps above this minimum have been decided based on the author's experience in order to collect sufficient transient data for the post-processing.

The effect of a different numerical setup on the flow field can be understood by looking at Figure 2.11. The flow field obtained with the mixing plane has been expanded over 360 deg for a better comparison with the others. This interface model offers a diffuser inlet flow field prediction in agreement with the others confirming the findings proposed in the radial exhaust hood investigation, with the exception of the rotor wake. The latter can be predicted with the Frozen Rotor, however, as already found in the literature review, this method shows a tendency to overestimate the wake effect if compared with the instantaneous transient solution. For a broader perspective of the flow field, it is interesting to look at Figure 2.12.

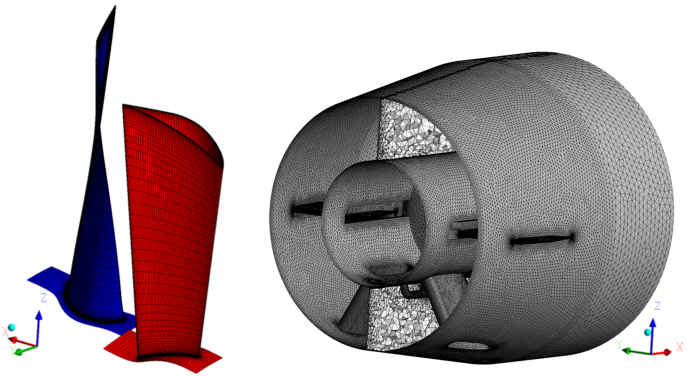

Figure 2.10: Last stage and axial exhaust hood computational grids

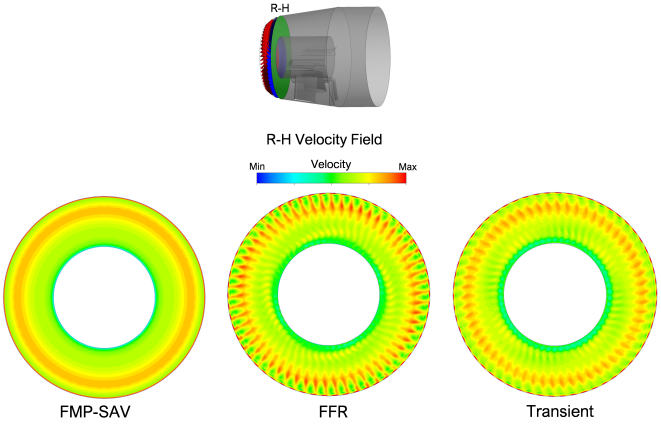

Figure 2.11: Velocity field in rotor-hood interface: FMP-sav, FFR and Transient

First of all, it is clear how the flow field of the axial exhaust is less complex than the radial one. The strong vortices which characterized the flow field of the latter are almost absent in the design operating condition of the axial diffuser, this leads to reduced losses and therefore higher pressure recovery. The main weak point of this exhaust hood

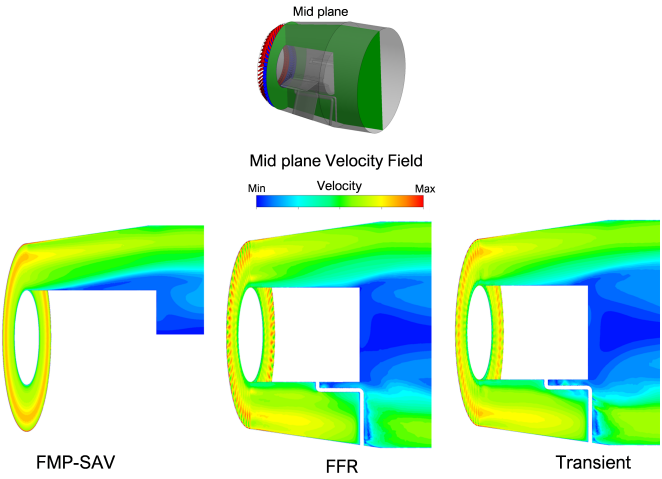

Figure 2.12: Velocity field within the exhaust hood: FMP-sav, FFR and Transient

is the hub separation, as visible in Figure 2.12. However, in design operating condition it is extremely reduced as predicted by Frozen Rotor and Transient numerical setups, while the Mixing Plane shows a higher hub separation. This effect can be explained by considering the main difference between these models found in Figure 2.11: the wake effect. Indeed, the Frozen Rotor model which presents the highest wake intensity prediction is also the one with the smallest hub separation.

Concerning the performance estimation, the mixing plane setup presents a C_p of 21% higher respect to the transient one, however, this can be explained with the absence of the struts in the periodic model. The Frozen Rotor estimates a C_p 15% higher than the transient one, this effect can be instead justified with the different resolution of the hub separation.

2.2.2 Influence of Struts

This sub-section examines the effect of the struts on the exhaust system performance. The struts are the supports of the exhaust hood

which ensure its structural integrity, in the investigated geometry they are located in the lower part of the exhaust system, as can be seen in Figure 2.10.

This analysis is an excerpt, focused on the design condition, of a wider investigation reported in Chapter 4. Due to the high number of simulations analyzed in the complete study, the mixing plane interface has been selected to perform this assessment. The axial exhaust hood has been simulated with and without the presence of struts and the results are shown in Figure 2.13.

The exhaust hood performances are analyzed by computing the pressure recovery factor (C_p) (Equation 1.1), the total pressure loss coefficient (C_{tpl})(Equation 1.2), and the residual kinetic energy coefficient (C_{rke}) (Equation 1.3) in the post-processing surfaces located along the flow path. All the post-processing coefficients are normalized respect to a reference value and their trend is plotted against the normalized axial length.

The strong impact of the struts on the performance is clear by looking at the charts reported in Figure 2.13. The first and second dashed lines highlight the struts region, where a significant drop of the pressure recovery is present and at the same time an increase of C_{tpl} and C_{rke}. The drop of performance in the struts region seems therefore linked to a dual effect: increase of losses and flow acceleration (an increase of residual kinetic energy). The first effect can be explained by considering the flow separation due to the effect of non-aerodynamic bodies (struts), such an effect can be seen in Figure 2.14 with a zero-velocity region generated behind the struts. This effect dramatically increases in off-design conditions as the effect of the high inlet swirl (deeply discussed in Chapter 4). The flow acceleration is instead linked to the decrease of the flow passage area generated by the presence of struts which leads to an increase of axial velocity flow field. Finally, it is worth noticing the significant difference in the C_p evaluated at the real outlet (third dashed line in Figure 2.13) and the numerical outlet. Although the geometric area ratio is constant in this region, the pressure recovery increases due to a dissipation of the vortices generated by the struts.

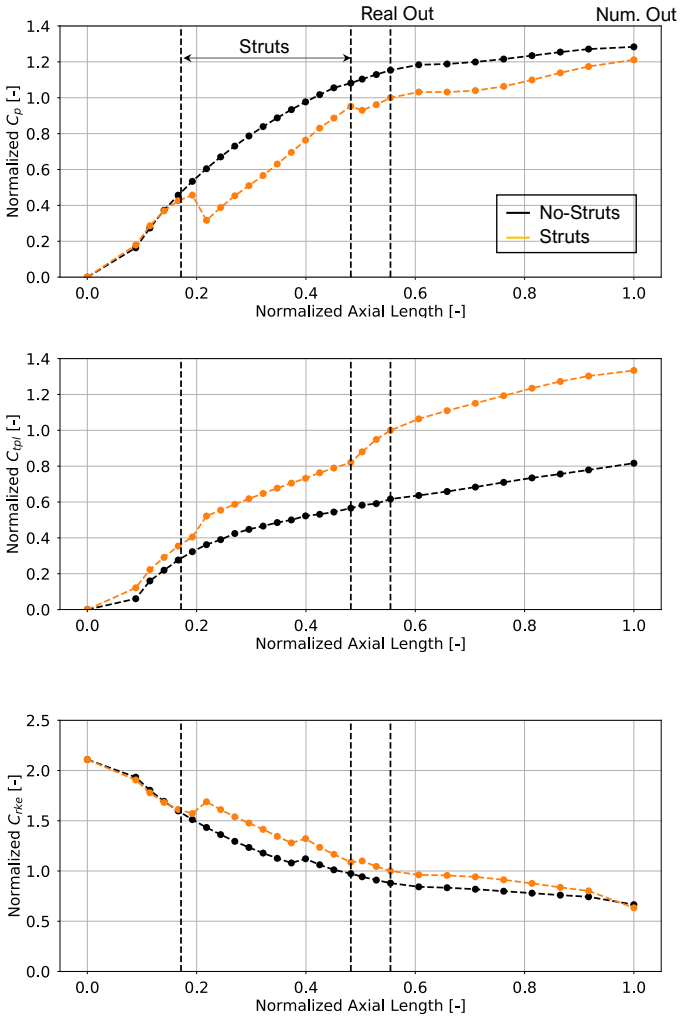

Figure 2.13: C_p,C_{tpl} and C_{rke} trend along the diffuser with and without struts

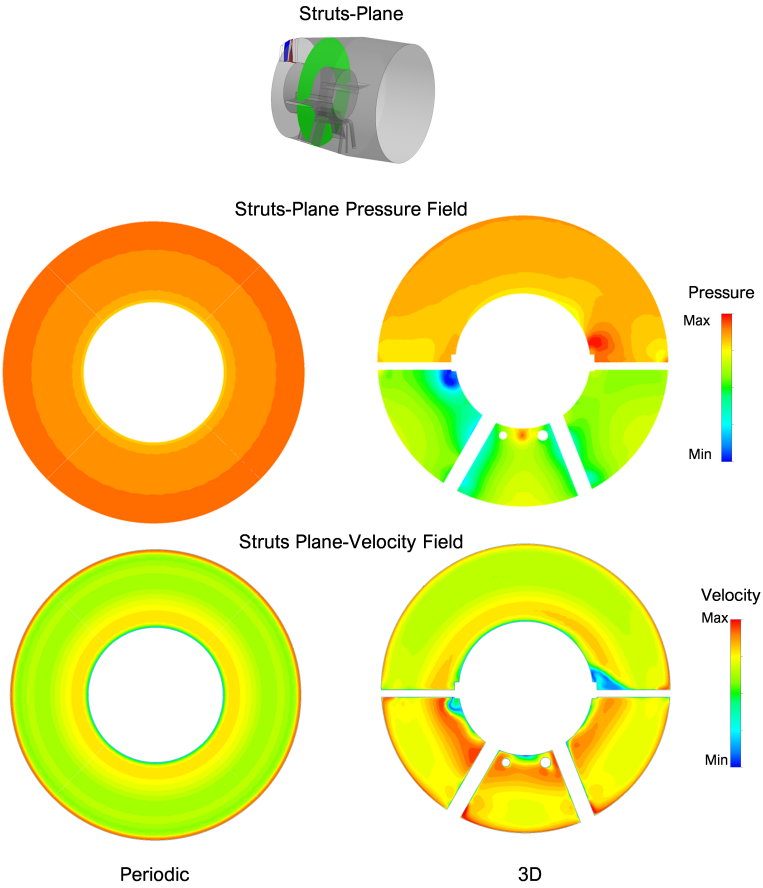

Figure 2.14: Pressure and velocity field with and without struts

Chapter 3

Exhaust System Design Approach

This chapter describes the development of a numerical procedure for the design of a steam turbine exhaust system. The description of such a procedure is split into two parts, which corresponds to the main steps toward the definition of the final tool. These steps are also reported in two publications [127, 128].

The developed design tool has been applied only on the radial configuration of the exhaust hood, since it is the more complex one from an aerodynamic point of view, as explained in Chapter 1. The axial configuration does not need a dedicated procedure since its design is standard and obtained with years of experience in the axial annular diffuser design criteria.

The CFD setup has been decided by virtue of the findings proposed in Chapter 2 and it is based on mixing plane interfaces. Despite the impact of the struts shown in the previous chapter, such geometry feature is neglected in the first instance for the sake of reducing the computational cost. The numerical procedure is indeed based on a high number of numerical simulations and it is, therefore, necessary to minimize the computational burden of each simulation. The detailed aspects, such as the 3D effect of the LSB or the presence of struts, can be considered in a following step of the design process.

3.1 Development of Design Approach-Part 1

This section describes the first step toward the development of the exhaust system design approach. The findings of this investigation are indeed essential for the identification of the complete procedure.

As already described in chapter 1, the radial exhaust hood is characterized by a complex flow field with highly rotational flow structures which are the main source of losses within the diffuser and exhaust hood outer casing. This section will illustrate how such losses can be mitigated with a proper design of the exhaust hood casing. Such a task has been accomplished by using a design of experiment (DOE) analysis implemented through CFD simulation.

Before proceeding with the DOE analysis, an example of retrofitting is presented. Indeed, a baseline geometry has been generated by integrating a new generation of low-pressure blades, manufactured by Baker Hughes for mechanical drive applications, with a previously designed radial exhaust hood. Such analysis shows the issues linked to the retrofitting by highlighting the low aerodynamic efficiency of the exhaust hood. The impact of a different exhaust hood geometry on these aerodynamic inefficiencies is assessed with a DOE analysis based on a parametric geometry of this component. It is worth highlighting how in this step the focus is only on the external casing while the diffuser is kept constant during the analysis due to an industrial design constraint.

3.1.1 Baseline Geometry Analysis

In this sub-section, the results of the baseline geometry (Dp0) are discussed. The exhaust hood performances are analyzed both exploiting flow field visualizations and by computing the pressure recovery factor (Equation 1.1), the total pressure loss coefficient (Equation 1.2), and the residual kinetic energy coefficient (Equation 1.3) in the post-processing surfaces located along the flow path (red surfaces in Figure 3.1). The trend of the normalized C_p is reported in Figure 3.1, it is normalized by a reference value used in the normalization of every C_p of this section. The

same is valid for the other coefficients.

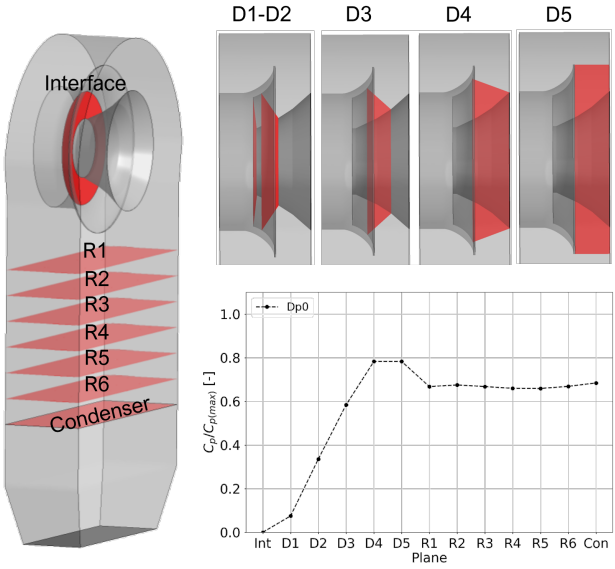

Figure 3.1: Cp behavior along the postprocessing surfaces for the baseline geometry.

As can be seen in Figure, the C_p rises in the diffuser up to the D4 surface where it stops growing. The flat trend between the surfaces D4 and D5 is an indicator of the non-optimal performance of the diffuser in this region. The physical explanation behind this trend is presented later by using a graphical representation of the flow field in the diffuser. Concerning the drop of the pressure recovery downstream of the diffuser (D5-R1), it is a very usual behavior of the radial exhaust system because, in this region, the low momentum flow coming from the upper part of the exhaust hood, which has already lost a substantial part of its kinetic energy, is mixed with the high momentum flow coming from the lower part of the exhaust hood. The mixing implies the onset of high velocity gradients between the two streams and consequently high viscous losses

as can be seen by the abrupt rise of the C_{tpl} in this region in Figure 3.2. In addition, as already mentioned in Chapter 1, in this region two strong counter-rotating vortices are generated leading to a further increase of losses. In the same graph also the residual kinetic energy behavior is shown: it presents a decreasing trend, as expected, with a change of slope between the section D4-D5 that justifies the flat trend of the C_p identified in this region. This behavior is an indicator of local acceleration of the flow which is due to aerodynamic inefficiency of the final section of the diffuser, that the averaged values reported in Figures 3.1 and 3.2 are not able to catch. For a deeper understating of this effect, the circumferential C_p behavior is reported in the polar charts computed on D4 and D5 surfaces in Figure 3.3.

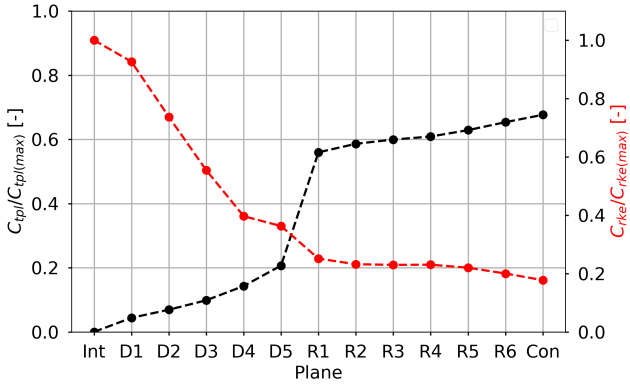

Figure 3.2: C_{tpl} andC_{rke} behaviors along the postprocessing surfaces for the baseline geometry.

The polar chart shows how the diffuser does not work uniformly over 360° deg since the pressure recovery occurs mainly on the upper part. This effect is particularly pronounced in the D4 surface, while in the D5 one the performance difference between the upper and lower part is smaller, mainly because in the upper part the diffuser does not work efficiently. This zone of low performance leads to the flat behavior of the C_p observed

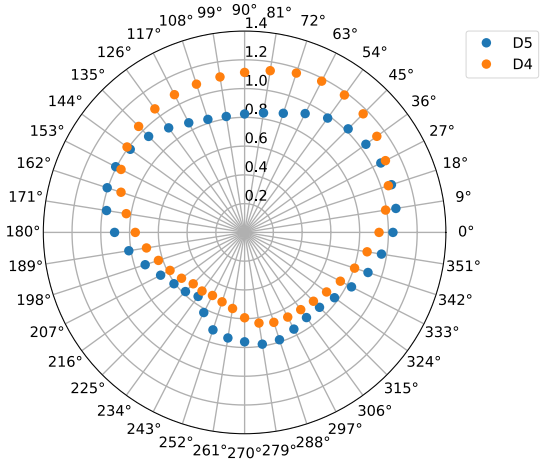

Figure 3.3: Polar charts of normalized C_p computed on the postprocessing surface D4 e D5 for the baseline geometry.

in Figure 3.1.

To clarify, this aspect is useful to observe the 2D velocity streamlines in Y0 plane reported in Figure 3.4a. The Y0 plane cuts in half the low performance region identified by the polar chart: the streamlines show a wide separation area originating from the internal diffuser wall (the so-called hub cone separation) which drastically reduces the available passage area for the flow and, therefore, it acts as an aerodynamic blockage. The reduction in the aerodynamic area leads to a flow acceleration causing the C_p local decrease and the slope change in the C_{rke} trend.

The hub cone separation promotes the onset of a recirculation region (pointed as A in 3.4) which extends along the entire exhaust hood up to the condenser section through the secondary vortex pointed as A in Figure 3.4b. Moreover, the acceleration of the flow due to the aerodynamic blockage affects the magnitude of the main vortex (exhaust tip vortex), indicated as B. Figure 3.4b illustrates the 3D velocity streamlines which

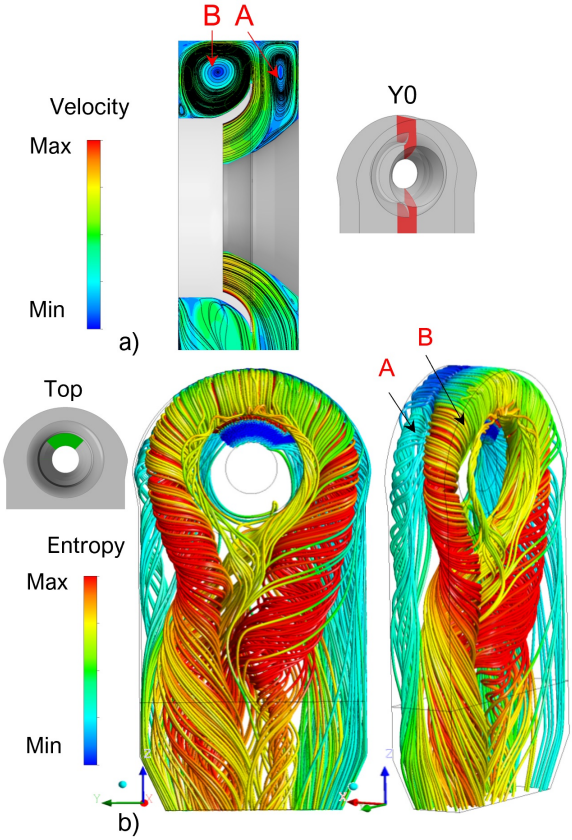

Figure 3.4: Flow field visualization of DP0 (a) 2D velocity streamlines and normalized velocity contour plot on Y0 plane, (b) 3D velocity streamlines originating from the top section colored by normalized entropy.

originate from the top section of the diffuser inlet, colored by normalized entropy. This sector-wise streamlines flow field visualization, also used by other authors [13, 76], allows to show the complex 3D flow inside the exhaust system. Only the streamlines originating from the top section are

shown since previous investigations have demonstrated how the strongest vortices are located in this region. The high values of entropy qualitatively identified for vortex B clarify how this vortex is the main source of losses in the exhaust system. These post-processing techniques have been systematically applied for all the design points.

3.1.2 Design of Experiment

The results presented in the literature review show how the optimization of the exhaust system geometry can help to reduce the vortices' strength, leading to a decrease in the overall losses and consequently increasing the C_p.

As already discussed in chapter 1, a fundamental step before the implementation of an optimization procedure is the definition of the geometric parameters to be varied in the DOE. In this regard, the results presented in this chapter deals with a sensitivity analysis aimed at assessing how the three geometric parameters, illustrated in Figure 3.5, impact, both qualitatively and quantitatively, on the exhaust system performance. The geometric parameters are defined as follow:

- R: is the radius of the cylinder forming the upper part of the exhaust hood
- Δz: is the vertical distance between the axis of the cylinder forming the upper part of the exhaust hood and the turbine axis of rotation. This parameter allows to obtained a gradually increasing flow passage area from top to mid sections of the external casing, as schematically shown by the red arrows in Figure 3.5a. The combination of R and Δz determines the maximum height of the exhaust system.
- L: is directly linked to the axial size of the exhaust hood

Different values of these parameters lead to a change of two characteristic areas of the exhaust system: A2 and A3, reported in 3.5c, the same areas investigated in a previous work found in literature [74]. A0 has not

been varied since it is defined by the rotor blade spanwise dimension, as well as A1 which is related to the diffuser geometry, fixed in this investigation and designed with Baker Hughes' best practice defined by previous investigations [36, 39]. It is interesting highlighting how the latter design constraint is one of the main limits of this first attempt to develop a design approach, as will be shown later in this Chapter. Finally, as a further design constraint, the width of the exhaust hood outlet section is fixed by the dimensions of the condenser's flange. In this chapter R, L, and Δz are presented as normalized quantities by the last stage blade height (h) calculated in the final section of the rotor.

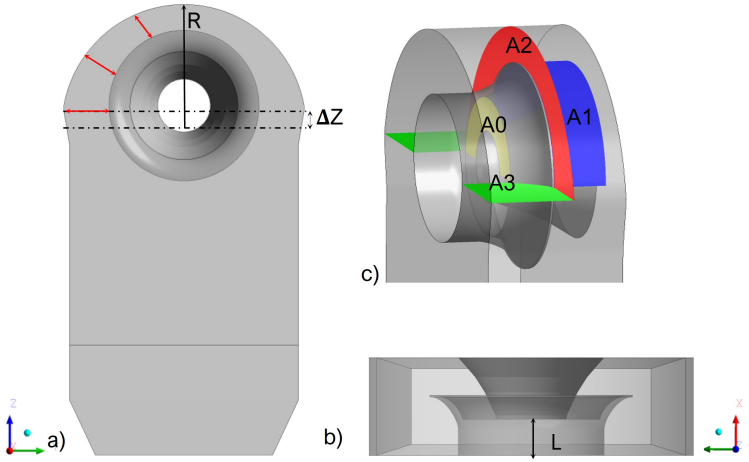

Figure 3.5: Parametric geometry: a)Frontal view with R and Z b) top view with L c) Significant exhaust hood areas.

The design points were created with the Latin Hypercube Sampling algorithms available in ANSYS workbench. The total number of design points simulated is 32 however, for the sake of ease the description of the results, only a selection of the most representative of these are deeply discussed; the geometric features of such a cluster are reported in Table 3.1 , together with the percentage changes of volume (W) respect to the

baseline geometry.

Table 3.1: Geometrical dimensions of the investigated design points.

Design Points	Δz/h	R/h	L/h	$(W\text{-}W_{Dp0})/W_{Dp0}$
Dp0	0.87	5.00	1.11	0%
Dp2	1.46	6.02	1.11	10%
Dp3	1.26	5.34	1.11	1%
Dp4	1.07	3.98	1.11	-12%
Dp5	0.88	6.36	1.11	22%
Dp9	0.10	4.32	1.11	-3%
Dp13	0.87	5.00	2.01	28%
Dp14	0.87	5.00	0.29	-29%
Dp22	0.57	4.46	0.86	-14%
Dp25	0.77	5.00	1.11	17%
Dp29	1.60	6.27	1.86	38%

3.1.3 Response Surface

The results of the numerical simulation have been post-processed in ANSYS workbench to define a four dimensions response surface. The coefficient of determination of the response surface is 0.99, and it is, therefore, able to predict with good accuracy the CFD C_p at the condenser section as a function of the geometric parameters.

The influence of each investigated parameter can be understood by analyzing the response surface using a 2D slice representation, illustrated in Figures 3.6 and 3.7. More in the point, in Figure 3.6, the three-dimensional response surface, achieved for a fixed value of L, is sliced with planes at constant R, while in Figure 3.6, the same 2D slicing is done to the three-dimensional response surface resulting by a fixed value of Δz. In the same charts, the simulated design points are illustrated, pointed as small squares. The grey ones are those discussed with greater attention in this investigation.

The strong influence of R on the exhaust hood performance is clear by observing both the graphs reported in Figures 3.6 and 3.7 , where an

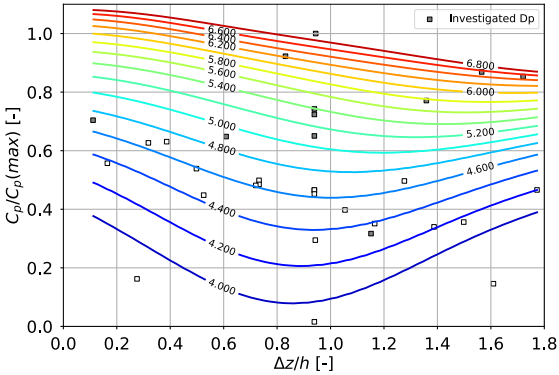

Figure 3.6: 2D slice of 3D response surface generated with a fixed value L/h, the contour lines have a fixed value of R/h.

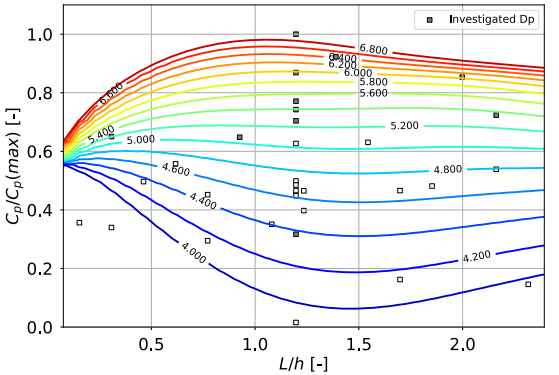

Figure 3.7: 2D slice of 3D response surface generated with a fixed value Dz/h, the contour lines have a fixed value of R/h.

increase of R usually leads to higher performance of the exhaust hood. Concerning the variations of Δz, the response surface identifies, for high values of R, an optimum C_p value when Δz is near to 0, meaning that

for high values of the radius the misalignment of the rotation axis and cylinder axis should be avoided. This misalignment allows to obtain a gradually increasing cross-sectional area moving from A2 toward A3, which could promote the deceleration of the flow, but, as a side effect, it reduces the exhaust hood maximum height for a fixed value of R.

For medium-low values of R, the shape of the response surface radically changes. In this region, Δz becomes more important by determining a minimum of the C_p in correspondence of Δz/h 0.9. This trend can be explained considering that the combinations of values of Δz/h around 0.9 and values of R/h below 5.2 represent the worst tradeoff between the two aforementioned aspects, meaning that the maximum height of the exhaust hood is not enough to ensure high performance in the diffuser, as will be shown in the following, and the misalignment of the rotation axis induced by Δz is not such as to ensure a high deceleration of the flow or mitigation of the vortices' strength. From this point, an increase of Δz improves the performance of the exhaust hood by decelerating the flow and a decrease of Δz still enhances the performance by increasing the maximum height of the exhaust hood.

The effect of the axial size L is reported in Figure 3.7 , where it is clear how, for a sufficiently high value of R, an increase of L has a positive influence on the pressure recovery performance until a peak of C_p is reached. Further increase of L does not lead to an improvement in the performance but only contributes to an unnecessary increase in the volume of the exhaust hood. For medium values of R, the effect of L is almost zero, meaning that if the exhaust hood height has not reached optimum values, an increase of the hood depth does not impact the performance.

The global trends of the post-processing coefficients along the flow path are shown in Figure 3.8.

The most performing exhaust hoods are Dp25 and Dp5, with a percentage increase in volume, compared to the baseline geometry, of 17% and 22%, respectively. As can be seen, the most performing geometries are those in which the diffuser works optimally with a constantly increasing

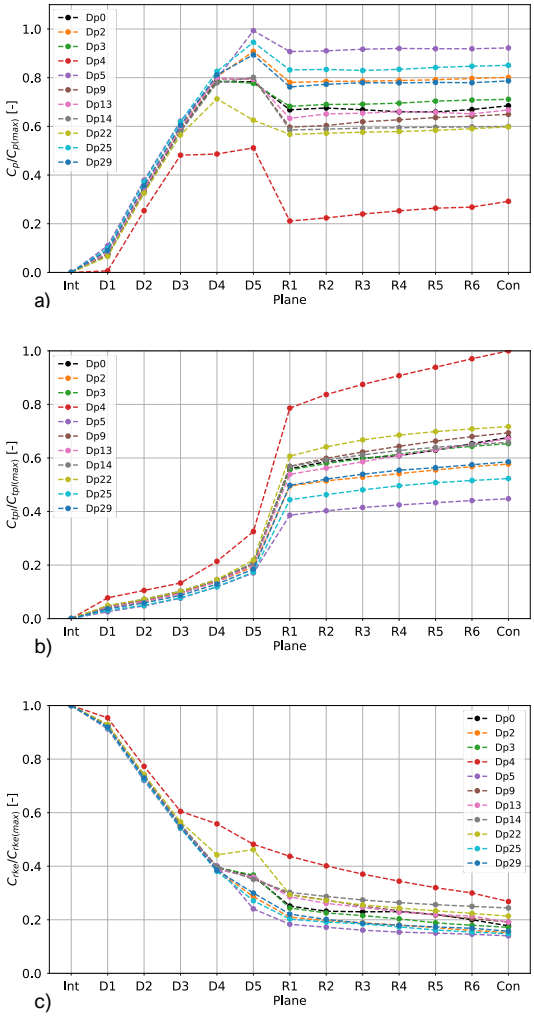

Figure 3.8: (a) Cp, (b) Ctpl, and (c) Crke behavior along the postprocessing surfaces.

trend of the pressure recovery from the Rotor-Hood interface (Int) up to the final section of the diffuser (D5). The increase of the performance in the diffuser is directly linked to the reduction of the separation region pointed as A in Figure 3.4. By remembering that the diffuser geometry has not been varied in the DOE procedure, all the differences showed in diffuser pressure recovery in Figure 3.8 are a consequence of a change in the geometry downstream of the diffuser, meaning that there is a strong interaction between the diffuser and the outer casing of the exhaust system.

3.1.4 Impact of Exhaust Hood Height

For in-depth knowledge physical mechanisms behind the illustrated trends it is useful to observe the flow field visualization reported Figures 3.9 and 3.10. Specifically, in Figure 3.9 the influence of the maximum hood height is presented by comparing the Dp5, which has the maximum hood height, and the Dp4, characterized by one of the lowest hood heights. Both the compared geometries have the same value of L, and consequently, all the effects shown are related to the hood height variations only.

By observing the 2D streamlines reported in Figure 3.9a, related to Dp5, it can be seen a reduction in the hub cone separation area into the diffuser compared to the baseline geometry (Figure 3.4); this aspect justifies the improvement in the performance of the Dp5, identified in Figure 3.8 with an upward trend of the pressure recovery along the entire length of the diffuser. However, the separation area is still present since it is strongly affected by the diffuser hub cone geometry, which is constant in this investigation; the separation area dimension is still reduced and consequently, the local drop of the C_p due to flow acceleration is minimal; this effect, combined with a greater volume of the upper part of the exhaust hood, help to mitigate the strength of the main vortex B, as indicated by the small increase of losses between the section D5 and R1 in Figure 3.8 and by the lower values of the entropy showed in the Figure 3.9c. As a further contribution to the decrease of losses, the reduction of the separation help to suppress the secondary vortex A.

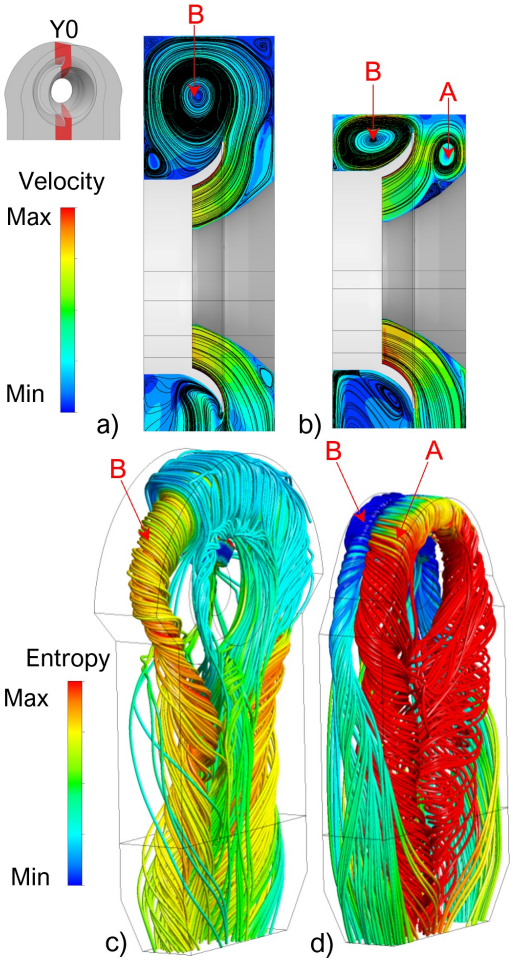

Figure 3.9: 2D velocity streamlines and normalized velocity contour plot on Y0 plane for Dp5 (a) and Dp4 (b); 3D velocity streamlines originating from the top section colored by normalized entropy for Dp5 (c) and Dp4 (d).

In Figures 3.9b and 3.9d, the effect of the hood height reduction is assessed. The overall performances are drastically reduced as already illustrated by Figure 3.8, where the Dp4 has shown the worst value of the C_p at the condenser section. One of the main reasons for these low performances can be understood by observing the 2D streamlines reported in Figure 3.9b, where the separation area in the diffuser is greater compared to Dp0 and Dp5 geometries; this leads to a poorly functioning of the diffuser, especially in the final sections as shown by the flat trend of the C_p between the planes D3–D5 in Figure 3.8. The 3D streamlines (Figure 3.9d) further clarifies the drop of the performance of this geometry by showing the high strength of the vortex B caused by the coupling effect of the aerodynamic blockage of hub cone separation, as well as the low volume of the upper part of the exhaust hood, which does not allow a proper diffusion of the vortex.

3.1.5 Impact of Exhaust Hood depth

The influence of the hood depth is discussed in Figure 3.10 by comparing the baseline geometry with the Dp13 and Dp14, which have, respectively, a greater and a lower value of L respect to the Dp0. Both the compared geometries have the same value of R and Δz and consequently, all the shown effects are related only to the hood depth variations. By looking at the Dp13 2D and 3D streamlines very small differences respect to the Dp0 can be seen. This supports the point made previously that an increase of L does not lead to the improvements of the exhaust hood performance when L has already reached optimal values. On the contrary, by looking at the Dp14 2D and 3D streamlines it can be understood how a decrease of L results in a considerable decline of the exhaust system performance. An excessively reduced depth of the hood provides a changed flow field with three distinct vortices that considerably increase the drop of the performance downstream of the diffuser, as illustrated by the trend of the C_p between surface D5 and R1 in Figure 3.8.

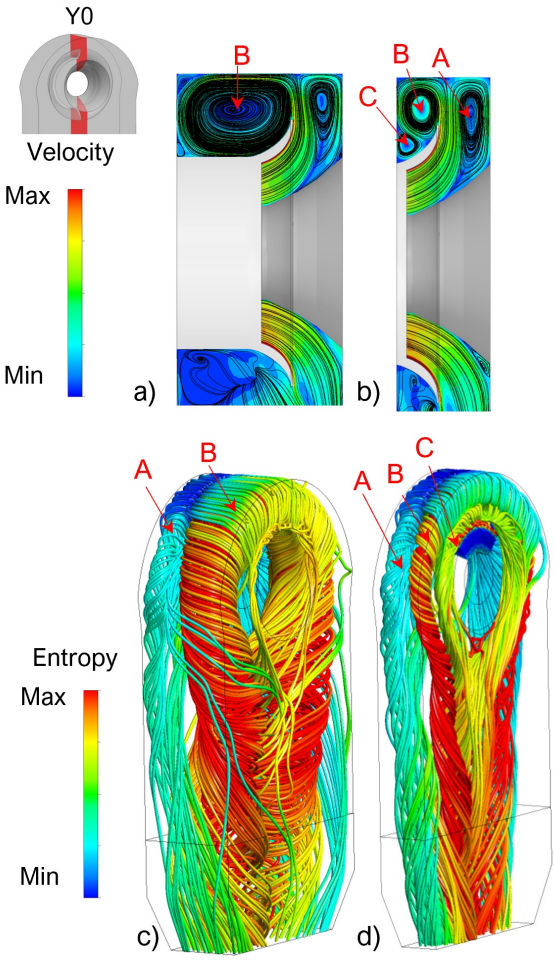

Figure 3.10: 2D velocity streamlines and normalized velocity contour plot on Y0 plane for Dp13 (a) and Dp14 (b); 3D velocity streamlines originating from the top section colored by normalized entropy for Dp13 (c) and Dp14 (d).

3.1.6 Concluding Remarks

To summarize, the influence of the investigated parameters has been studied both quantitatively, with the trends of three different performance parameters, and qualitatively with the visualization of the streamlines for an in-depth understanding of loss mechanisms, mainly linked to the onset and the spreading of the recirculating vortices. The considerable amount of data obtained in the DOE procedure has been processed to obtain a response surface which can support the design of the exhaust system. The design information resulting from the response surface trends, which are consistent with those reported in the literature, showing that there is an optimal value of the exhaust hood height below which the performance suffers a strong deterioration. Concerning the hood depth, its impact is closely linked to the hood height: for optimal values of the latter, there is a cut-off value of the hood depth below which the exhaust system showed very low performance. An increase of the hood depth above the cut-off value does not contribute to improving the aerodynamic behavior of the exhaust system but leads only to an unnecessary rise of volume. The procedure has led to a new exhaust hood geometry (Dp25) which shows an improved pressure recovery coefficient, about 24% greater than the baseline geometry for the investigated design operating condition. The Dp25 has been finally verified with both frozen rotor and transient numerical setup to numerically validate the performance improvement. The results of such verification are not reported since they confirm the findings already proposed in Chapter 2, which shows how the mixing plane can be used for qualitative comparison between different geometries since it is able to predict the major exhaust hood flow features during design operating conditions.

In view of the development of the design procedure, one of the most interesting findings proposed by this investigation is the strong effect of the exhaust hood upper wall (controlled by R) on the diffuser performance since it affects the hub cone separation. However, the optimization of the external casing can not be used as a single parameter to avoid this separation since it also depends on the diffuser hub cone geometry. It is

therefore possible to conclude that the optimization of the aerodynamic performance of the exhaust hood can not disregard the parameterization of both diffuser and external casing.

3.2 Development of Design Approach-Part 2

This section describes the development of the complete strategy for the exhaust hood design, it can be considered as an evolution of the one presented in the previous section. The latter shows the strong fluid-dynamic coupling between the diffuser and the exhaust hood casing, pointing out the importance of including into the DOE study the geometrical parameters of both components to increase the exhaust system performance. The complete procedure has been applied to the same exhaust system studied in the previous chapter and the major differences concerns an increased number of input parameters and a significant increase of the pressure recovery performance of the optimized geometry respect to the one described in the previous section.

3.2.1 Simplified Fluid Domain

On the basis of the aforementioned fluid dynamic coupling existing between the exhaust hood casing and the diffuser, a parametric model has been developed including geometrical parameters of both components. Due to the increased number of parameters, the DOE has to take into account a simplification of the fluid domain was necessary to reduce the overall computational costs of the procedure. For this purpose, a periodic CFD model has been conceived to significantly reduce the number of grid elements, basically modeling as periodic the exhaust hood domain as illustrated in Figure 3.11. The introduction of such simplification allows to significantly reduce the computational costs respect to a 3D exhaust hood domain (illustrated in Figure 3.11a), even if specific boundary conditions are required to replicate the flow field of the 3D diffuser.

The idea behind the proposed approach is to approximate the flow in the diffuser as symmetric, neglecting, at first instance, the effects related

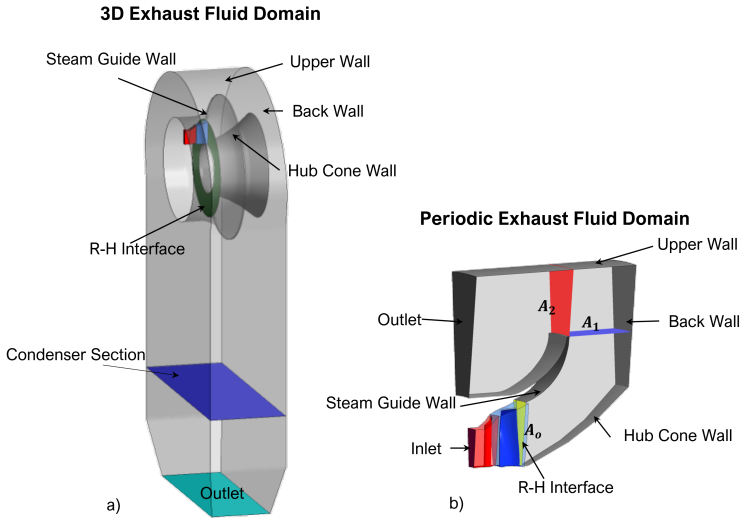

Figure 3.11: a) 3D exhaust hood numerical setup b) Periodic model exhaust hood numerical setup

to the asymmetry of the radial exhaust system casing. Similar approaches can be found in literature [67], however, the one presented in this work differs from others as it considers the presence of the exhaust hood upper wall to replicate the upper part of the 3D exhaust hood, where the most important aerodynamic flow features occur. In fact, as already found in the previous DOE investigation, the upper wall strongly affects the diffuser performance and, for this reason, it is crucial to replicate this effect also in the simplified model.

The achieved reduction of the computational cost allows realizing the very high number of simulations required for the presented design procedure. The computational cost of each simulation is 20 CPUh, 10 time lower respect to the double mixing plane approach with 3D exhaust hood. One of the key feature for the definition of this simplified model is the outlet condition. Three different outlet types have been tested as shown in Figure 3.12. By looking at the 3D baseline geometry flow field

the main flow features are the hub cone separation and the tip vortex in the region downstream of the diffuser. Among the boundary conditions available in CFX, the one able to replicate both this flow features is the Periodic Axial Out while the others alter the flow field predicted by the 3D model. Thus, the static pressure outlet has been imposed as boundary, since CFX automatically switches the boundary condition from "outlet" to "free-slip wall" in the cells with a back-flow, guaranteeing the formation of a flow field similar to the one observed in the 3D model. The pressure value has been adjusted to match the 3D model flow conditions, both in terms of total-pressure and axial velocity at the diffuser inlet. Periodic boundary conditions have been used in both the stator, rotor and diffuser.

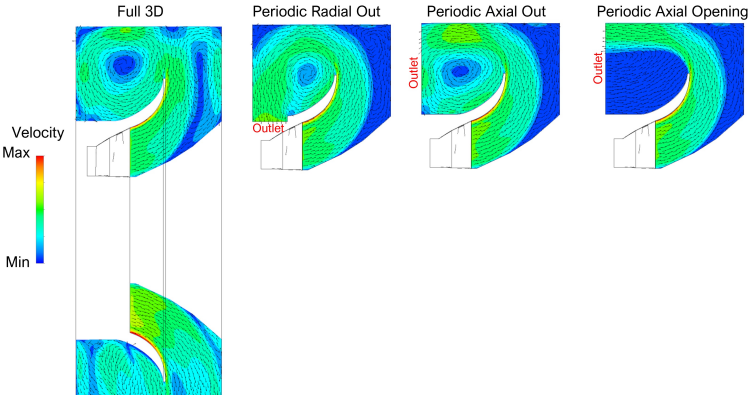

Figure 3.12: Velocity field comparison between 3D and different periodic models

With the aim of performing an automatic procedure, the definition of a smart convergence criterion is essential. In this regard, the convergence criterion used in the CFD simulation is based on a statistic monitor located in the diffuser inlet surface. Simulation convergence is achieved when the standard deviation of the static pressure calculated in the last 50 iterations is below 0.5 [Pa] and the residuals are lower than $1 * 10^{-5}$. These conditions have been imposed based on an initial sensitivity analysis.

3.2.2 Design of Experiment

After the definition of the simplified model, the next step was the realization of parametric geometry and the choice of the Design of Experiment input parameters presented in Figure 3.13.

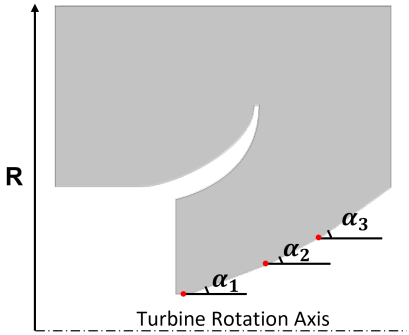

Figure 3.13: Input parameter of the optimization procedure

Based on the findings proposed by the literature review and on the previous investigation, four geometrical parameters (illustrated in Figure 3.13) have been selected to modify both the diffuser and outer casing geometry:

- α_1, α_2 and α_3, which are the angles of the hub cone wall. They directly influence the shape of the diffuser and the flow passage areas
- R, which is the radius of the cylinder forming the upper part of the exhaust hood. It is the same parameter investigated in the previous section where it has been shown how strong is the influence of this parameter on the diffuser performance.

These parameters will be presented as normalized quantities respect to the their variation range.

The geometry of the steam-guide wall (illustrated in the Figure 3.11) has not been changed since it has already been optimized in previous

investigations by Verstraete et al. [36, 39] on a similar exhaust hood and it has been confirmed as aerodynamically effective in the previous section exhaust hood baseline geometry analysis, indeed no separation area has been detected in this area. In the latter study, it has been also shown that the axial width of the baseline geometry is very close to the optimum one, the reason why it has been kept constant in this investigation. On the contrary, the hub cone wall has been identified as the most critical region of the exhaust system due to the presence of a wide separation area which drastically reduces the available passage area for the flow.

For these reasons, the optimization procedure, represented in Figure 3.14, has been carried out with the presented parameters to optimize the diffuser aerodynamic performance. Due to axial length constrain A_1 has been kept constant along with A_0, which is fixed by the rotor blade dimensions. Moreover, the axial position of the points illustrated in red in Figure 3.13 are fixed to reduce the parametric geometry degrees of freedom.

Concerning the DOE output variable, the pressure recovery factor calculated at the diffuser outlet section (A_1) and the exhaust system volume have been selected since this work aims to define an optimal exhaust hood as a trade-off between overall dimensions and the aerodynamic performances.

The Latin Hypercube Sampling [63] has been chosen as a sampling strategy to obtain a uniformly distributed data-set to avoid unwanted correlation in the input data that could affect the Design of Experiment analysis. The parameters variation range has been defined according to the geometric constraints provided by Baker Hughes.

3.2.3 Response Surface

The total number of geometry created in the DOE step is 50 and each of them has been tested with a CFD simulation, employing the numerical setup presented in Chapter 2 combined with the presented simplified fluid domain. Eight geometries have been removed by the procedure due to convergence issues. The others have been used to generate a first attempt

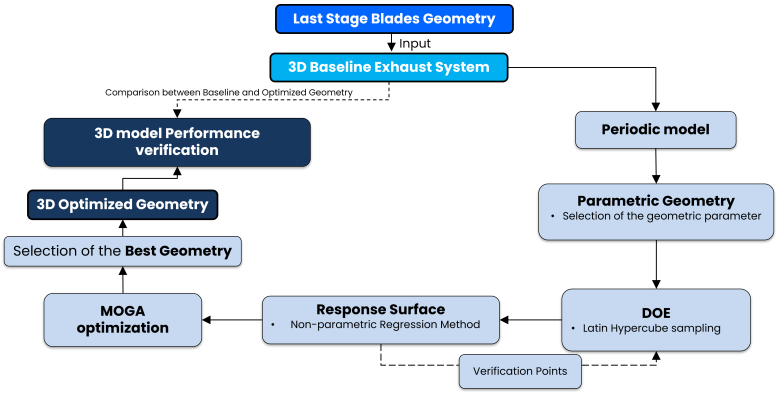

Figure 3.14: Input parameter of the optimization procedure

response surface with the non-parametric regression method available in Ansys Workbench, described in Chapter 1. The accuracy of the response surface is then tested with 4 additional geometries, defined as verification points, which are not used to generate the response surface but just to calculate the error (verification error) between the C_p predicted by the response surface and the C_p calculated by the CFD simulation. The idea behind this procedure is that, if the model can predict the C_p of these geometries, with an average error below 5% without using them for building the response surface, then a desired level of accuracy is reached and the response surface can be used by the optimization algorithm. On the contrary, if the verification error is above 5%, the verification points become refinement ones so they are integrated into a second attempting response surface. This iterative process has been repeated four times until good predictability of the response surface has been reached with 51 design points, excluding failed geometries.

Once completed the verification step, the response surface presents a coefficient of determination around 0.99 and a verification error of around 4%. Therefore, the model can predict with good accuracy the CFD pressure recovery in the final section of the diffuser. This is confirmed In Figure 3.15, where the C_p predicted by the response surface is plotted

against the one calculated by the CFD simulation. This comparison highlights how the model can predict the CFD results with a good level of accuracy: in fact, the response point trend line is very close to the graph bisector, meaning that there is almost a 1:1 match between the predicted and the calculated C_p.

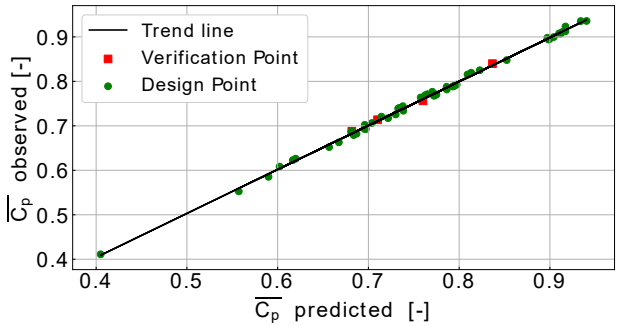

Figure 3.15: C_p predicted by the response surface plotted against the one calculated by the CFD simulation

Before presenting the optimized geometry, it is useful to discuss the influence of each parameter on the exhaust system performance. In this regard, the 2D slice representation of the response surface, reported in Figures 3.16, 3.17 and 3.18, is an effective tool for this evaluation. More to the point, Figure 3.16 is obtained by a 3D response surface, achieved for a fixed value α_2 and α_3, sliced with planes at constant R. The fixed values of α_2 and α_3 are coincident with the optimum ones. The same criterion is used to generate Figures 3.17 and 3.18. The description of the response surface results is focused on the most significant regions in terms of aerodynamic performance.

The strong influence of R on the exhaust hood performance, observable in the same figures, is consistent with the findings of the previous investigations found in literature [74, 75] and with the one reported in the previous section. Indeed, an increase of R usually leads to higher performance of the exhaust system. Concerning the influence of α_1, Figure 3.16

shows how an increase in α_1 leads to an improvement in the performance until a peak of the C_p is reached. A further rise in this angle results in a decline of the C_p. For a deeper understanding of this effect is useful to observe the sketch reported in Figure 3.14, where it is shown how an increase in α_1 leads to a decrease in the flow passage area.

From a fluid-dynamic point of view, this results in a slower deceleration of the flow and ideally in a reduced pressure recovery. But, contrary to what is expected, the response surface shows how an increase in α_1 has a positive impact on the C_p calculated in A_1. In fact, a weak deceleration in the first sections of the diffuser could prevent or postpone the separation, due to the higher momentum of the flow, with the related benefits in terms of aerodynamic performance. This effect will be further explained by looking at the velocity contours reported later. It is also important to underline how the response surface identifies that a further increase in α_1 beyond the peak of C_p leads to a decrease in the performance. By considering the aforementioned aspects, this is probably due to an exceedingly weak deceleration, or even a soft acceleration, of the flow that the final sections of the diffuser are not able to recover, since A_1 is fixed.

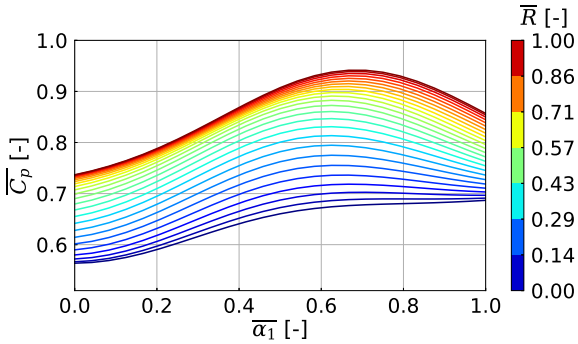

Figure 3.16: 2D slice of the response surface generated with a fixed value of α_2 and α_3.

The effect of α_2 is reported in Figure 3.17. For medium-high values of R the link between pressure recovery and α_2 is very similar to that one

presented for α_1: in fact, also in this case an increase in the performance is obtained by rising the angle until a peak is reached. The physical explanation behind this trend is the same reported for α_1.

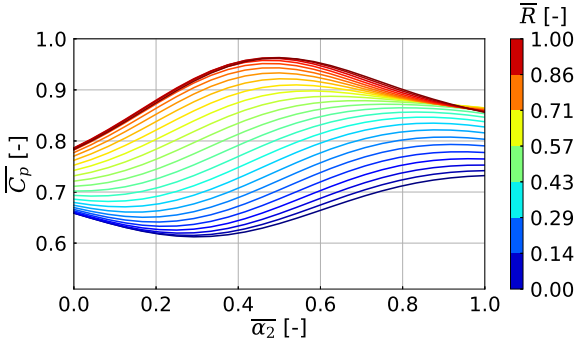

Figure 3.17: 2D slice of the response surface generated with a fixed value of α_1 and α_3.

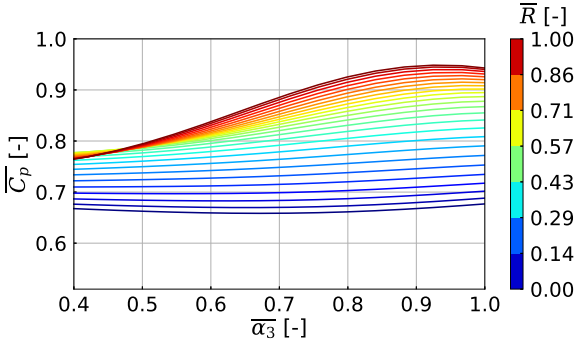

Figure 3.18: 2D slice of the response surface generated with a fixed value of α_1 and α_2.

Concerning the effect of α_3, illustrated in Figure 3.18, the response surface identifies, for high values of R, a monotonically increasing trend which means that, for an optimal aerodynamic behavior, α_3 should be

maximized. In fact, in this final region of the diffuser, the flow has already lost a substantial part of its initial velocity and it is, therefore, particularly inclined to separate; an increase in the flow passage area would just promote this trend. For medium-low values of R the influence of α_3 is almost zero, since it is very likely that the flow is already separated in this region and the geometric area does not coincide with the fluid-dynamic one, and, therefore, changes in the geometric area do not have an impact on the aerodynamic behavior of the flow.

To summarize, for a given diffuser area ratio, the response surface identifies regions having maximum pressure recovery performance for specific values of α_1, α_2, and α_3 that are related to the value of R and to the operating conditions as well, as will be shown in the Chapter 4.

3.2.4 Optimization

The response surface creation is followed by the multi-objective optimization, which uses the response surface, instead of CFD simulations, to find out the optimal geometry. The optimization algorithm used is Multi Objectives Genetic Algorithm, described in Chapter 1. The main objective of the MOGA is the maximization of C_p, while minimizing the exhaust hood volume as secondary target. The algorithm carries out 20 000 evaluations of the response surface to find out three optimal geometries and the most interesting one is then verified firstly with the simplified model and then with the 3D one. A comparison of the geometrical and performance data between the baseline geometry (Dp_0) and the optimized one (Dp_{opt}) is reported in Table 3.2. By observing this data, it is interesting to notice that the optimized geometry is obtained by increasing all the studied parameters, resulting in a significant improvement of the performance. In particular, the C_p increases by 30% with respect to the baseline geometry at the expense of an increase in the volume, which is however kept contained.

A comparison of the performance between the optimized and baseline geometry is reported in Figure 3.19b. In the same Figure the post-processing surfaces are shown, in which the C_p has been calculated with

Table 3.2: Input e output normalized data for the baseline and optimized geometry.

Dp	$\overline{\alpha_1}$[-]	$\overline{\alpha_2}$ [-]	$\overline{\alpha_3}$[-]	$\overline{R}$[-]	$\overline{C_{p,A1}}$[-]	$\frac{V-V_{Dp_0}}{V_{Dp_0}}$ [%]
Dp_0	0.43	0.38	0.22	0.45	0.69	0
Dp_{opt}	0.66	0.65	1	0.64	0.90	7.77

the Equation 1.1. As already mentioned in the previous subsection, the optimal geometry exhibits lower performance in the diffuser initial areas, largely offset by a stronger pressure recovery in the final ones.

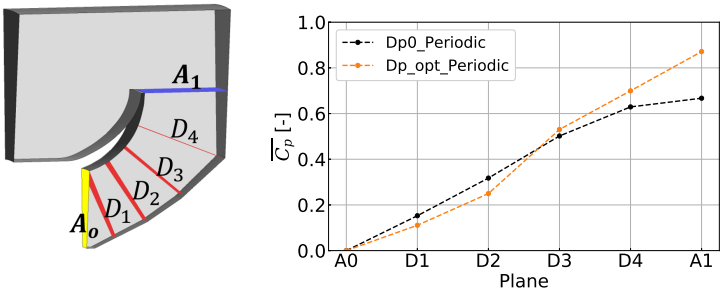

(a) *(b)*

Figure 3.19: a)Periodic model post processing surfaces b) C_p behaviour.

For a deeper understanding of the C_p behaviour, it is useful to observe the normalized absolute velocity contours reported in Figure 3.22. The baseline geometry flow field shows a wide separation area originating from the internal hub cone wall which drastically reduces the available passage area for the flow, therefore, acting as an aerodynamic blockage. This blockage opposes the flow deceleration causing the slope change in the C_p behavior. This effect is almost absent in the Dp_{opt}, and, therefore, it justifies the improvement in the performance shown in the Figure 3.19b.

3.2.5 Optimized Geometry Verification

The results presented up to this point have been obtained with a fluid model which considers the fluid as symmetric in the diffuser. However, since it represents an approximation of the real geometry, verification with a 3D model is required. The CFD simulations with the 3D domain have been carried out by employing the numerical setup presented in Chapter 2.

The 3D optimized geometry has been obtained by merging the periodic geometry replicated over 360° (blue area in Figure 3.20) and the diffuser-condenser junction (grey area in Figure 3.20), which is the same as the baseline geometry. For the way in which the upper region of the optimized exhaust system is generated, the misalignment between the axis of the cylinder that forms it and the turbine rotation axis, present in the baseline geometry, is lost. The latter allows obtaining a gradually increasing fluid area in the upper region of the exhaust hood, with a maximum in the horizontal plane and a minimum in the vertical one. As shown in the previous section, larger fluid areas moving towards the horizontal plane have a positive impact on the performance by mitigating the strength of the fluid vortices, which dominate the 3D flow field of the exhaust system.

By observing the graph in Figure 3.21, it can be seen how the periodic model (dashed lines) is able to replicate the C_p calculated in the diffuser in good agreement with the 3D model (continuous line) for both the baseline and the optimized geometry. This is an interesting finding for the current design procedure since the diffuser is the region in the exhaust system where the whole pressure recovery takes place. In fact, the downstream region, characterized by a geometrical asymmetry, acts as a junction between the latter and the condenser but it does not contribute to the pressure recovery and it is just a source of losses, as shown in the previous chapter. The optimization of the diffuser performance can therefore be realized with the simplified approach with a reasonable degree of approximation and a significant reduction of the numerical cost. Nevertheless, as a second step of the design procedure, it is necessary to properly design the exhaust system outer casing in the downstream

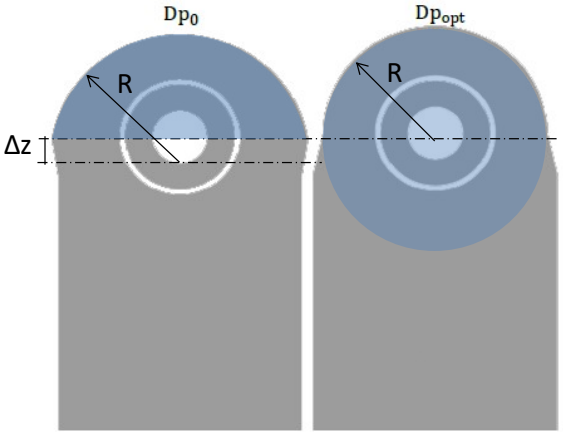

Figure 3.20: Frontal view of baseline and optimized geometry.

region to minimize the aerodynamic losses.

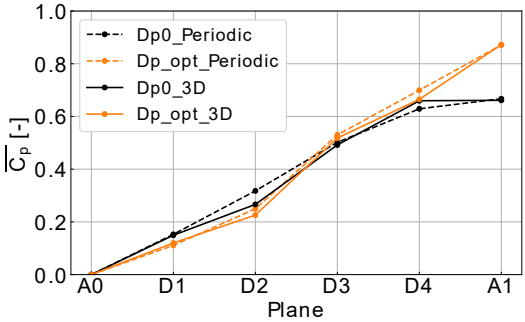

Figure 3.21: Comparison of the C_p trend between periodioc and 3D model for baseline and optimized geometry.

The flow fields of the Dp_0 and Dp_{opt} computed on the Y0 surface are presented in Figure 3.22. The disappearance of the hub cone separation is predicted by both periodic and 3D models and this justifies the im-

provement in the final sections of the diffuser observable in Figure 3.21. In addition, it is worth highlighting how the flow fields obtained with the periodic model are consistent with those obtained with the 3D ones.

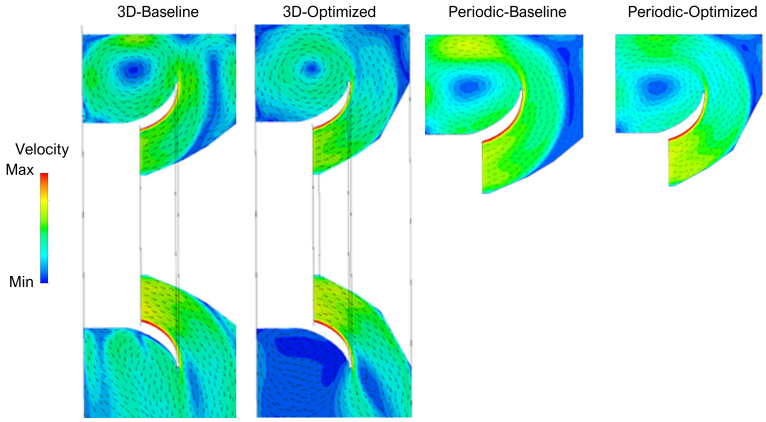

Figure 3.22: Velocity flow fields of both periodic and 3D model for baseline and optimized geometries.

The graph in Figure 3.23 presents a comparison between the C_p calculated for the baseline geometry (Dp_0) and the optimized geometry (Dp_{opt}) on the surfaces in red located along with the entire exhaust system up to the condenser section. The plot shows the strong increase in the performance obtained with the optimized 3D geometry with a volume even lower by 4% than to the baseline one, highlighting the strong improvement that the procedure represents in comparison to the previous one, in which an important improvement in the C_p value was reached by strongly rising the casing radius, generating an optimized exhaust hood with an increase in the volume of 17%.

Finally, by observing Table 3.2 it is worth noticing how α_1 and α_2 assume very close values in the optimized geometry (0.66 and 0.65), suggesting the use of only two angles for defining the diffuser hub cone geometry with reduced complexity and cost for the manufacturing.

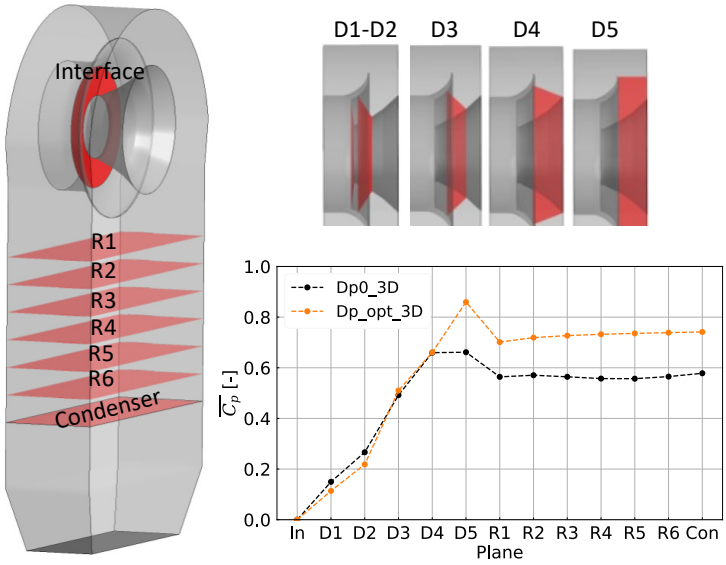

Figure 3.23: Comparison between baseline and optimized geometry of the C_P trend along the entire exhaust hood.

3.2.6 Concluding Remarks

The numerical procedure presented in this section can be used to optimize the performance of a steam turbine exhaust hood by acting on both diffuser shape parameters and exhaust hood maximum height. The comparison between the simplified and 3D models has shown the accuracy of the periodic model in replicating the flow field with the diffuser. The optimized geometry identified with the presented procedure presents a pressure recovery factor, calculated in the condenser section, 28% greater than the baseline one. The improvement of the performance is achieved even with a reduction of the exhaust system volume equal to 4%. However, by looking at the C_p trend reported in Figure 3.23 it can be understood how a further improvement of the performance can be reached by acting on the external casing of the exhaust hood and therefore limiting the drop of performance between D5 and R1. Indeed, as already mentioned

previously, the periodic model due to its inherent symmetry assumption can not act on the Δz parameter investigated in the previous section. However, it can be added to the optimized geometry by using the response surface presented in Figure 3.6.

In the light of the above, a third attempt optimized geometry has been generated by adding a Δz on the optimized geometry found in this section. This geometry is illustrated in Figure 3.24 together with the other geometries.

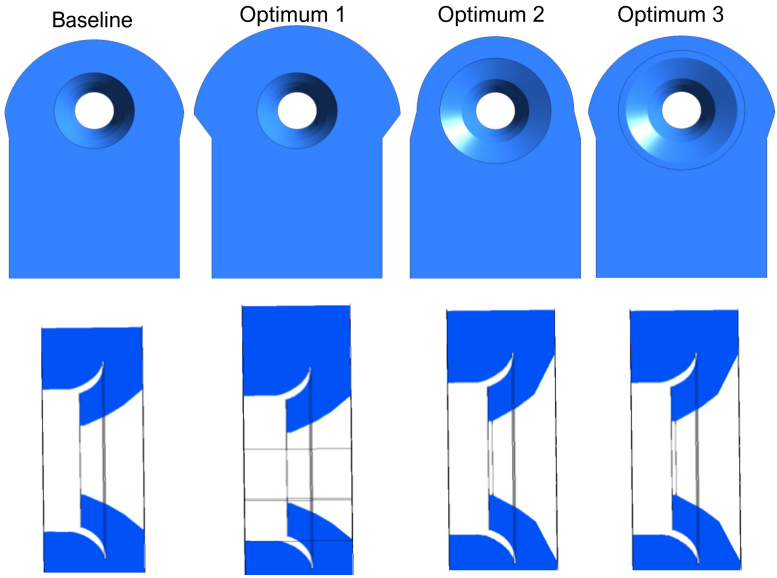

Figure 3.24: Comparison between baseline and different optimized geometry.

By observing Figure 3.24 it is clear how the first optimized geometry (Optimum 1) found in the previous section by acting in the external casing only presents very high volume with respect to the others. The non-optimal fluid behavior in the diffuser is indeed compensated with a significant increase of the exhaust volume in the upper region to reduce

the vortices strength which ensures an increase of C_p of 24% respect to the baseline.

The second attempt optimized geometry (Optimum 2) presents a volume significantly reduced respect to the first one, even lower respect to the baseline, with an increase of C_p of 28% obtained by optimizing both the diffuser hub cone shape and the exhaust hood maximum height. However, the simplified procedure neglects the Δz generating more losses downstream of the diffuser, as shown in Figure 3.25 between the surfaces D5-R1 where the Optimum 2 presents the highest C_p drop. This can be solved by acting on the Δz as shown by the Optimum 3 geometry, generated starting from the optimum 2 and adding a Δz with the results of the response surface presented in Figure 3.6. The Optimum 3 presents indeed optimum performance in both diffuser and condenser neck.

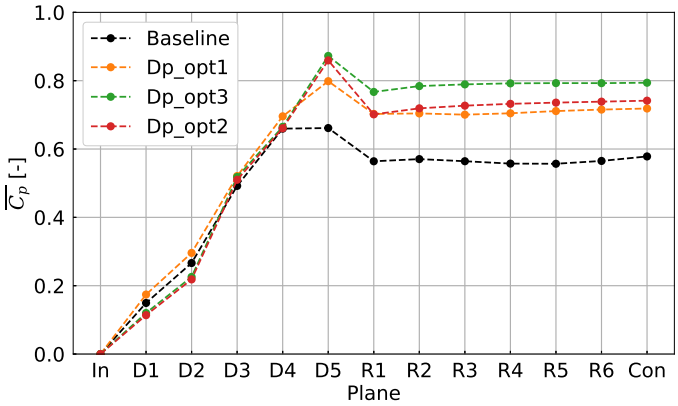

Figure 3.25: Comparison between baseline and different optimized geometry.

Chapter 4

Off-Design Assessment

In this chapter different aspects related to the aerodynamic behavior of the exhaust system during off-design conditions are investigated. In the first part the influence of the swirl number at the diffuser inlet on the performance is assessed, since it is a key parameter to describe the different operations of the machine. In design operating condition the LSB is designed to operate with an outlet swirl number near to zero, while by reducing (or increasing) the mass flow this parameter takes values different from zero. The tangential inclination of the flow at the diffuser inlet drastically affects the performance of the exhaust hood, especially when it interacts with the structural struts.

In the second part of the chapter the focus is moved on the influence of the operating conditions on the exhaust system design approach proposed in Chapter 3. In this regard, has been demonstrated how the optimum geometry depends on the operating condition considered.

Finally, in the concluding part of the Chapter the fluid dynamic mechanisms potentially accountable for flow-induced vibration of the LSB during Low Volume Fluid conditions are investigated in both axial and radial exhaust hood configurations.

4.1 Influence of diffuser inlet swirl

In the light of the findings proposed by the literature review, the central role of the inlet swirl on the exhaust system performance seems clear. It is therefore crucial, once defined the exhaust hood geometry to test its performance at different inlet swirl angles. In this section, the pressure recovery performances of the axial exhaust hood presented in Chapter 2 are evaluated as a function of this parameter. The performances of a periodic model without struts are compared with the ones obtained with a 3D exhaust hood, with struts included, by using the numerical setups already presented in Chapter 2. The results of this analysis are presented in Figure 4.1 with normalized C_p and Swirl Angle. The negative swirl angle operating points have been obtained by increasing the outlet pressure and consequently decreasing the mass flow, or by decreasing the inlet pressure at the last stage stator. The positive swirl angle has been instead obtained with an opposite criterion.

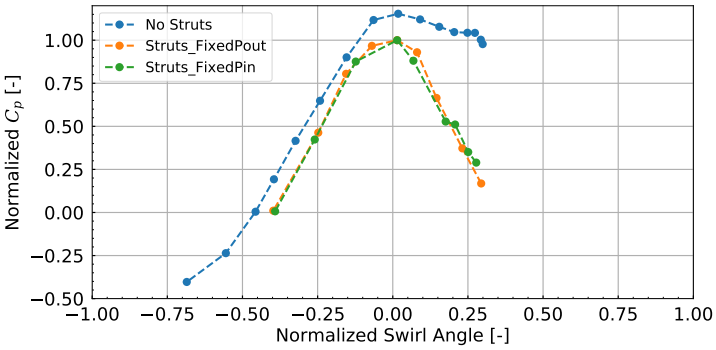

Figure 4.1: Influence of inlet swirl angle on diffuser performance with and without the exhaust hood struts.

By looking at Figure 4.1 the strong impact of the swirl number on the performance is visible, and its effect is strongly emphasized when the

struts are integrated in the fluid domain. As expected, the maximum performances of the exhaust hood, for both the fluid models considered, are obtained in correspondence of swirl number near zero. It is worth mentioning the different trends identified by the fluid models for positive values of swirl, such operating points are characterized by high axial (higher mass flow respect to the design) and tangential velocity. The physical explanation behind this trend is explained later in this chapter with additional post-processing.

In order to assess the influence of Swirl Angle, the performance parameter behaviors along the exhaust hood of two operating points with opposite Swirl Angle (reported in Table 4.1) are compared with the design one in Figure 4.2. The curves reported in this figure have been obtained with the 3D model and therefore can be seen the effect of the interaction between the swirl of the flow and the struts. In the initial part of the diffuser, no differences between the operating points can be seen, while a significant change of the performance parameter trends is visible in the struts region. The interaction between swirl and struts leads to a drastic drop in performance due to a significant increase in losses. It is useful to distinguish between the positive and negative swirl conditions in order to properly understand the two mechanisms responsible for the drop in performance.

In the positive Swirl Angle condition, the drastic drop of performance is due to both an increase of losses and residual kinetic energy of the flow. Figure 4.3 clarifies how both these effects are due to the interaction between swirl and struts since the periodic model does not identify these effects. The mentioned performance parameter trends can also be seen in the negative Swirl Angle condition in Figure 4.4, however, the effects are significantly weaker. It is, therefore, possible to conclude that the high velocity magnitude characteristic of the positive swirl condition determines a further decrease of performances.

In order to understand these effects is useful to observe the velocity contours reported in Figure 4.5 and 4.6. Specifically, by looking at Figure 4.6 it can be seen how the interaction between the swirl of the flow

and the struts promotes the onset of zero-velocity recirculation regions which reduce the available flow passage area. The increase of the residual kinetic energy is therefore linked to the local flow acceleration due to the reduction of the fluid dynamic area, this effect is surely stronger in the high-velocity cases (positive swirl angle). This justifies the diversification on the residual kinetic energy trend in Figure 4.2.

The separation area also affects the increase of losses identified in Figure 4.2, indeed, the high velocity gradient between the recirculation region and the high-velocity flow in the free stream leads to significant losses, which are stronger in the high-velocity operating points. These effects are canceled in the no struts fluid domain leading to the different trends of performance parameter observable in Figures 4.3 and 4.4.

However, the chart reported in Figure 4.1 highlights a drop of performance for negative Swirl Angle also in the periodic model. This effect can not be related to the struts. The explanation behind this trend can be understood by looking at the velocity contour 4.5 where a hub separation is clear for the negative Swirl Angle operating points. Such a separation is not linked to the struts but to the low momentum of the flow in the boundary layer due to low velocity characteristic of these off-design operating points. The mechanism which leads to the drop in performance is the same one already explained with the hub cone separation of the radial exhaust hood in Chapter 3. This effect is not detectable in the positive Swirl Angle operating points, as visible in Figure 4.5, since they are characterized by higher momentum of the flow in the boundary layer avoiding the flow separation. This is the reason why the periodic model does not identify any drop in performance in these operating points.

Table 4.1: Operating pints with different inlet Swirl Angle

OP	$\overline{\theta}$[-]	$\overline{U_{\mathrm{ax}}}$[-]	$\overline{p_{\mathrm{out}}}$[-]
Design	0	1	1
Positive Swirl	+0.15	1.1	0.88
Negative Swirl	-0.15	0.9	1.11

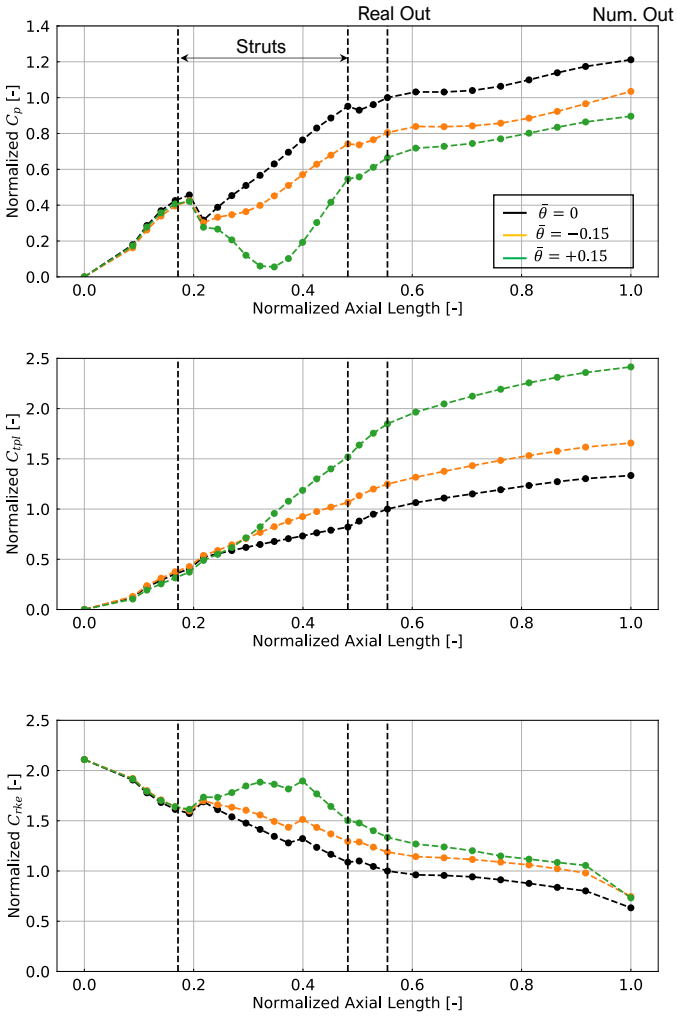

Figure 4.2: Effect of inlet swirl on performance parameter trends of 3D exhaust hood model with struts included.

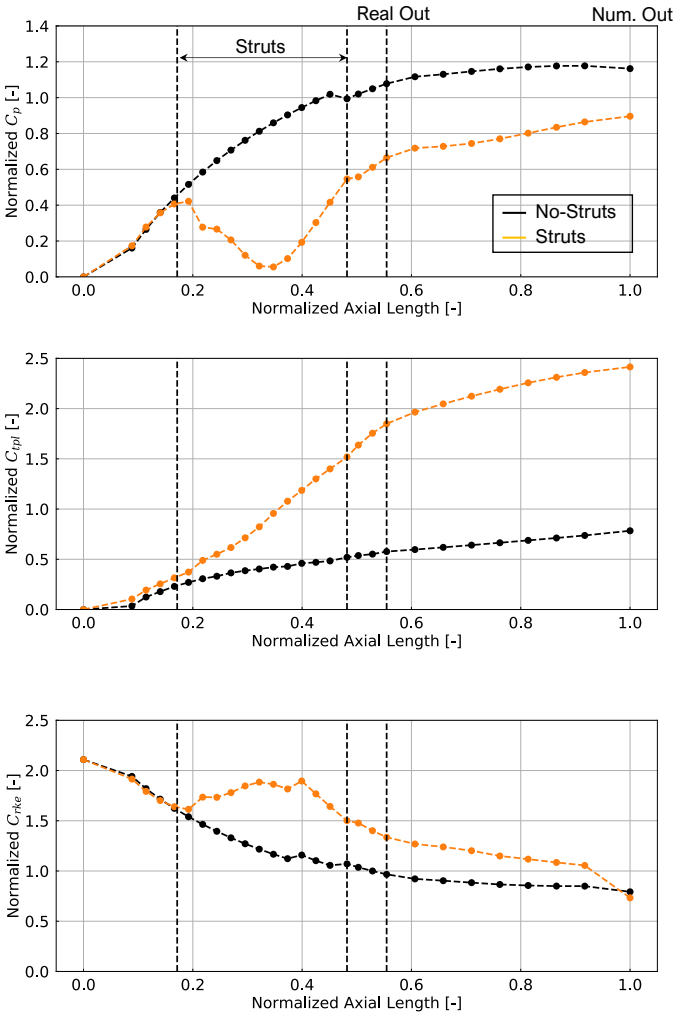

Figure 4.3: effect of struts on performance parameter trends for a fixed θ=+0.15.

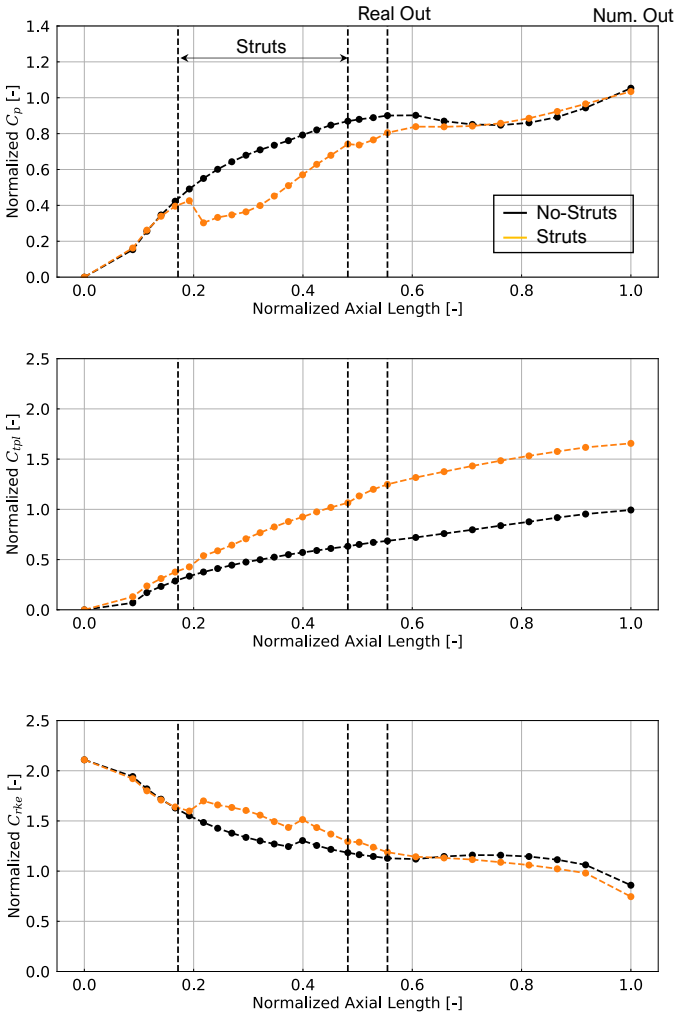

Figure 4.4: effect of struts on performance parameter trends for a fixed θ=-0.15.

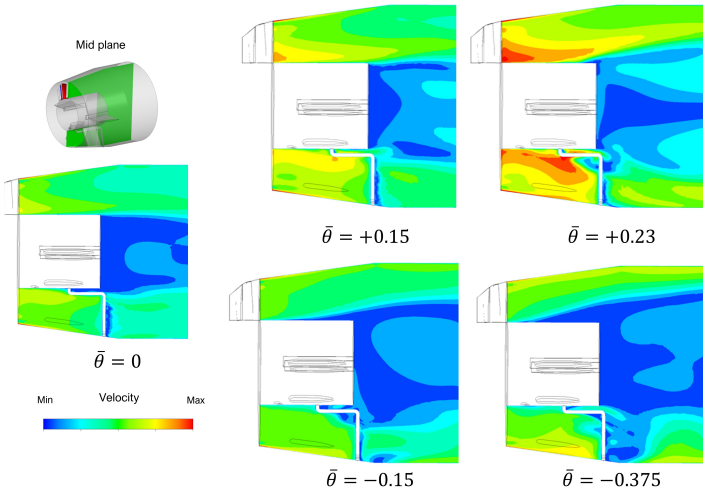

Figure 4.5: Influence of inlet swirl on the exhaust system flow field.

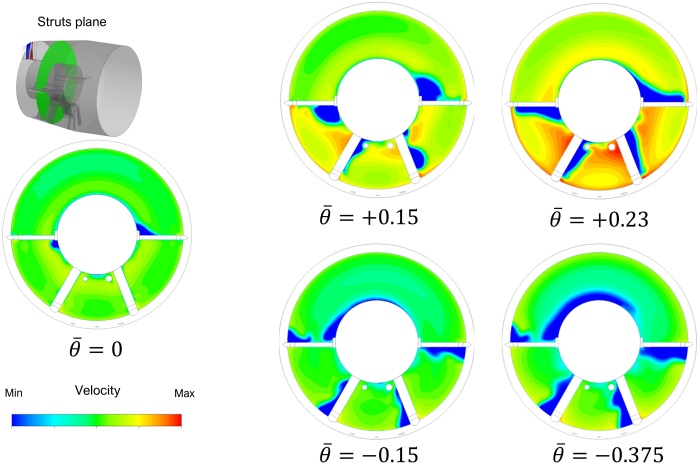

Figure 4.6: Influence of inlet swirl on the exhaust system flow field.

4.2 Optimization approach in off-design conditions

For a given exhaust hood geometry, the influence of different operating conditions on exhaust system performance has been assessed in the previous section with an axial exhaust hood configuration. The focus of this section is instead on the impact of such off-design conditions on the input geometric values of the optimum geometry found with the design approach proposed in Chapter 3. Before presenting the results of this analysis, it is interesting to investigate how the optimum geometry (the Optimum 2 in Figure 3.24) found in Chapter 3 reacts to different operating conditions. This analysis further expands the findings proposed in the previous section by considering also a radial exhaust configuration.

The results of this analysis are illustrated in Table 4.2 where C_p of the Dp_0 and Dp_{opt} calculated in design and off-design operating conditions are reported. By observing this table, it is interesting to highlight how the optimized geometry performs better than the baseline one also at off-design conditions. The results confirm the findings proposed in the previous section, it can be concluded that a high velocity operating condition (and high Swirl Angle) improves the performance by energizing the flow in the boundary layer in the internal side of the diffuser, contrasting or avoiding the separation in this region; a decrease in velocity leads to an opposite effect with the onset of the Hub Cone Separation Vortex. It's important to underline how other studies [39] identify a drop in performance if the velocity is further increased respect to the values simulated in this case.

Table 4.2: C_p of the Dp_0 and Dp_{opt} calculated in A1 in different operating conditions.

OP	$\overline{P_{out}}$ [-]	$\overline{U_{ax}}$ [-]	$\overline{C_{p,Dp0}}$[-]	$\overline{C_{p,Dp_{opt}}}$[-]
OP1	0.82	1.24	0.75	0.98
OP2 (Design)	1	1	0.69	0.90
OP3	1.08	0.77	0.40	0.52
OP4	1.17	0.72	0.27	0.37

In order to gain more in-depth knowledge about the impact of the off-design conditions on the exhaust system design, the developed optimization approach, reported in Chapter 3, has been applied to the other operating points (see Table 4.2). The goal of this investigation is to find out an optimal geometry for each operating condition, comparing such geometries to the Dp_{opt} generated at design condition (OP2). It is worth mentioning how the off-design conditions analyzed are still far from the LVF (axial velocity at diffuser inlet below 50% of the design one), since in such conditions the pressure recovery is no longer of interest. The off-design conditions presented in this investigation are close to the design where the exhaust hood performances are still of primary importance.

The influence of the input parameters on the diffuser performance for different operating conditions is presented in Figure 4.7. The results obtained with the OP3 are not shown in this Figure since they are similar to the ones obtained with the OP4. The curves illustrated in Figure 4.7 show the effect of each parameter on the C_p and they have been generated by fixing the other three parameters in the optimal values. Each line represents the effect on the C_p of a specific parameter within its variation range, reported in the abscissa axis. The black squares show the optimum value of each curve.

The strong influence of the operating conditions on the C_p is clear by observing Figure 4.7. Concerning α_1, it is interesting to highlight how its impact is strongly related to the operating conditions. In particular, by increasing the axial velocity (OP1) the peak of the C_p is shifted towards lower α_1 values, meaning that a higher deceleration is allowed still avoiding the separation. This effect is consistent with what was expected since the flow in the boundary layer has already been energized by the growth of the inlet axial velocity and the area can, therefore, be increased abruptly without separation. By decreasing the axial velocity (OP4), the influence of α_1 is totally different: in fact, as can be seen, the curve presents a constantly increasing trend and the optimal value is close to the upper limit of the variation range. Also, this trend is in a line with the expectation since the flow in the boundary layer is more prone to

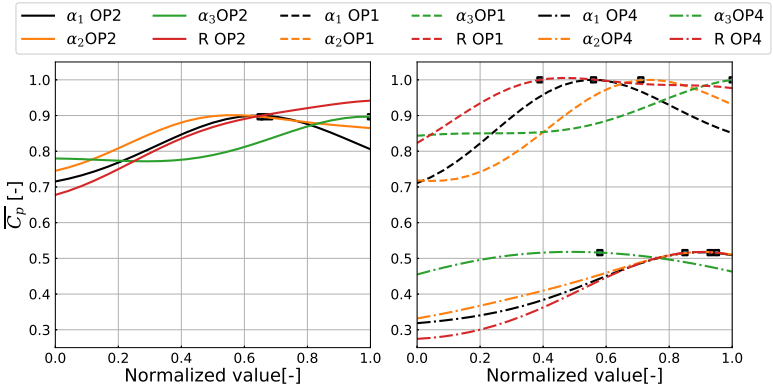

Figure 4.7: Influence of input parameters on diffuser performance at different operating conditions.

separation, due to the reduction of the inlet axial velocity, and a more gradual increase in area is required to avoid it.

Moreover, at off-design conditions, the response surface identifies an impact of α_2 similar to α_1, according to the already presented results of the design investigation. As a matter of fact, α_2 optimum in the OP4 case is shifted towards a higher value due to the effect already mentioned for α_1.

By considering the off-design operating conditions, α_3 is confirmed as the least impacting parameter. In particular, in the OP4 where a very weak influence on C_p is observed in Figure 4.7. This effect can be explained by considering that, at reduced axial velocity, this region is probably dominated by a separation area and changes in the geometric area do not have an impact on the aerodynamic behavior of the flow.

Finally, the exhaust hood maximum height, defined by R, is considered as the most important parameter for the exhaust system performance in the design condition. However, its impact is reduced in the maximum axial velocity condition (OP1): in fact, in this case, the constantly growing trend of the C_p with the increase in R, that has been already identified

in the OP2, is lost since the curve remains constant also after the peak is reached. This allows picking a reduced optimal value of R as shown also by Figure 4.8 with a significant reduction of the exhaust system volume (-13%).

In reference to the OP4, the response surface identifies a strong impact of R, even greater than in the OP2. Due to the greater slope of the R curve, the optimization algorithm shifts the optimal value of R at a higher value with respect to the design condition with a considerable increase of volume (+17%).

The trend of the optimal values in the different operating conditions are presented in Figure 4.8 and summarized in Table 4.3.

Table 4.3: Optimal geometries in different operating conditions.

OP	$\overline{\alpha_1}$[-]	$\overline{\alpha_2}$ [-]	$\overline{\alpha_3}$[-]	$\overline{R}$[-]	$\overline{C_{p,A1}}$[-]	$\frac{V-V_{Dp_0}}{V_{Dp_0}}$ [%]
OP1	0.56	0.71	1.00	0.39	0.99	-7.1%
OP2	0.66	0.65	1.00	0.64	0.90	+7.8%
OP3	0.84	0.79	0.95	0.81	0.64	+12.1%
OP4	0.93	0.95	0.58	0.85	0.51	+26.2%

As shown in Figure 4.7 it is noteworthy that, despite the procedure optimizing the investigated parameters to face a reduction of the inlet axial velocity, the static pressure recovery is far below with respect to design condition, meaning that a reduction in the C_p is inevitable at low-speed conditions.

By comparing the Tables 4.2 and 4.3, it can be noticed that the values of the C_p obtained by optimizing the geometry in each operating point (see Table 4.3) are comparable to the ones obtained by testing the Dp_{opt} in off-design conditions (see Table 4.2). For this reason, it can be concluded that, within the range of variation of the parameters here investigated, the optimization procedure should be applied to the design operating condition only. In other words, the complexity of considering an optimization approach that takes into account also different operating conditions to

select the optimum geometry is not justified by evidence of significant improvement in the performance respect to an optimization approach carried out on fixed operating conditions. In addition, presumably, the design operating point is the one in which the turbine operates for a longer time and consequently the one in which high performances are of higher importance, consequently, unless of a pioneering design of a variable geometry, the optimum geometric parameters should be selected in design operating point.

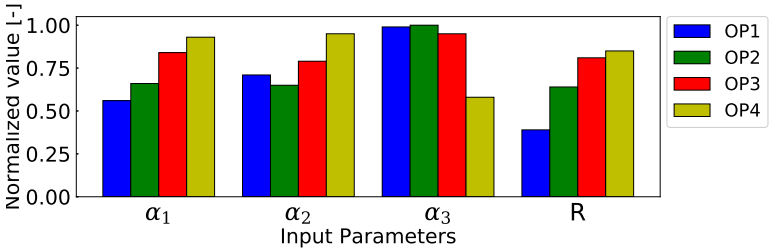

Figure 4.8: Optimal input parameter in different operating conditions.

4.3 Low Volume Flow Condition Analysis

The off-design operating conditions studied in the previous sections can not be considered as Low Volume Flow conditions since the values of axial velocity at diffuser outlet are above 50% of the design value. This chapter is instead focused on the LVF conditions where the performances of the exhaust hood are not of interest since the last stage is extracting power from the shaft (ventilation). These operating conditions are of extreme interest in this research topic due to the greater flexibility required in a modern steam turbine which is linked to even increasing LVF conditions. As widely reported in the literature review proposed in Chapter 1, during these operations the flow field could trigger dangerous non-synchronous aerodynamic excitations of the last stage bucket (LSB). In order to discover the source of such excitations, an extensive numerical study has been

carried out to investigate different mechanisms potentially accountable for flow-induced vibrations. In the first part of the section, the radial exhaust hood designed with the optimization approach proposed in Chapter 3 has been investigated in strong off-design conditions with unsteady simulations in order to detect rotating instability phenomena that might arise in the last stage during LVF conditions. The second part of the section is instead focused on determining the same phenomena in an axial exhaust hood. Such aerodynamic instabilities are detected by performing 3D unsteady CFD simulations (URANS) of the low-pressure turbine the last stage coupled with the axial exhaust hood, with structural struts included.

4.3.1 Radial Exhaust Hood

The optimization approach proposed in this work allows to find out a high-performing exhaust hood geometry for a given set of design constraints. A further fundamental step to complete the design process is the analysis of such geometry in all the operating ranges of the machine with a specific focus on the most dangerous ones in terms of structural stability, as schematically shown in Figure 4.9. This analysis is essential to define the operation limits of the turbine avoiding the operating conditions which may trigger LSB vibration. In this sub-section, a generic description of the instabilities found during LVF conditions is presented, while a more in-depth characterization of this phenomenon is reported in the following sub-section where an advanced post-processing technique has been used to extract a graphical representation of these instabilities.

As the first step of the off-design assessment, the periodic simplified model presented in Chapter 3 has been used to study the evolution of the flow field from the design to the LVF conditions. The output of this step is the selection of the most significant operating condition to be simulated with the 3D setup. In order to select such condition the LSB performance parameters are monitored to identify the ventilation of the last stage and the compressor mode operation at the rotor blade tip.

The different operating conditions have been obtained by varying the outlet pressure as illustrated in Figure 4.10a where the outlet pressure is

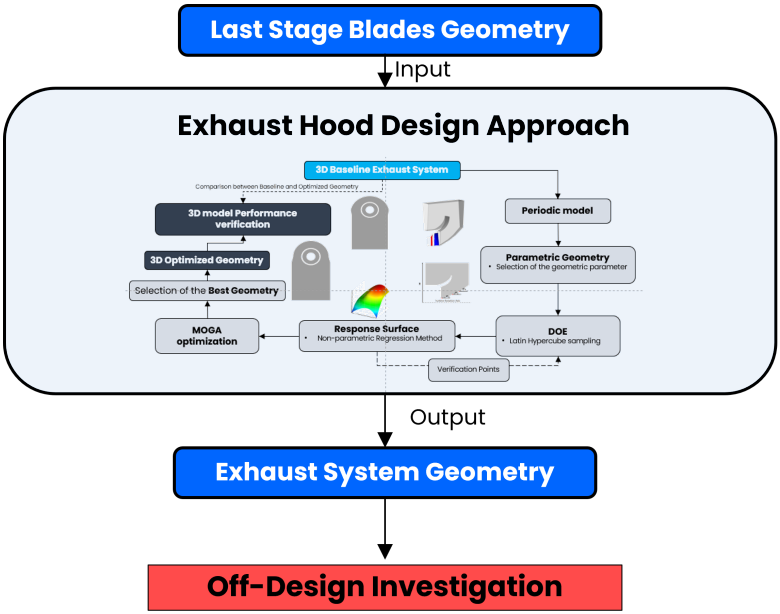

Figure 4.9: Scheme of workflow for the exhaust hood design.

plotted against the flow coefficient at the diffuser inlet. The latter has been selected as a key parameter to investigate the off-design conditions by virtue of the findings proposed in the literature review. It is calculated as the ratio between the axial diffuser inlet axial velocity and the blade tangential velocity at the medium radius. The low computational cost of the periodic model has allowed simulating 28 operating points in an acceptable with steady-state simulation. Indeed, several investigations have shown the applicability of RANS simulation to capture the characteristic flow features during LVF conditions [92, 93] reason why this setup has been used to study the evolution of the flow field as a consequence of the reduction of the mass flow.

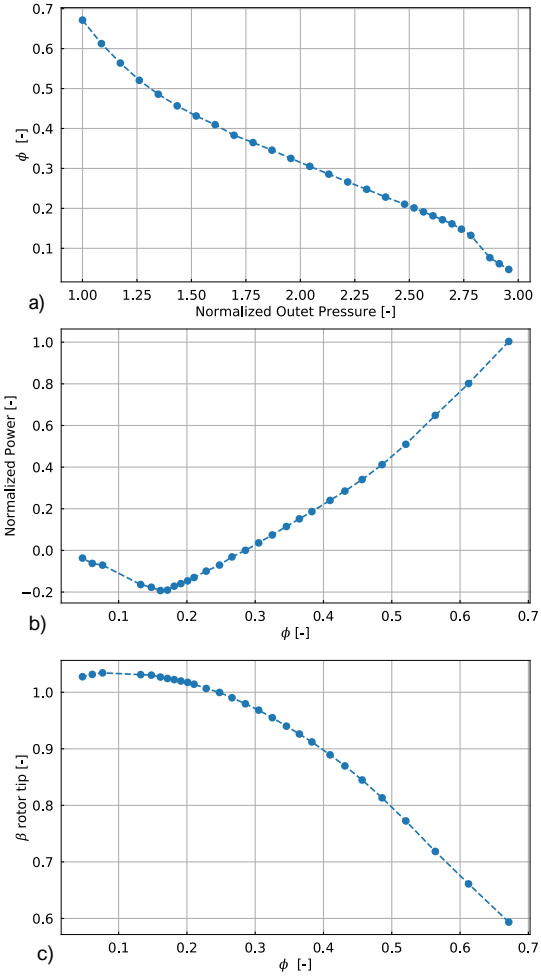

Figure 4.10: a)Effect of outlet pressure on flow coefficient b)LSB power in off-design conditions c)Rotor tip pressure ratio in off-design operating conditions.

By looking at the Figures 4.10 b and c it can be seen how for ϕ below 0.25 the last stage extracts power from the shaft and the rotor tip acts as a compressor. According to the findings of the literature review, the latter seems a necessary condition for the onset of the rotating instability. The evolution of the flow field associated with the LVF conditions can be seen in Figure 4.11. By looking at this figure it is clear how from design condition to the LVF one the flow field experiences a radical change. As already presented in the previous section the reduction of the axial velocity leads to flow separation in the hub region of the diffuser and the flow in the LSB becomes strongly radial, as shown by the velocity streamlines for the ϕ=0.228 condition. By further reducing the axial velocity (ϕ=0.132) the Tip Torus Vortex appears in the region between stator and rotor and, as will be demonstrated later, it is responsible for pressure oscillation which may trigger LSB vibration. Finally, in the minimum axial velocity condition (ϕ=0.076) both the Tip Vortex and the Hub Separation increase in intensity.

Among the operating points simulated with steady-state numerical setup, 3 points have been selected to perform URANS simulations with the simplified numerical domain. The design operating point has been selected as a reference point, the others are the operating point just inside the ventilation region of the LSB ($\phi = 0.23$) and the operating point with maximum pressure rise across the blade tip ($\phi = 0.18$). The URANS simulations with the simplified model have been carried out with the Transient Blade Row Method, available in CFX, which significantly reduces the computational effort of a transient simulation by allowing to simulate a single blade passage of the last stage. Among the different models in CFX Transient Blade Row, the Time Transformation method has been used. Such a method, based on phase-shifted periodic boundaries, handles the problem of the unequal pitch of stator and rotor by transforming the time coordinates of the rotor and stator in the circumferential direction in order to make the models fully periodic in "transformed" time.

The definition of the post-processing surfaces and monitor points is an essential step to detect the flow instabilities. These are illustrated

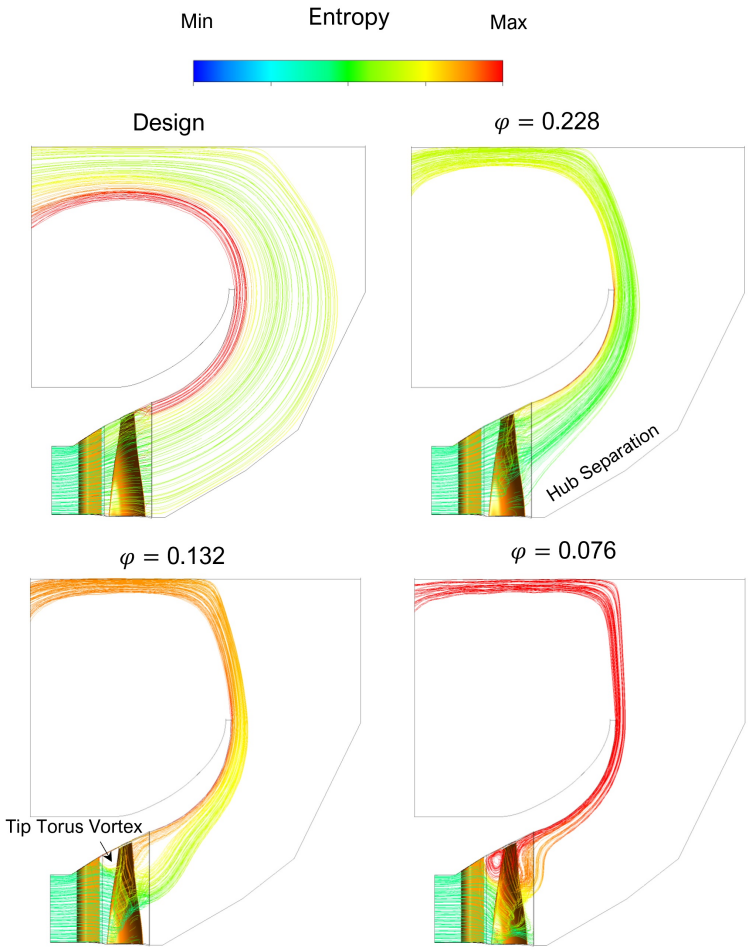

Figure 4.11: Evolution of the exhaust system flow field in off-design operating conditions.

in Figure 4.12 for both the periodic and 3D models. Concerning the periodic model (Figure 4.12 a), 12 monitor points have been used to

record the pressure oscillations and consequently to detect unsteady phenomena. These monitor points are located in 3 different regions, in stator-rotor inter-space, indicated in Figure with R1, in the rotor-diffuser space, indicated in Figure with R2 and finally in the diffuser. in both the R1 and R2 surface the monitor points are located at 3 different spanwise locations: 20, 50 and 85% of blade span. The monitor points used for the 3D model follow the same criterion with the further extension in the circumferential direction, as shown in Figure 4.12c.

Concerning the nomenclature of the monitor points used in the 3D model, the first code (i.e. "SL11") indicates the streamwise location of the post-processing surfaces, which are illustrated in Figure 4.16, the second code shows the spanwise location (i.e. "SPA85" means 85% of the span) and finally, the last number indicates the circumferential location of the monitor point (i.e. "0" means theta=0, that is coincident with y-axis).

The pressure signals recorded with the presented monitor points have been post-processed with the FFT to identify the different sources of instabilities and the results are presented in Figure 4.13. Specifically, in Figure 4.13a the FFT spectra of the pressure signal at the tip of R1 surface is reported for the 3 operating points simulated with the periodic model. By looking at this figure it is clear how in the operating point with $\phi = 0.18$ significant pressure oscillations arise in the low-frequency region. Such oscillations are generated by two different sources, the first ones are the Low Engine Order Frequencies which are explained in detail in the next sub-section, while the second is the Rotating Instability (RIF) well documented in the literature review. The oscillations generated by these instabilities are significantly stronger than the one associated with the Blade Passing Frequency (BPF), which are well discernible for the design operating condition since they are proportional to the mass flow rate. By comparing the charts in Figure 4.13 it seems clear how the RI is almost absent in the mid and hub section, contrary to the LOEF which are distributed over the entire span. Concerning the operating point with $\phi = 0.23$ no RI has been detected, this confirms that the ventilation of the last stage is not a sufficient condition for the onset of this phenomenon.

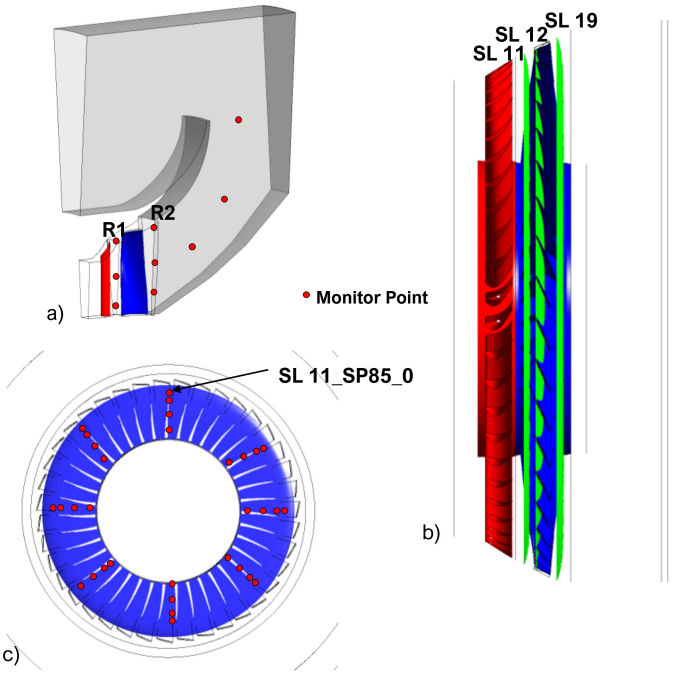

Figure 4.12: Post-Processing surfaces: a) Periodic model monitor points b) 3D model post-processing surfaces c) 3D model monitor points

The same conclusion can be obtained by looking at the flow field reported in Figure 4.11 where for $\phi = 0.23$ no Tip vortex is shown further justifying the applicability of RANS simulation for a qualitative analysis of the most critical conditions.

In Figure 4.14 the FFT spectra of the monitor points located in the R2 surface are presented. The RI is not clear anymore since it is located in the region upstream respect to these monitor points while the LEO disturbances are still present. Indeed, as will be clarified later these instabilities are generated in the region between rotor and diffuser where the R2 surface is located.

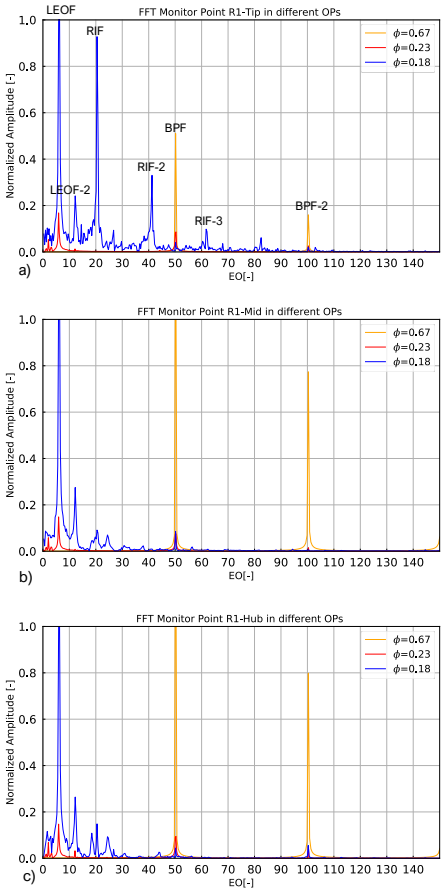

Figure 4.13: a)FFT spectra of pressure signal computed on relative monitor point at the tip of R1 surface in different operating conditions b)FFT spectra of pressure signal computed on relative monitor point at the mid of R1 surface in different operating conditions c)FFT spectra of pressure signal computed on relative monitor point at the hub of R1 surface in different operating conditions.

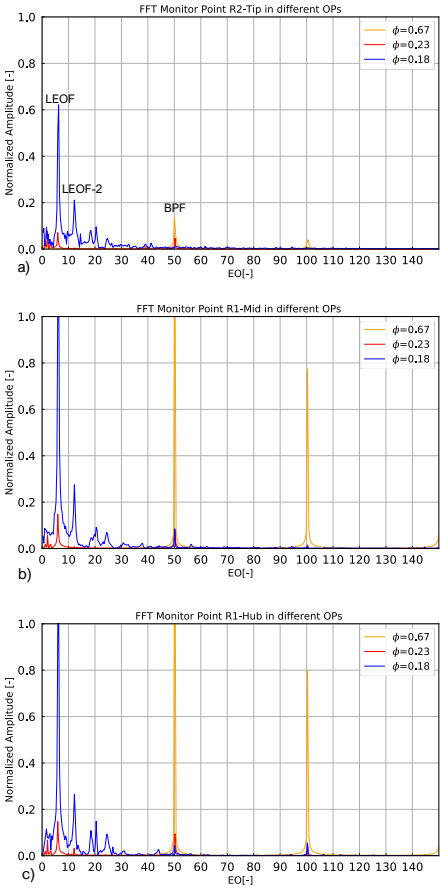

Figure 4.14: a)FFT spectra of pressure signal computed on relative monitor point at the tip of R2 surface in different operating conditions b)FFT spectra of pressure signal computed on relative monitor point at the mid of R2 surface in different operating conditions c)FFT spectra of pressure signal computed on relative monitor point at the hub of R2 surface in different operating conditions.

It is worth mentioning how, in line with the findings proposed by the literature review, the periodic unsteady numerical setup is capable to detect the RI phenomena, despite the strong assumption of axial symmetry of the fluid domain. It is now of primary interest to assess the comparison with a full 3D unsteady setup in order to highlight the differences due to axial symmetric assumption. For this purpose, the operating points characterized by maximum pressure oscillations have been simulated with the 3D optimized exhaust geometry illustrated in Chapter 3 and the full annulus mesh of the last stage. The presence of RI is confirmed only with this numerical setup, the results of this analysis are reported in Figure 4.15 in terms of FFT spectra of the pressure signal. By comparing the periodic and 3D results is interesting mentioning how the presence of a real geometry exhaust system leads to a shift of the characteristic frequency of the RI and a significant reduction of the amplitude of the pressure oscillations. This means that the simplified model can be used to qualitatively identify the most dangerous conditions in terms of unsteady disturbances but not for quantitative characterization of the frequency of the phenomenon. With the 3D model, the RI is characterized by different peaks concentrated in a region of disturbances, while in the periodic model prediction the RI manifests itself as a single strong peak. The physical explanation behind the trend identified by the 3D model will be explained in the next subsection thanks to POD analysis.

Concerning the axial and span distribution of the instabilities the results obtained with the 3D model (in Figures 4.15a and b) are in line with the ones already observed for the periodic model. Finally, the circumferential distribution reported in Figure 4.15c shows how the RI is uniformly distributed over 360° degrees.

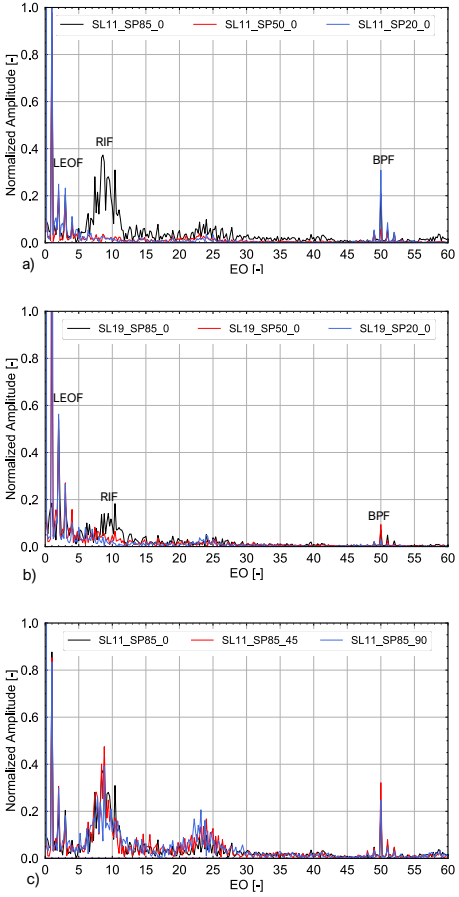

Figure 4.15: a) FFT spectra of pressure signal computed on relative monitor point at SL11 surface at different spanwise location b) FFT spectra of pressure signal computed on relative monitor point at SL19 surface at different spanwise location c)FFT spectra of pressure signal computed on relative monitor point at 85% span of SL11 surface at different circumferential location

4.3.2 Axial Exhaust Hood

This sub-section is focused on aerodynamic instabilities in the axial exhaust system which operates under LVF conditions. As already discussed in the previous sub-section such instabilities have been detected by carrying out unsteady simulations on a full annulus the last stage coupled with a real geometry axial diffuser of a steam turbine manufactured by Baker Hughes for Concentrated Solar Power (CSP) system applications.

To the author's knowledge, in literature, there is a lack of investigations concerning axial exhaust systems during LVF conditions and this is the first time that they are investigated with unsteady simulations. As already depicted in Chapter 1, recently Hoznedl et al.[109] presented experimental and steady-state numerical results of flow in the LSB of a steam turbine with an axial diffuser. Temperature and pressure measurements highlight how the steam at the L1 inlet is superheated during LVF conditions. This justifies the ideal gas assumption adopted in many investigations [104, 104, 106] in literature and in the present work. They also demonstrated how a flow coefficient of 0.17 is the transition point for the ventilation of the last stage. In addition, by analyzing the trend of blade vibration as a function of the flow coefficient it is worth mentioning how the blade vibration experiences a significant increase in correspondence of a flow coefficient of 0.27 where the hub separation appears in the diffuser. Such vibration may be triggered by the flow unsteadiness in the hub separation vortex. The blade vibration increase continuously by decreasing the flow coefficient in the region of ventilation (pressure ratio at the tip higher than 1) up to reach a maximum in correspondence of a flow coefficient of 0.05 with the maximum pressure rise across the blade tip This peak of vibration may be due to the presence of the RI. Further decrease of the flow coefficient beyond this value leads to a decrease of blade vibration. Due to the primary importance of the flow coefficients in classifying the different steps towards the evolution of the transient flow field, in this investigation, similar values of flow coefficient respect to the ones presented by Hoznedl et al.[109] have been investigated.

The numerical setup used for this investigation is the one presented in

Chapter 2. In virtue of the findings proposed in the previous sub-section, two different fluid domains, reported in Figure 4.16, have been investigated: periodic and fully 3D. Several studies have indeed shown the applicability of RANS simulation to capture the characteristic flow features during LVF conditions [92, 93] reason why this setup has been used to perform a mesh sensitivity and to study the evolution of the flow field as a consequence of the reduction of the mass flow. This assessment has allowed to find out the most interesting operating points to be simulated with the full 3D unsteady approach.

The 3D domain considers a full annulus mesh of both the last stage and the axial exhaust hood (Figure 4.16), with struts included since the real geometry of the diffuser seems necessary to accurately predict the amplitude of pressure fluctuations[104]. In order to capture the flow unsteadiness the stator-rotor transient interface, available in CFX, coupled with the rotor moving mesh has been used. Additional full 3D RANS simulations with the frozen rotor interfaces have been carried out to initialize unsteady calculations.

The URANS simulations have been solved with a second-order backward Euler scheme and a time step of 2.3e-5 [s], resulting in 15 rotor mesh steps per pitch angle, which is sufficient to properly catch the blade passing effect, as shown by Fu et al. [129]; consequently, the selected time step can be used to detect both the tip RI which present a characteristic frequency far below the blade passing one [104, 106] and the hub separation vortex disturbances which act at even lower frequencies [99]. The total physical time simulated is averagely equal to 10 complete rotor revolutions (REV), which are, in some cases, essential to properly catch all the unsteady flow features, the exact number depends on the operating condition. Considering the fluid domain and the high physical time simulated, the average computational cost of each unsteady simulation is almost 100 K CPUh. As convergence criterion for unsteady simulations the summation of the resultant force on all blades has been considered, the minimum number of time steps is then reached when this monitor is stable with relative oscillation below 3%, the additional time steps above

this minimum have been decided based on the author's experience in order to collect sufficient transient data for the post-processing.

As already mentioned, the selection of the monitor points and post-processing surfaces plays a key role in the identification of transient instabilities. Similar approach respect to the one used for the radial exhaust has been used to locate the monitor points. A schematic representation of these is reported in Figure 4.16, they are spaced in two different rotor surfaces, at 3 different span sections (20,50,85%) and in 8 angular positions, making a total number of 48 monitor points. Each monitor point records the transient history of static and total pressure in both relative and absolute frames of reference. In addition, the integral pressure, the resultant force and the torque of 4 different rotor blades have been monitored.

Despite the significant number of monitor points, the analysis of a local signal may lead to an information loss, reason why also the 2D pressure fields, in plane SL11 and SL19 (Figure 4.16) have been stored to perform more in-depth post-processing based on Proper Orthogonal Decomposition (POD). Such a technique, proposed by Lumley [112], applied to fluid dynamic allows the decomposition of a complex flow field into several modes, ordering them according to their energy content. The graphical representation of each mode enables the identification of coherent structures within a turbulent flow, which are often embedded, favoring the understanding of how they interact and how they contribute to the development of a specific phenomenon. In this work, the so-called Snapshot POD proposed by Sirovinch [113, 114], as a development of the technique presented by Lumley [112], has been implemented in Matlab script. The theoretical explanation of the POD can be found in Chapter 1.

Concerning the boundary conditions, a total pressure, total temperature and flow direction profile have been imposed at the numerical inlet, such profiles have been calculated with the multi-stage steady-state calculation presented in [81] while at the outlet section an average static pressure value has been imposed. In order to study the evolution of

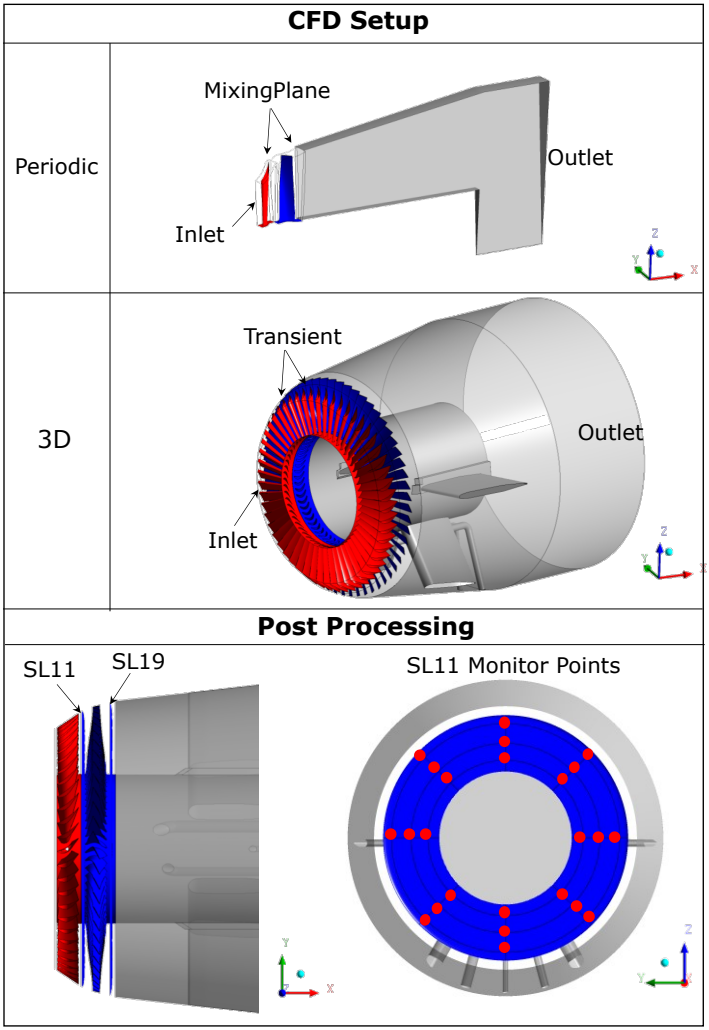

Figure 4.16: Numerical setup and post processing surfaces.

the flow field during LVF conditions, six different operating conditions, summarized in Table 4.4, have been investigated. The operating points studied in this chapter follow new nomenclature respect to one described in the previous section.

Table 4.4: Investigated operating conditions.

OP	TEST	$\overline{m}$ [-]	$\overline{U_{ax}}$ [-]	ϕ [-]	$\overline{\theta}$ [-]
OP0	B	1	1	0.52	0
OP1	A	0.224	0.195	0.10	0.96
OP2	A	0.375	0.375	0.25	0.73
OP3	B	0.653	0.653	0.16	0.87
OP4	B	0.322	0.322	0.06	1
OP5	B	0.522	0.522	0.13	0.92

The mass flow ($\overline{m}$) and axial velocity ($\overline{U_{ax}}$) at the diffuser inlet are normalized respect to the design value, while the swirl angle, calculated as the arctangent of the ratio between the tangential and axial velocity at the diffuser inlet, is normalized respect to OP4 value (maximum swirl condition).

The flow coefficient ϕ is calculated as the ratio between the axial velocity at the diffuser inlet and the tangential rotor speed at the mean radius. The OPs have been selected with two different strategies: TEST A starts from the off-design point and decreases the condenser pressure up to reach a safe condition within the stability range while TEST B starts from the design condition (OP0) and gradually increases the condenser pressure up to unsafe operations out from the stability range. It is worth highlighting how OP1 and OP4, and OP5 present flow coefficients within the range of instability identified by both Megerle et al.[104] and Hoznedl et al.[109].

The evaluation of 6 different operating conditions allows to define the application limits of the investigated steam turbine, illustrated in Figure 4.17, between these, the OP1 and the OP4 are defined as unsafe conditions due to the presence of strong unsteadiness in the flow field

which may trigger blade vibrations. In order to gradually characterize the transient behavior of the instabilities, the numerical results are presented starting with TEST A simulations, followed by TEST B ones.

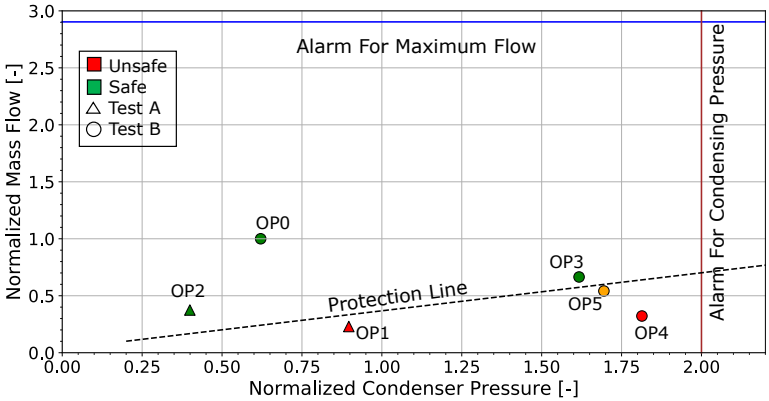

Figure 4.17: Steam turbine application limits.

The TEST A results are presented in Figure 4.18, in terms of FFT spectra of the pressure signals recorded in the relative monitor points presented in Figure 4.16. In this section, the amplitude of the pressure signal is presented as normalized quantity respect to a reference value, while the frequency is normalized respect to the rotational one, expressed as EO, and the physical time is normalized respect to the value to complete an entire rotor revolution, expressed as REV. The nomenclature of the monitor points follows the same criterion already explained in the previous sub-section.

In Figure 4.18a the FFT spectra of the pressure signal at 3 different span locations for a fixed stream-wise location is presented. By looking at this graph the higher level of unsteadiness of the tip section (85% span) is clear. In particular, a very strong peak of amplitude at 8 EO is well visible, as will be demonstrated later this peak is due to the presence of a rotating instability (RI) at the tip of the region between stator and rotor blades, reason why it is referred as RIF (Rotating Instability Frequency).

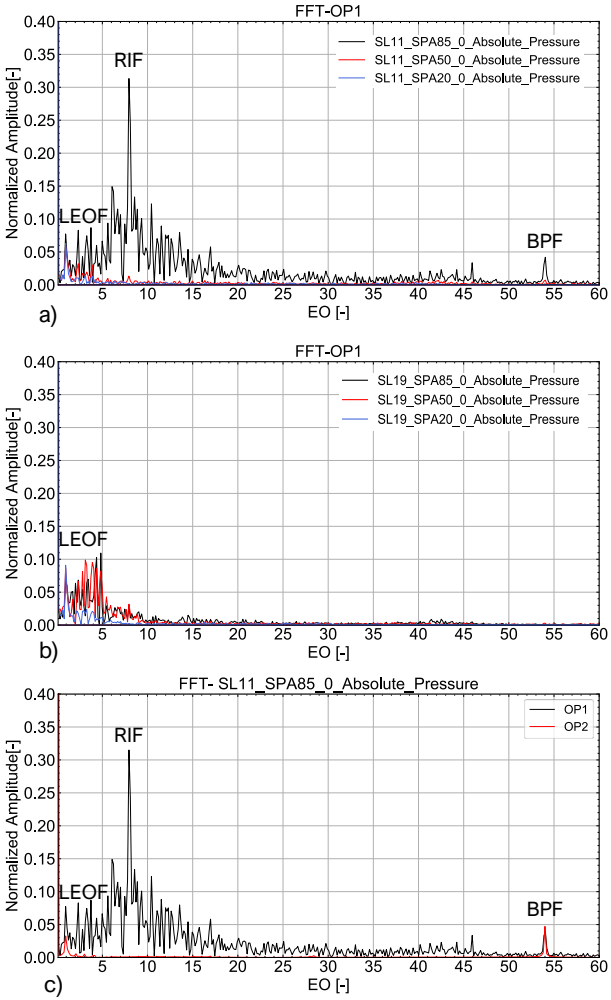

Figure 4.18: FFT spectra of relative monitor point pressure signal a) Effect of Spanwise location in the OP1 and surface SL11, b) Effect of Spanwise location in the OP1 and surface SL19, c) Comparison between OP1 and OP2 in surface SL11 at 85% span.

In line with the results presented in the literature review, the amplitude of the RIF is well above the one of the stator blade wake, pointed as BPF (Blade Passing Frequency). In addition, other low-frequency disturbances (LEOF) can be seen in the spectra, as explained later, such disturbances are due to diffuser asymmetry generated by the structural struts and to the hub separation vortex illustrated in Figure 1.11.

The LEOFs are clearly discernible also in Figure 4.18b, where the FFT spectra of the pressure in the surface SL19, between rotor blades and diffuser, are shown; while the RIF is no longer so evident. It is worth highlighting how the LEOF amplitude is well distinguishable in all the spectrum, meaning that such phenomenon, on the contrary respect to the RI, affects a wide section of the span. Specifically, the effect of the diffuser asymmetry at 1 EO is the same on the 3 signals since this is due to the presence of full-span structural struts only in the lower part of the diffuser, as shown in Figure 4.16. In Figure 4.18c is shown the effect of a different operating condition on the pressure signal in a monitor point located in the tip section of the SL11 surface. By looking at this graph it is clear how both the RIF and LEOF, except for the 1 EO linked to the diffuser asymmetry, disappear by decreasing the condenser pressure, while the stator wake effect amplitude is slightly stronger due to the higher mass flow of the OP2. For a sake of brevity, the effect of different circumferential locations of the monitor point is not presented, but it is worth mentioning how the signal of the RI is almost the same over the entire full annulus extension. Finally, in Figure 4.19 the FFT spectrum of the blade resultant force is reported, by looking at this graph it is clear how both the RI and the LEO instabilities observed in the pressure signals have a direct effect on the blade force since the same characteristic frequencies are clearly distinguishable.

As observed by previous investigations [105, 106], the RI is inherently unstable and changeable in time and for this reason, a STFT (Short Time Fourier Transform) is useful to study the evolution of the transient signal in the physical time. In figure 4.20b the STFT of the OP1 pressure signal at 85% of the SL11 surface is reported.

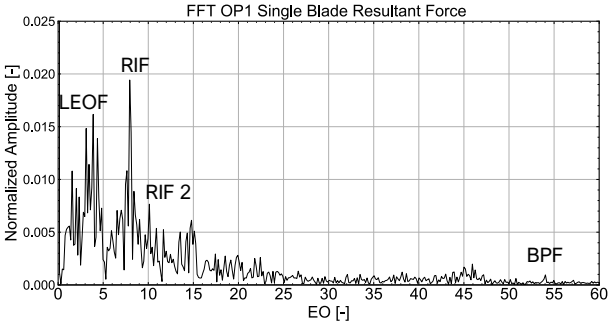

Figure 4.19: FFT spectrum of a singular blade resultant force.

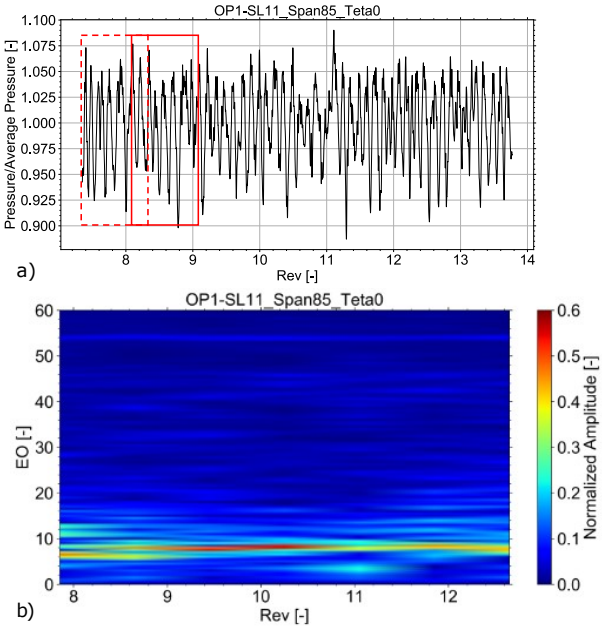

Figure 4.20: a) Pressure transient history with FFT moving windows (in red), b) STFT spectra of pressure signal.

The STFT is realized by considering a moving FFT window of 1 REV with an overlapping interval of 0.2 REV, as illustrated in Figure 4.20a. As can be seen by the STFT the signal of the RI is not constant in time, contrary to the stator wake visible at the top of the contour at 54 EO with a constant signal. Specifically, in the first part of the time window considered, between 8 and 9 REV, the RI signal is clearly visible with a characteristic frequency of 6 EO while in the final part of the time window, between 9 and 12 REV, the dominant frequency is shifted to 8 EO. In addition, another weaker signal of instability is visible at 11 EO, which, as will be shown thanks to POD, is associated with another RI configuration. Also the unsteadiness at LOEFs are present in this spectrogram with an unstable signal, between 2 and 4 EO, which reaches a maximum of amplitudes around 11 REV.

For a deeper investigation about the unsteady flow field in the SL11 surface, a POD analysis of the pressure field has been realized by processing a series of 1740 snapshots allowing the identification of the dynamics related to the different sources of unsteadiness observed in the FFT spectra. The time difference between each snapshot is equal to 2 time steps which determines a total time of 4 REV. The POD results are reported in Figure 4.21b,c,d while in Figure 4.21a is a snapshot of the pressure field.

In the snapshot of the pressure field, the stall cells near the casing can be seen. Such flow structures, by rotating in the circumferential direction with a fraction of the rotor speed, lead to the pressure oscillation observed in Figure 4.18. However, due to the instability of the signal shown in STFT this pattern shown by the snapshot is not stable in time, in this regard POD can be used for the identification of spatio-temporal evolution of this flow feature. As clarified in the numerical setup section, the POD is an energy-based decomposition that aims at determining the best approximation of a data set with a series of modes, each of which is characterized by spatial and temporal distribution and by its energy content. Figure 4.21b shows the singular and cumulative energy content of each POD mode. Since the energy is a measure of the importance

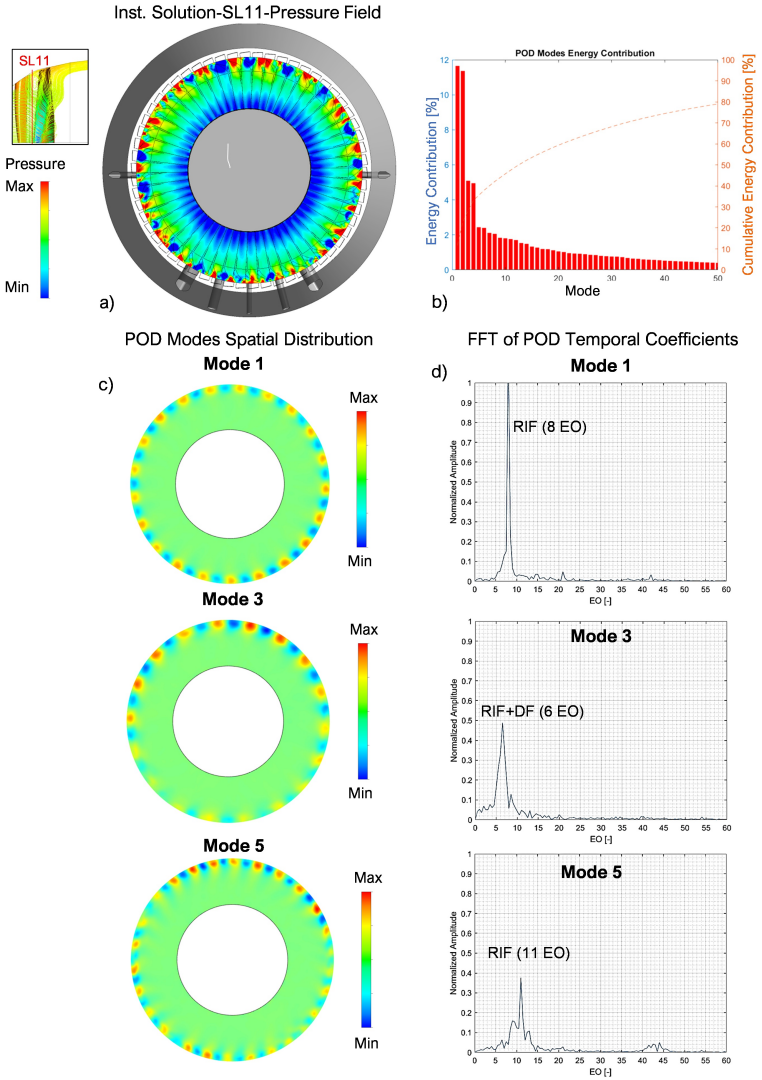

Figure 4.21: a) OP1 instantaneous pressure field on SL11 , b) POD modes energy contribution, c) Statistical POD Modes spatial distribution, d) FFT spectra of POD modes temporal coefficients.

of each mode it can be concluded that the first and second POD mode largely contributes to the resultant pressure field. The statistical spatial distribution of POD modes is presented in Figure4.21c, mode 1 is the principal mode and this is exactly the graphical representation of the RI with 16 stall cells pattern with a dominant frequency of 8 EO (RIF) clearly visible from both the spectrum of the POD temporal coefficients, in Figure 4.21d, and from the FFT spectra of pressure signal of the monitor point in Figure 4.18a. Mode 2 is not reported since it has the same dominant frequency, similar energy content and a shifted spatial distribution, this is typical behavior of convective flow [130] and it is valid also for modes 3-4 and modes 5-6. In the spatial distribution of mode 3, the already presented 16 stall cells pattern is still observable, however in this case there is a non-uniformity between the upper and the lower part of the surface. In particular, the stall cells in the upper part are more intense respect to the ones in the lower part. This effect leads to a shift of the characteristic frequency of the mode from 8 EO to 6 EO, already observed in STFT in Figure 4.20, and it may be related to the geometric asymmetry induced by the diffuser. Finally, in mode 5 another RI pattern with a different number of pressure cells can be observed, this confirms the thesis of temporal instability of this phenomenon. A similar dual RI configuration has been already reported in previous studies [88, 105, 106].

The results of TEST B are reported in Figure 4.22 with the FFT spectra of all the operating points and in Figure 4.23 with a specific focus on the OP4 which shows the RI and high LEO unsteadiness. Figure 4.22a reports the FFT spectra in the 85% span of the SL11 surface, the presence of the RI, already discussed for the OP1, in the OP4 is evident and it is worth highlighting how the characteristic frequency of such instability is different from the one presented for OP1. This is in line with the findings of previous studies [96, 104, 105, 106] which have already demonstrated that the RIF is related to the operating conditions. In addition, Figure 4.22a shows the FFT spectra of the design point OP0, which in line with expectations present only a strong peak of amplitude in correspondence of the BPF, while OP3 and OP5 show only very weak unsteadiness located

in the low-frequency region, meaning that the RI is not present in this conditions.

By looking at Figure 4.22b very strong unsteadiness at LOEFs can be seen, as already anticipated in TEST A results discussion, such instabilities are generated in the hub separation area behind the rotor blades and they are maximum in the OP4. For an in-depth explanation of this phenomenon, a POD analysis has been carried out in the SL19 surface by using 1740 snapshots of the pressure field.

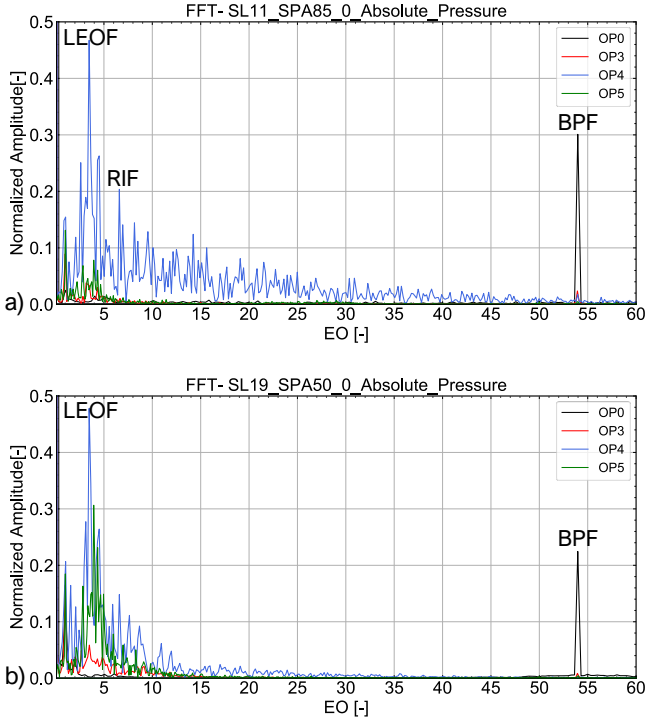

Figure 4.22: FFT spectra of relative pressure signal a) Effect of Spanwise location for all the OPs of TEST B at the tip of surface SL11, b) Effect of Spanwise location for all the OPs of TEST B at the mid of surface SL19.

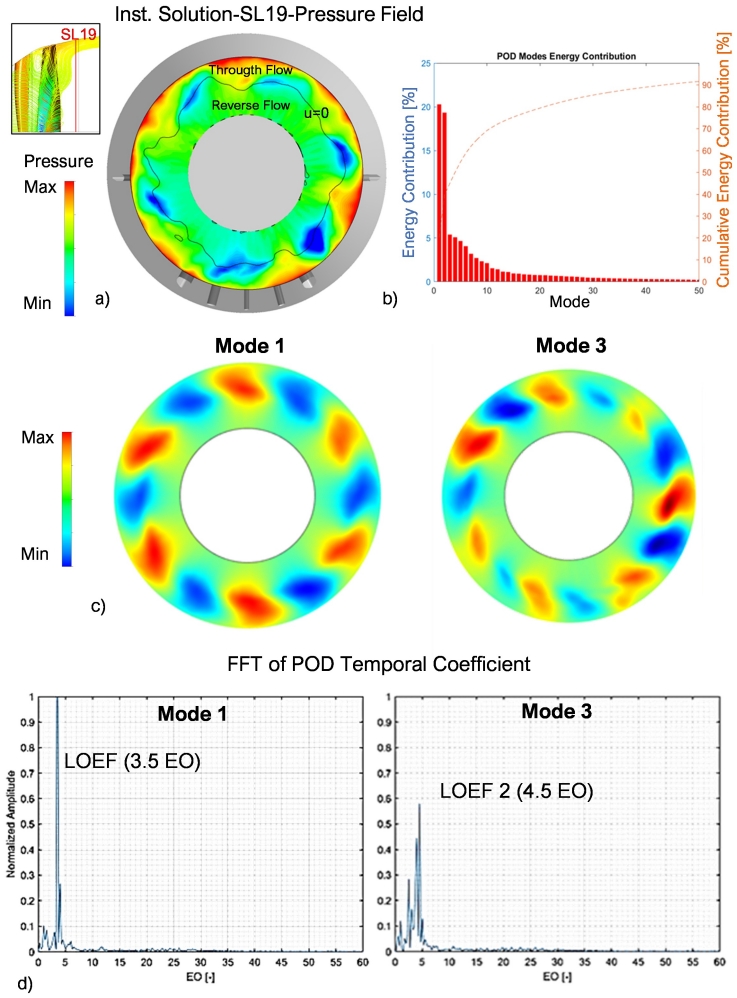

Figure 4.23: a) OP4 instantaneous pressure field on SL19, b) POD modes energy contribution, c) Statistical POD Modes spatial distribution, d) FFT spectra of POD modes temporal coefficients.

The results of the POD analysis are reported in Figure 4.23b,c,d together with a singular snapshot in Figure 4.23a. By looking at the pressure field in Figure 4.23a, a 6 pressure cells pattern can be easily seen. The rotation of these cells in the circumferential direction leads to the low-frequency instabilities observed previously and reported in Figure 4.22. These pressure cells are the cores of the helical vortices, generated due to the high swirl of the flow, located in the interface between the through flow and the reverse flow, as highlighted by the isoline at zero axial velocity in Figure 4.23a, where there is a very high tangential velocity gradient. This gradient is generated by the interaction between the high swirled flow which crosses the LSB tip and the hub separation vortex schematically shown in Figure 1.11.

The central role of the swirl in this phenomenon is also confirmed by looking at the data reported in Table 4.4, the OP1, OP4 and OP5 are the operating points characterized by the higher swirl angle and both experience well discernible pressure oscillations in the low-frequency region. This instability mechanism may be attributed to the Precessing Vortex Core (PVC) observed in several fluid dynamic applications. Aleeksenko et al. [131] described the formation of helical vortices in strongly swirled flow and in presence of separation, which may develop a rotation in the circumferential direction. The theory of helical vortices specifies how their number may depend on several factors, as confirmed by looking at the FFT spectra of OP4 and OP5 in Figure 4.22 where a slightly different dominant frequency in the low-frequency region can be seen, meaning that there is a different number of vortices. In addition, these vortices are not stationary and their number may vary in time [131]. This is confirmed by the POD analysis in Figure 4.23c where, by comparing mode 1 with mode 3 it is clear how the number of pressure cells, and consequently their dominant frequency, can vary during the transient evolution of the flow field. Concerning the modes' energy content, modes 1 and 2 largely contribute to the resultant pressure field since they are accountable for 40% of the global energy content. The spatial distribution of mode 1 clarifies how this phenomenon affects a significant part of the span,

contrary to the RI which is located only near the blade tip. However, the span extension and the amplitude of the pressure oscillations are strongly linked to the operating conditions, and in particular to the swirl number; indeed, by decreasing the swirl this phenomenon becomes weaker, as for the OP5 and OP1, and totally disappears in the other operating points. The present work has allowed the identification of a mechanism of instabilities linked to the hub separation vortex, an alternative to the tip RI widely observed in the literature. This finding is in line with numerical and experimental pieces of evidence proposed in the literature [90, 99, 109] which reported an increase of blade vibration in correspondence of the onset of the hub separation vortex in the diffuser.

Conclusions

This research activity aims at expanding the knowledge about different aspects of the aerodynamic behaviour of the steam turbine exhaust system through the development of numerical methods. The interest in such investigation is justified by the current trends in the steam turbine design practices, which are oriented towards more flexible operating conditions. In this scenario, new low-pressure blades are designed and integrated into an existing turbine casing, with previously designed exhaust hood. This procedure, the so called retrofitting, could lead to a drastic reduction of the aerodynamic performance of the exhaust system due to the strong coupling between last stage and exhaust hood, reasons why also a redesign of the exhaust hood should be required. In this regard, a numerical procedure has been developed to identify an optimal exhaust hood for a given last stage geometry and operating condition in an extremely reduced time. Such exhaust hood geometry can guarantee high aerodynamic performance in design operating condition with an overall volume consistent with the industrial needs. The definition of this procedure has required a two-step development and it is finally based on the definition of a periodic CFD model, which is fundamental to perform the DOE study in feasible time. The CFD numerical setup has been selected as a final output of a sensitivity analysis aimed at assessing the influence of different numerical strategies on the flow field resolution. Specifically, the impact of computational grids, rotor-static component interfaces and geometric simplification has been evaluated. The results of the periodic model DOE analysis have been used to develop a response surface which describes the exhaust

hood performance as a function of input geometrical parameters. For the selection of these parameter, the lesson learnt with the first step of the development of the procedure is crucial since it demonstrates the strong impact of the outer casing on the diffuser performance. The parametric model should therefore include parameters of both the outer casing and diffuser to properly optimize the pressure recovery. It is worth recalling how, in order to perform a DOE study with a significant number of geometric parameter, is necessary to reduce the computational cost of each simulation to maintain the overall time needed by the procedure consistent with the industrial time table.

The response surface once reached an acceptable level of accuracy, is used by an optimization algorithm to find out a high-performing exhaust hood for the given application. Due to the strong assumption needed to approximate a radial exhaust hood with a periodic geometry, a final verification with the 3D model is required to check the performance improvement. The comparison between the periodic and the 3D model has highlighted a good agreement in both the averaged pressure recovery factor prediction and flow field resolution within the diffuser, with a speedup of the computational time by about one order of magnitude. The simplified model coupled with the optimization procedure can be, therefore, used as a design tool for preliminary screening of the most interesting geometries, which should later be simulated with a more sophisticated numerical approach as verification.

The application of this numerical procedure to an exhaust system manufactured by Baker Hughes has allowed to identify an optimum geometry with a pressure recovery factor, calculated in the condenser section, 28% greater than the baseline one. The improvement of the performance is achieved even with a reduction of the exhaust system volume equal to 4%. Such significant improvement has been obtained with an optimization of the hub cone angle which allows avoiding the flow separation. In addition, the optimization of the outer casing allows controlling the vortices strength reducing the losses within the exhaust hood.

According to the findings proposed in this work, the optimization procedure should only be carried out in the design operating condition since it is one in which a high pressure recovery is of primary interest. A drop of performance in off-design operations seems unavoidable also optimizing the geometry in such conditions. The low axial velocity and the consequent high swirl angle at the diffuser inlet play a key role in the drop of performance in reduced load conditions by leading to the Hub Cone Separation which acts as aerodynamic blockage causing the drop of performance. It is worth highlighting how such behavior is also exaggerated when the structural struts are included in the numerical domain, the interaction between these supports and high swirl angle leads to a dramatic increase of the pressure losses and local acceleration of the flow with an inevitable drop of the pressure recovery.

Once fixed the exhaust hood geometry, the assessment of the flow field behavior in off-design conditions is essential not only to study the trend of the performance but to investigate the unsteady fluid dynamic phenomena in the last stage during LVF conditions. Such conditions are indeed potentially dangerous for the low pressure turbine blades since they may experience flow-induced vibrations triggered by the surrounding fluid. Due to the different fluid behavior between axial and radial exhaust hoods, the LVF analysis has been carried out with both these exhaust configurations.

The radial exhaust hood investigated is the one identified with the optimization procedure. The already mentioned simplified periodic model has been used to perform RANS simulation aimed at characterizing the evolution of the flow field during LVF conditions. Such numerical setup has proven to be effective in showing the main flow features during these conditions, however, due to inherent unsteadiness and strong three-dimensionality of the flow, it fails to detect the mechanisms responsible for the flow-induced vibration. Before considering the full 3D unsteady numerical setup, a periodic model unsteady setup has been tested. This allows a significant reduction of the computational costs and it allows to detect of the unsteady phenomena responsible for flow-induced vibration,

however, in line with the findings proposed by the literature review, it fails to predict the frequency and the amplitude of the instabilities. For this reason, to properly investigate these phenomena full 3D unsteady simulations are required. In this work, such simulations are deeply discussed and studied with an axial diffuser manufactured by Baker Hughes for concentrated solar power plant application. This diffuser, with struts included, has been coupled with a full annulus mesh of the last stage of the low pressure turbine. Six operating conditions have been simulated with the 3D setup allowing to identify of the application limits of the turbine aimed at avoiding the operations in unsafe conditions, characterized by strong pressure oscillations in the LSB which may trigger vibrations. The rotating instability accountable for a significant part of this pressure oscillation has been detected in the tip region between stator and rotor. The strong link between pressure oscillations and alternating blade loads has been clarified by monitoring the blade force. The FFT spectrum of a single blade force revealed indeed the same peaks observed in the pressure signals.

A graphical representation of this instability has been presented thanks to the Proper Orthogonal Decomposition which allows decomposing a complex flow field into different modes, ranked by their energy content. In this case, the RI is manifested with a 16 pressure cells pattern which counter rotates respect to the rotor motion with a fraction of its speed. The tip RI mechanism is line with other studies found in literature [78, 104, 105, 106]. In addition, the application of 2D POD has allowed avoiding the potential loss of information linked to post-processing based on local monitor points allowing to identify the region of maximum pressure oscillations in both the surfaces investigated.

The RI is not the only source of unsteadiness detected in this work, indeed, in line with the findings of other investigations [90, 99, 109], low-frequency instabilities behind the rotor blades are revealed. These instabilities are generated by the interaction between the hub separation vortex in the diffuser and the strongly swirled flow at the outlet of the rotor, confined at the tip. The high-velocity gradient between through

and reverse flow leads to the onset of helical vortices, with the vortex core located in the zero velocity separation line, which rotates with a mechanism similar to the ones observed for the tip RI. In line with the the described phenomena.

Cornering the optimization procedure, the integration of uncertainty Quantification techniques (UQ) may represent an interesting way of development.

List of Figures

List of Tables

Bibliography

[1] Renewables 2020. In *//www.iea.org/reports/renewables-2020*, volume IEA, 2020.

[2] "Global renewables outlook: Energy transformation 2050." 2020.

[3] EIA. "International energy outlook 2021." 2021.

[4] Gonzalez-Salazar, Miguel Angel, Kirsten, Trevor, and Prchlik, Lubos. "Review of the operational flexibility and emissions of gas-and coal-fired power plants in a future with growing renewables." *Renewable and Sustainable Energy Reviews*, 82:1497–1513, 2018.

[5] Gülen, Seyfettin Can. "Steam turbine-quo vadis?" *Frontiers in Energy Research*, 2021.

[6] Nakamura, Tateki, Segawa, Kiyoshi, Isobe, Nobuhiro, and Saito, Eng Takashi. "Highly-reliable design technology of steam turbine for nuclear power plant." *Hitachi Hyoron*, 91(2):224–225, 2009.

[7] Asai, Kunio, Kurosawa, Atsuhiro, and Lee, Goingwon. "Titanium 50-inch and 60-inch last-stage blades for steam turbines." *Hitachi Review*, 62(1):23, 2013.

[8] Lübbe, Bertold, Aschenbruck, Jens, Pütz, Oliver, and Theidel, Mira. Design and validation of a large steam turbine end-stage blade to meet current and future market demands. In *Turbo Expo: Power for*

Land, Sea, and Air, volume 85017, page V008T22A014. American Society of Mechanical Engineers, 2021.

[9] Keller, H. "Low pressure turbine exhaust system design." *Aerothermodynamics of low pressure steam turbines and condensers. Hemisphere Publishing, New York, NY*, 1986.

[10] Stein, Peter, Pfoster, Christoph, Sell, Michael, Galpin, Paul, and Hansen, Thorsten. Cfd modeling of low pressure steam turbine radial diffuser flow by using a novel multiple mixing plane based coupling: Simulation and validation. In *Turbo Expo: Power for Land, Sea, and Air*, volume 56796, page V008T26A020. American Society of Mechanical Engineers, 2015.

[11] Zaryankin, AE, Simonov, BP, Paramonov, AN, and Chusov, SA. "Advancements in the aerodynamics of exhaust hoods of turbines." *Thermal engineering*, 45(1):23–27, 1998.

[12] Burton, Zoe, Ingram, Grant L, and Hogg, Simon. "A literature review of low pressure steam turbine exhaust hood and diffuser studies." *Journal of Engineering for Gas Turbines and Power*, 135 (6), 2013.

[13] Mizumi, Shunsuke, Ishibashi, Kouji, and Sawamura, Yasuaki. Steam turbine exhaust hood with swirl flow separation ducts. In *Turbo Expo: Power for Land, Sea, and Air*, volume 44724, pages 385–393. American Society of Mechanical Engineers, 2012.

[14] Zhang, Wei, Paik, Bu Geun, Jang, Young Gil, Lee, Sang Joon, Lee, Su Eon, and Kim, Jin Hwan. "Particle image velocimetry measurements of the three-dimensional flow in an exhaust hood model of a low-pressure steam turbine." 2007.

[15] Xu, X, Kang, S, and Hirsch, CH. Numerical simulation of the 3d viscous flow in the exhaust casing of a low-pressure steam turbine. In *Turbo Expo: Power for Land, Sea, and Air*, volume 78507, page V001T03A071. American Society of Mechanical Engineers, 2001.

[16] Fu, Jing-Lun and Liu, Jian-Jun. "Influences of inflow condition on non-axisymmetric flows in turbine exhaust hoods." *Journal of Thermal Science*, 17(4):305–313, 2008.

[17] Munyoki, Dickson, Schatz, Markus, and Vogt, Damian M. Detailed numerical study of the main sources of loss and flow behavior in low pressure steam turbine exhaust hoods. In *Turbo Expo: Power for Land, Sea, and Air*, volume 50954, page V008T29A004. American Society of Mechanical Engineers, 2017.

[18] McDonald, AT, Fox, RW, and Van Dewoestine, RV. "Effects of swirling inlet flow on pressure recovery in conical diffusers." *AIAA Journal*, 9(10):2014–2018, 1971.

[19] Kumar, DS and Kumar, KL. "Effect of swirl on pressure recovery in annular diffusers." *Journal of Mechanical Engineering Science*, 22(6):305–313, 1980.

[20] UVAROV, VV, SHKURIKHIN, IB, and MOLYAKOV, VD. "Investigation of joint operation of turbine stages and of a radial-annular diffuser with a controlled boundary-layer." *Thermal Engineering*, 23(5):18–22, 1976.

[21] Fu, Jing-Lun and Liu, Jian-Jun. Investigations of influential factors on the aerodynamic performance of a steam turbine exhaust system. In *Turbo Expo: Power for Land, Sea, and Air*, volume 44021, pages 2159–2169, 2010.

[22] Yin, Mingyan, Yang, Chen, Meng, Liu, Yan, Wei, Zhuhai, Zhong, Li, Jun, and Feng, Zhenping. Numerical analysis on the swirl flows in the exhaust hood of steam turbine and optimization design. In *Turbo Expo: Power for Land, Sea, and Air*, volume 49866, page V008T26A002. American Society of Mechanical Engineers, 2016.

[23] Beevers, Adam, Congiu, Francesco, Pengue, Fabio, and Mokulys, Thomas. An analysis of the merits of cfd for the performance prediction of a low pressure steam turbine radial diffuser. In

Turbo Expo: Power for Land, Sea, and Air, volume 44021, pages 563–574, 2010.

[24] Liu, JJ and Hynes, TP. The investigation of turbine and exhaust interactions in asymmetric flows: Part 1—blade-row models applied. In *Turbo Expo: Power for Land, Sea, and Air*, volume 3610, pages 169–177, 2002.

[25] Tindell, RH, Alston, TM, Sarro, CA, Stegmann, GC, Gray, L, and Davids, J. "Computational fluid dynamics analysis of a steam power plant low-pressure turbine downward exhaust hood." 1996.

[26] Kreitmeier, F and Greim, R. "Optimization of blade—diffuser interaction for improved turbine performance." *Proceedings of the Institution of Mechanical Engineers, Part A: Journal of Power and Energy*, 217(4):443–451, 2003.

[27] Gardzilewicz, ANDRZEJ, Swirydczuk, J, Badur, Janusz, Karcz, MICHAŁ, Werner, ROBERT, and Szyrejko, CZESŁAW. "Methodology of cfd computations applied for analysing flow through steam turbine exhaust hoods." *Transactions of the Institute of Fluid-flow Machinery*, 113:157–168, 2003.

[28] Liu, JJ, Cui, YQ, and Jiang, HD. "Investigation of flow in a steam turbine exhaust hood with/without turbine exit conditions simulated." *J. Eng. Gas Turbines Power*, 125(1):292–299, 2003.

[29] Sadasivan, S, Arumugam, SK, and Aggarwal, MC. "An alternative numerical model for investigating three-dimensional steam turbine exhaust hood." *Journal of Applied Fluid Mechanics*, 13(2):639–650, 2020.

[30] Sadasivan, Sreeja, Kumar Arumugam, Senthil, and Aggarwal, Mahesh C. "Computational investigation of multi-phase flow effects on the performance of the steam turbine exhaust hood." *Proceedings of the Institution of Mechanical Engineers, Part A: Journal of Power and Energy*, 235(2):279–290, 2021.

[31] Benim, AC, Geiger, M, Doehler, S, Schoenenberger, M, and Roemer, H. "Modelling the flow in the exhaust hood of steam turbines under consideration of turbine-exhaust hood interaction." *VDI BERICHTE*, 1185:343–343, 1995.

[32] Taylor, Derek, Singh, Gurnam, Hemsley, Phil, and Claridge, Martin. Parametric experimental and numerical study of lp diffuser and exhaust hoods. In *Turbo Expo: Power for Land, Sea, and Air*, volume 49866, page V008T26A017. American Society of Mechanical Engineers, 2016.

[33] Fu, Jing-Lun and Liu, Jian-Jun. "Investigations on the improving aerodynamic performances of last stage steam turbine and exhaust hood under design and off design conditions." *Journal of Thermal Science*, 24(5):468–477, 2015.

[34] Fu, J, Liu, J, and Zhou, S. "Experimental and numerical investigation of interaction between turbine stage and exhaust hood." *Proceedings of the Institution of Mechanical Engineers, Part A: Journal of Power and Energy*, 221(7):991–999, 2007.

[35] Li, Zhigang, Li, Jun, Yan, Xin, Feng, Zhenping, Ohyama, Hiroharu, and Zhang, Ming. Investigations on the flow pattern and aerodynamic performance of last stage and exhaust hood for large power steam turbines. In *Turbo Expo: Power for Land, Sea, and Air*, volume 44724, pages 569–577. American Society of Mechanical Engineers, 2012.

[36] Verstraete, Tom, Prinsier, Johan, Di Sante, Alberto, Della Gatta, Stefania, and Cosi, Lorenzo. Design optimization of a low pressure steam turbine radial diffuser using an evolutionary algorithm and 3d cfd. In *Turbo Expo: Power for Land, Sea, and Air*, volume 44724, pages 603–613. American Society of Mechanical Engineers, 2012.

[37] Živnỳ, A, Macálka, A, Hoznedl, M, Sedlák, K, Hajšman, M, and Kolovratník, M. Numerical investigation and validation of the 1 090 mw steam turbine exhaust hood flow field. In *Turbo Expo: Power for Land, Sea, and Air*, volume 50954, page V008T29A015. American Society of Mechanical Engineers, 2017.

[38] Fan, Tao, Xie, Yonghui, Zhang, Di, and Sun, Bi. A combined numerical model and optimization for low pressure exhaust system in steam turbine. In *ASME power conference*, volume 42738, pages 349–358, 2007.

[39] Verstraete, Tom, Prinsier, Johan, and Cosi, Lorenzo. Design and off-design optimization of a low pressure steam turbine radial diffuser using an evolutionary algorithm and 3d cfd. In *Turbo Expo: Power for Land, Sea, and Air*, volume 45585, page V01BT27A046. American Society of Mechanical Engineers, 2014.

[40] Burton, Zoe, Ingram, Grant, and Hogg, Simon. A novel method of coupling the steam turbine exhaust hood and the last stage blades using the non-linear harmonic method. In *ASME turbo expo 2013: turbine technical conference and exposition*. American Society of Mechanical Engineers Digital Collection, 2013.

[41] Mambro, Antonio, Congiu, Francesco, and Galloni, Enzo. Cfd modelling of steam turbine last stage blades at low load using multiple mixing plane approach. In *Turbo Expo: Power for Land, Sea, and Air*, volume 84201, page V009T23A012. American Society of Mechanical Engineers, 2020.

[42] Stanciu, M, Fendler, Y, and Dorey, JM. Unsteady stator-rotor interaction coupled with exhaust hood effect for last stage steam turbines. In *Proceedings of the 9th European Turbomachinery Conference, Istanbul, March*, pages 21–25, 2011.

[43] Zimmermann, C and Stetter, H. Experimental determination of the flow field in the tip region of a lp-steam turbine. In *Turbo Expo:*

Power for Land, Sea, and Air, volume 78880, page V001T03A047. American Society of Mechanical Engineers, 1993.

[44] Willinger, Reinhard and Haselbacher, Hermann. *The role of rotor tip clearance on the aerodynamic interaction of a last gas turbine stage and an exhaust diffuser*, volume 78620. American Society of Mechanical Engineers, 1998.

[45] Burton, Zoe, Hogg, Simon, and Ingram, Grant. A generic low pressure exhaust diffuser for steam turbine research. In *Turbo Expo: Power for Land, Sea, and Air*, volume 44724, pages 455–466. American Society of Mechanical Engineers, 2012.

[46] Becker, S, Gretschel, E-Ch, and Casey, M. Influence of a tip clearance jet on a swirling flow in an axial-radial diffuser. In *Proceedings of the 6th European Turbomachinery Conference*, 2005.

[47] Huang, PG, Bardina, J, and Coakley, T. "Turbulence modeling validation, testing, and development." *NASA technical memorandum*, 110446:147, 1997.

[48] Kasilov, VF and Sharkov, AV. "Evaluating the effect of steam wetness on the efficiency of the exhaust hoods of the low-pressure cylinders of steam turbines." *Thermal engineering*, 51(5):378–383, 2004.

[49] Tanuma, Tadashi, Sasao, Yasuhiro, Yamamoto, Satoru, Niizeki, Yoshiki, Shibukawa, Naoki, and Saeki, Hiroshi. Numerical investigation of three-dimensional wet steam flows in an exhaust diffuser with non-uniform inlet flows from the turbine stages in a steam turbine. In *Turbo Expo: Power for Land, Sea, and Air*, volume 44724, pages 589–602. American Society of Mechanical Engineers, 2012.

[50] Grübel, M, Starzmann, J, Schatz, M, Eberle, T, Vogt, DM, and Sieverding, F. "Two-phase flow modeling and measurements in

low-pressure turbines—part i: numerical validation of wet steam models and turbine modeling." *Journal of Engineering for Gas Turbines and Power*, 137(4), 2015.

[51] Schatz, M, Eberle, T, Grübel, M, Starzmann, J, Vogt, DM, and Suerken, N. "Two-phase flow modeling and measurements in low-pressure turbines—part ii: Turbine wetness measurement and comparison to computational fluid dynamics-predictions." *Journal of Engineering for Gas Turbines and Power*, 137(4), 2015.

[52] Štastnỳ, Miroslav, Tajc, Ladislav, Kolár, Petr, and Tucek, Antonín. "Effects of inlet swirl on the flow in a steam turbine exhaust hood." *Journal of Thermal Science*, 9(4):327–333, 2000.

[53] Stein, Peter, Telschow, Dirk, Lamarque, Frederic, and Colitto, Nuncio. Low pressure steam turbine exhaust flow: Part 1—cfd coupling of lp turbine and condenser neck. In *Turbo Expo: Power for Land, Sea, and Air*, volume 49866, page V008T26A025. American Society of Mechanical Engineers, 2016.

[54] Telschow, Dirk, Stein, Peter, Wolf, Hartwig, and Sgambati, Alessandro. Low pressure steam turbine exhaust flow: Part 2—investigation of the condenser neck flow field and 1d modelling. In *Turbo Expo: Power for Land, Sea, and Air*, volume 49866, page V008T26A026. American Society of Mechanical Engineers, 2016.

[55] Xu, Qing, Lin, Aqiang, Cai, Yuhang, Ahmad, Naseem, Duan, Yu, and Liu, Chen. "Numerical analysis of aerodynamic characteristics of exhaust passage with consideration of wet steam effect in a supercritical steam turbine." *Energies*, 13(7):1560, 2020.

[56] Queipo, Nestor V, Haftka, Raphael T, Shyy, Wei, Goel, Tushar, Vaidyanathan, Rajkumar, and Tucker, P Kevin. "Surrogate-based analysis and optimization." *Progress in aerospace sciences*, 41(1): 1–28, 2005.

[57] Madavan, Nateri K, Rai, Man Mohan, and Huber, Frank W. *Neural net-based redesign of transonic turbines for improved unsteady aerodynamic performance*. National Aeronautics and Space Administration, Ames Research Center, 1998.

[58] Rai, Man Mohan and Madavan, Nateri K. "Aerodynamic design using neural networks." *AIAA journal*, 38(1):173–182, 2000.

[59] Madsen, Jens I, Shyy, Wei, and Haftka, Raphael T. "Response surface techniques for diffuser shape optimization." *AIAA journal*, 38(9):1512–1518, 2000.

[60] Shyy, Wei, Papila, Nilay, Tucker, Kevin, Vaidyanathan, Raj, and Griffin, Lisa. "Global design optimization for fluid machinery applications." 2000.

[61] Papila, Nilay, Shyy, Wei, Griffin, Lisa, and Dorney, Daniel J. "Shape optimization of supersonic turbines using global approximation methods." *Journal of Propulsion and Power*, 18(3):509–518, 2002.

[62] Hedayat, A Samad, Sloane, Neil James Alexander, and Stufken, John. *Orthogonal arrays: theory and applications*. Springer Science & Business Media, 1999.

[63] McKay, MD, Beckman, RJ, and Conover, WJ. "Comparison the three methods for selecting values of input variable in the analysis of output from a computer code." *Technometrics;(United States)*, 21(2), 1979.

[64] Awad, Mariette and Khanna, Rahul. *Efficient learning machines: theories, concepts, and applications for engineers and system designers*. Springer nature, 2015.

[65] Yoon, Sungho, Stanislaus, Felix Joe, Mokulys, Thomas, Singh, Gurnam, and Claridge, Martin. A three-dimensional diffuser design for the retrofit of a low pressure turbine using in-house exhaust design

system. In *Turbo Expo: Power for Land, Sea, and Air*, volume 54679, pages 2309–2319, 2011.

[66] Musch, Christian, Stu¨ er, Heinrich, and Hermle, Georg. Optimization strategy for a coupled design of the last stage and the successive diffuser in a low pressure steam turbine. In *Turbo Expo: Power for Land, Sea, and Air*, volume 54679, pages 2407–2415, 2011.

[67] Musch, Christian, Cremanns, Kevin, Hecker, Simon, and Penkner, Andreas. Combined optimisation of the last stage and diffuser in a steam turbine using meta-model. In *12 th European Conference on Turbomachinery Fluid dynamics & Thermodynamics*. EUROPEAN TURBOMACHINERY SOCIETY, 2017.

[68] Mizumi, Shunsuke and Ishibashi, Kouji. Design philosophy and methodology of a low pressure exhaust hood for a large power steam turbine. In *Turbo Expo: Power for Land, Sea, and Air*, volume 55201, page V05BT25A007. American Society of Mechanical Engineers, 2013.

[69] Lihua, CAO, Aqiang, LIN, Yong, LI, and Bin, XIAO. "Optimum tilt angle of flow guide in steam turbine exhaust hood considering the effect of last stage flow field." *Chinese Journal of Mechanical Engineering*, 30(4):866–875, 2017.

[70] Wang, Hongtao, Zhu, Xiaocheng, Du, Zhaohui, and Yang, Hong. Aerodynamic optimization system development for low pressure exhaust hood of steam turbine. In *Turbo Expo: Power for Land, Sea, and Air*, volume 44021, pages 2139–2148, 2010.

[71] Ding, Bowen and Xu, Liping. Designing steam turbine exhaust diffusers using minimum energy curves. In *Proceedings of Shanghai 2017 Global Power and Propulsion Forum, 30 Oct–1 Nov. Paper No. GPPS2017*, volume 60, 2017.

[72] Ding, Bowen, Xu, Liping, Yang, Jiandao, Yang, Rui, and Dai, Yuejin. The effect of stage-diffuser interaction on the aerodynamic

performance and design of lp steam turbine exhaust systems. In *Turbo Expo: Power for Land, Sea, and Air*, volume 51173, page V008T29A013. American Society of Mechanical Engineers, 2018.

[73] Liu, JJ and Hynes, TP. The investigation of turbine and exhaust interactions in asymmetric flows: Part 2—turbine-diffuser-collector interactions. In *Turbo Expo: Power for Land, Sea, and Air*, volume 3610, pages 179–188, 2002.

[74] Finzel, Conrad, Schatz, Markus, Casey, Michael V, and Gloss, Daniel. Experimental investigation of geometrical parameters on the pressure recovery of low pressure steam turbine exhaust hoods. In *Turbo Expo: Power for Land, Sea, and Air*, volume 54679, pages 2255–2263, 2011.

[75] Munyoki, Dickson, Schatz, Markus, and Vogt, Damian M. Numerical investigation of the influence of hood height variation on performance of low pressure steam turbine exhaust hoods. In *Turbo Expo: Power for Land, Sea, and Air*, volume 51173, page V008T29A031. American Society of Mechanical Engineers, 2018.

[76] Munyoki, Dickson, Schatz, Markus, and Vogt, Damian M. Numerical investigation of the influence of flow deflection at the upper hood on performance of low pressure steam turbine exhaust hoods. In *Turbo Expo: Power for Land, Sea, and Air*, volume 58714, page V008T29A008. American Society of Mechanical Engineers, 2019.

[77] M. Gloger, K. Neumann and Termuehlen, H. "Design criteria for reliable low-pressure blading." *ASME Paper*, 86, 1986.

[78] Megerle, Benjamin, Stephen Rice, Timothy, McBean, Ivan, and Ott, Peter. "Numerical and experimental investigation of the aerodynamic excitation of a model low-pressure steam turbine stage operating under low volume flow." *Journal of engineering for gas turbines and power*, 135(1), 2013.

[79] Bessone, A, Guida, R, Marrè Brunenghi, M, Patrone, S, Carassale, L, Kubin, Z, Arnone, A, and Pinelli, L. Aeromechanical characterization of a last stage steam blade at low load operation: Part 1—experimental measurements and data processing. In *Turbo Expo: Power for Land, Sea, and Air*, volume 84218, page V10AT24A019. American Society of Mechanical Engineers, 2020.

[80] Pinelli, Lorenzo, Vanti, Federico, Peruzzi, Lorenzo, Arnone, Andrea, Bessone, Andrea, Bettini, Claudio, Guida, Roberto, Marré Brunenghi, Michela, and Slama, Vaclav. Aeromechanical characterization of a last stage steam blade at low load operation: Part 2—computational modelling and comparison. In *Turbo Expo: Power for Land, Sea, and Air*, volume 84218, page V10AT24A017. American Society of Mechanical Engineers, 2020.

[81] Pinelli, Lorenzo, Mariotti, Filippo, Arnone, Andrea, Marconcini, Michele, and Arcangeli, Lorenzo. "Numerical investigation of flow induced vibrations of steam turbine last stage rotor at low load operation – part 1: Sensitivity to flutter occurrence." *ASME 2022, not still published*, 2022.

[82] Filippenko, Victor, Frolov, Boris, Chernobrovkin, Andrey, Zhou, Bin, Mujezinovic´, Amir, and Slepski, Jon. Analyses of temperature distribution on steam turbine last stage low pressure buckets at low flow operations. In *Turbo Expo: Power for Land, Sea, and Air*, volume 54679, pages 2463–2469, 2011.

[83] Beevers, Adam, Havakechian, Said, and Megerle, Benjamin. "On the prediction and theory of the temperature increase of low pressure last stage moving blades during low volume flow conditions, and limiting it through steam extraction methods." *Journal of Turbomachinery*, 137(10):101002, 2015.

[84] Mambro, Antonio, Congiu, Francesco, and Galloni, Enzo. "Influence of the snubber on temperature distribution at last stage blade exit

of a steam turbine during low volume flow operations." *Applied Thermal Engineering*, 150:937–952, 2019.

[85] Y. Shnee, M. Fedorov F. Ponomarev and Bystritskii, L. "Features of operation of a turbine stage with low dm/l ratio under conditions of low loads." *Teploenergetika*, 18:39 – 42, 1971.

[86] Y. Shnee, V. Slabchenko M. Zatsev O. Ponomarev and Fedorov, M. "Influence of the operational factors on dynamic stresses in moving blades of a turbine stage." *Teploenergetika*, 21:49 – 52, 1974.

[87] Schmidt, D and Riess, W. Steady and unsteady flow measurements in the last stages of lp steam turbines. In *IMECHE CONFERENCE TRANSACTIONS*, volume 1, pages 723–734. MECHANICAL ENGINEERING PUBLICATIONS, 1999.

[88] Gerschütz, Wolfram, Casey, Michael, and Truckenmüller, Frank. "Experimental investigations of rotating flow instabilities in the last stage of a low-pressure model steam turbine during windage." *Proceedings of the Institution of Mechanical Engineers, Part A: Journal of Power and Energy*, 219(6):499–510, 2005.

[89] Zhang, LY, He, L, and Stüer, H. "A numerical investigation of rotating instability in steam turbine last stage." *Journal of turbomachinery*, 135(1), 2013.

[90] Segawa, Kiyoshi, Senoo, Shigeki, Hamatake, Hisashi, Kudo, Takeshi, Nakamura, Tateki, and Shibashita, Naoaki. Steady and unsteady flow measurements under low load conditions in a low pressure model steam turbine. In *International Conference on Nuclear Engineering*, volume 44977, pages 833–839. American Society of Mechanical Engineers, 2012.

[91] Senoo, Shigeki, Segawa, Kiyoshi, Hamatake, Hisashi, Kudo, Takeshi, Nakamura, Tateki, and Shibashita, Naoaki. "Computations for unsteady compressible flows in a multistage steam turbine with

steam properties at low load operations." *Journal of engineering for gas turbines and power*, 133(10), 2011.

[92] Herzog, N, Gu¨ ndogdu, Y, Kang, G, Seume, JR, and Rothe, K. Part load operation of a four-stage turbine. In *Turbo Expo: Power for Land, Sea, and Air*, volume 47306, pages 663–672, 2005.

[93] Sigg, R, Heinz, Ch, Casey, MV, and Sürken, N. "Numerical and experimental investigation of a low-pressure steam turbine during windage." *Proceedings of the Institution of Mechanical Engineers, Part A: Journal of Power 19 and Energy*, 223(6):697–708, 2009.

[94] Zhang, LY, He, L, and Stüer, H. 3-d time domain unsteady computation of rotating instability in steam turbine last stage. In *Turbo Expo: Power for Land, Sea, and Air*, volume 44724, pages 559–567. American Society of Mechanical Engineers, 2012.

[95] Shibukawa, Naoki, Tejima, Tomohiro, Iwasaki, Yoshifumi, Murakami, Itaru, and Saito, Ikuo. A correlation between vibration stresses and flow features of steam turbine long blades in low load conditions. In *Turbo Expo: Power for Land, Sea, and Air*, volume 54679, pages 2437–2446, 2011.

[96] Shibukawa, Naoki, Iwasaki, Yoshifumi, and Watanabe, Mitsunori. Unsteady flow features and vibration stresses of an actual size steam turbine last stage in various low load conditions. In *Turbo Expo: Power for Land, Sea, and Air*, volume 55201, page V05BT25A030. American Society of Mechanical Engineers, 2013.

[97] Tanuma, Tadashi, Okuda, Hiroshi, Hashimoto, Gaku, Yamamoto, Satoru, Shibukawa, Naoki, Okuno, Kenichi, Saeki, Hiroshi, and Tsukuda, Tomohiko. Aerodynamic and structural numerical investigation of unsteady flow effects on last stage blades. In *Turbo Expo: Power for Land, Sea, and Air*, volume 56796, page V008T26A035. American Society of Mechanical Engineers, 2015.

[98] Tanuma, Tadashi, Ogawa, Michio, Okuda, Hiroshi, Hashimoto, Gaku, Shibukawa, Naoki, Okuno, Kenichi, and Tsukuda, Tomohiko. Unsteady flow effects on steam turbine last stage blades at very low load operating condition. In *Turbo Expo: Power for Land, Sea, and Air*, volume 51173, page V008T29A028. American Society of Mechanical Engineers, 2018.

[99] Zhou, Bin, Mujezinovic, Amir, Coleman, Andrew, Ning, Wei, and Ansari, Asif. Forced response prediction for steam turbine last stage blade subject to low engine order excitation. In *Turbo Expo: Power for Land, Sea, and Air*, volume 54679, pages 2447–2453, 2011.

[100] Moffatt, Stuart and He, Li. Blade forced response prediction for industrial gas turbines: Part 1—methodologies. In *Turbo Expo: Power for Land, Sea, and Air*, volume 36878, pages 407–414, 2003.

[101] Ning, Wei, Moffatt, Stuart, Li, Yansheng, and Wells, Roger G. Blade forced response prediction for industrial gas turbines: Part 2—verification and application. In *Turbo Expo: Power for Land, Sea, and Air*, volume 36878, pages 415–422, 2003.

[102] Qi, Di, Chen, Yifeng, Lin, Gang, Li, Wenfu, and Tan, Wei. Aerodynamic and structural numerical investigation of full annulus last stage of steam turbine under low load conditions. In *Turbo Expo: Power for Land, Sea, and Air*, volume 84201, page V009T23A027. American Society of Mechanical Engineers, 2020.

[103] Sigg, Roland and Rice, Timothy. The characteristics of rotating instabilities in low pressure steam turbines at low volume flow operation. In *Turbo Expo: Power for Land, Sea, and Air*, volume 56796, page V008T26A028. American Society of Mechanical Engineers, 2015.

[104] Megerle, Benjamin, McBean, Ivan, Stephen Rice, Timothy, and Ott, Peter. “Unsteady aerodynamics of low-pressure steam turbines

operating under low volume flow." *Journal of turbomachinery*, 136 (9):091008, 2014.

[105] Megerle, Benjamin, Rice, Timothy Stephen, McBean, Ivan, and Ott, Peter. Turbulent scale resolving modelling of rotating stall in low-pressure steam turbines operated under low volume flow conditions. In *Turbo Expo: Power for Land, Sea, and Air*, volume 56796, page V008T26A016. American Society of Mechanical Engineers, 2015.

[106] Ercan, Ilgit and Vogt, Damian M. Detached eddy simulation of rotating instabilities in a low-pressure model steam turbine operating under low volume flow conditions. In *Turbo Expo: Power for Land, Sea, and Air*, volume 85017, page V008T22A006. American Society of Mechanical Engineers, 2021.

[107] Liu, Bo, Yang, Jiandao, Zhou, Daiwei, Zhu, Xiaocheng, and Du, Zhaohui. Numerical investigations of flow features in a low pressure steam turbine last stage under different mass flow rates. In *Turbo Expo: Power for Land, Sea, and Air*, volume 56796, page V008T26A022. American Society of Mechanical Engineers, 2015.

[108] Rzadkowski, Romuald, Surwiło, Jan, Kubitz, Leszek, Lampart, Piotr, and Szymaniak, Mariusz. Unsteady forces in last stage lp steam turbine rotor blades with exhaust hood. In *Turbo Expo: Power for Land, Sea, and Air*, volume 49842, page V07BT34A020. American Society of Mechanical Engineers, 2016.

[109] Hoznedl, Michal, Sedlák, Kamil, Mrózek, Lukáš, Dadáková, Tereza, Kubín, Zdeněk, and Gregor, Karel. Experimental and numerical study of flow and dynamics on lsb at 34 mw steam turbine. In *Turbo Expo: Power for Land, Sea, and Air*, volume 84201, page V009T23A003. American Society of Mechanical Engineers, 2020.

[110] Cooley, James W and Tukey, John W. "An algorithm for the

machine calculation of complex fourier series." *Mathematics of computation*, 19(90):297–301, 1965.

[111] Mendez, M. A. "Lecture on data-driven modal analysis." *at VonKarman Insitute for FluidMechanics*.

[112] Lumley, John L. *Stochastic tools in turbulence*. Courier Corporation, 2007.

[113] Sirovich, Lawrence. "Turbulence and the dynamics of coherent structures. i. coherent structures." *Quarterly of applied mathematics*, 45(3):561–571, 1987.

[114] Sirovich, Lawrence. "Chaotic dynamics of coherent structures." *Physica D: Nonlinear Phenomena*, 37(1-3):126–145, 1989.

[115] Berkooz, Gal, Holmes, Philip, and Lumley, John L. "The proper orthogonal decomposition in the analysis of turbulent flows." *Annual review of fluid mechanics*, 25(1):539–575, 1993.

[116] Sarkar, S. "Identification of flow structures on a lp turbine blade due to periodic passing wakes." *Journal of fluids engineering*, 130 (6), 2008.

[117] Lengani, Davide and Simoni, Daniele. "Recognition of coherent structures in the boundary layer of a low-pressure-turbine blade for different free-stream turbulence intensity levels." *International Journal of Heat and Fluid Flow*, 54:1–13, 2015.

[118] Lengani, D, Simoni, D, Ubaldi, M, Zunino, P, and Guida, R. Turbulence production, dissipation and length scales in laminar separation bubbles. In *11th International ERCOFTAC Symposium on Engineering Turbulence Modelling and Measurements, Sicily, Italy, Sept*, pages 21–23, 2016.

[119] Lengani, D, Simoni, D, Ubaldi, M, Zunino, P, Bertini, F, and Michelassi, V. "Accurate estimation of profile losses and analysis

of loss generation mechanisms in a turbine cascade." *Journal of Turbomachinery*, 139(12):121007, 2017.

[120] Davide, Lengani, Simoni, Daniele, Ubaldi, Marina, Zunino, Pietro, and Bertini, Francesco. "Coherent structures formation during wake-boundary layer interaction on a lp turbine blade." *Flow, Turbulence and Combustion*, 98(1):57–81, 2017.

[121] Lengani, D, Simoni, D, Pichler, R, Sandberg, RD, Michelassi, V, and Bertini, F. "On the identification and decomposition of the unsteady losses in a turbine cascade." *Journal of Turbomachinery*, 141(3):031005, 2019.

[122] Mendez, MA, Balabane, M, and Buchlin, JM. "Multi-scale modal analysis of complex fluid flows." *arXiv preprint arXiv:1804.09646*, 2018.

[123] Fondelli, Tommaso, Diurno, Tommaso, Palanti, Lorenzo, Andreini, Antonio, Facchini, Bruno, Nettis, Leonardo, Arcangeli, Lorenzo, and Maceli, Nicola. Investigation on low-pressure steam turbine exhaust hood modelling through computational fluid dynamic simulations. In *AIP Conference Proceedings*, volume 2191, page 020076. AIP Publishing LLC, 2019.

[124] Menter, Florian R. "Two-equation eddy-viscosity turbulence models for engineering applications." *AIAA journal*, 32(8):1598–1605, 1994.

[125] Roache, Patrick J. *Verification and validation in computational science and engineering*, volume 895. Hermosa Albuquerque, NM, 1998.

[126] Celik, Ishmail B, Ghia, Urmila, Roache, Patrick J, and Freitas, Christopher J. "Procedure for estimation and reporting of uncertainty due to discretization in cfd applications." *Journal of fluids Engineering-Transactions of the ASME*, 130(7), 2008.

[127] Diurno, Tommaso, Fondelli, Tommaso, Nettis, Leonardo, Maceli, Nicola, Arcangeli, Lorenzo, Andreini, Antonio, and Facchini, Bruno. "Numerical investigation on the aerodynamic performance of a low-pressure steam turbine exhaust hood using design of experiment analysis." *Journal of Engineering for Gas Turbines and Power*, 142(11), 2020.

[128] Diurno, Tommaso, Tomasello, Stella Grazia, Fondelli, Tommaso, Andreini, Antonio, Facchini, Bruno, Nettis, Leonardo, and Arcangeli, Lorenzo. Development of a design approach for the optimization of steam turbine exhaust system performance through cfd modelling. In *Turbo Expo: Power for Land, Sea, and Air*, volume 85017, page V008T22A013. American Society of Mechanical Engineers, 2021.

[129] Fu, Jing-Lun, Liu, Jian-Jun, and Zhou, Si-Jing. "Unsteady Interactions Between Axial Turbine and Nonaxisymmetric Exhaust Hood Under Different Operational Conditions." *Journal of Turbomachinery*, 134(4), 07 2011. ISSN 0889-504X. 041002.

[130] Lengani, D, Simoni, D, Pichler, R, Sandberg, RD, Michelassi, V, and Bertini, F. "On the identification and decomposition of the unsteady losses in a turbine cascade." *Journal of Turbomachinery*, 141(3):031005, 2019.

[131] Alekseenko, SV, Kuibin, PA, Okulov, Valery Leonidovich, and Shtork, SI. "Helical vortices in swirl flow." *Journal of Fluid Mechanics*, 382:195–243, 1999.